Title

Inferring the Properties of Galaxies and Dark Matter Halos from the Dynamics of Their Stars and Star Clusters

Author

Wasserman, Asher Daniel

Publication Date

2020

UNIVERSITY OF CALIFORNIA
SANTA CRUZ

INFERRING THE PROPERTIES OF GALAXIES AND DARK MATTER HALOS FROM THE DYNAMICS OF THEIR STARS AND STAR CLUSTERS

A dissertation submitted in partial satisfaction of the
requirements for the degree of

Doctor of Philosophy

in

ASTRONOMY AND ASTROPHYSICS

by

Asher Wasserman

March 2020

The Dissertation of Asher Wasserman
is approved:

Jean P. Brodie, Chair

Alexie Leauthaud

Aaron J. Romanowsky

Duncan A. Forbes

Quentin Williams
Acting Vice Provost and Dean of Graduate Studies

Table of Contents

List of Figures

List of Tables

Abstract

Inferring the properties of galaxies and dark matter halos from the dynamics of their stars and star clusters

by

Asher Wasserman

There is a long and rewarding history in astronomy of studying the motions of stars, gas, and planets to learn about the distribution of mass in the universe. Observations of nearby galaxies rotating faster than otherwise expected are one of the pillars of evidence for the cold dark matter (CDM) cosmological model. As increasingly precise predictions are made about the small scale distribution of mass in the universe, we need tools to be able to weigh our beliefs about the mass content of galaxies and how they can be updated by increasingly richer and more complete observations. In this thesis I present a series of applications of a Bayesian hierarchical model for the equilibrium dynamics of spherical galaxies. Some key features of the model are: a natural mechanism for propagating the systematic uncertainty of parameters such as orbital anisotropy, distance, and stellar mass-to-light ratio into estimates for the dark matter content of galaxies, the ability to jointly model multiple tracer populations with heterogeneous data, and a clear way to incorporate and examine prior assumptions about galaxy and dark matter scaling relations.

Acknowledgments

This thesis contains previously published materials, originally published as Wasserman et al. (2018a,b, 2019). I thank my co-authors for their support and for allowing me to use these works in my thesis: Aaron Romanowsky, Jean Brodie, Duncan Forbes, Pieter van Dokkum, Alexa Villaume, Adebusola Alabi, Charlie Conroy, Jay Strader, Sabine Bellstedt, Roberto Abraham, Yotam Cohen, Shany Danieli, Christopher Martin, Matt Matuszewski, John Tamanas, Stefano Profumo.

My work was supported by NSF grants AST-1616598 and AST-1616710, the University of California Observatories, and the ARCS Foundation of Northern California.

Some of the data presented herein were obtained at the W.M. Keck Observatory, which is operated as a scientific partnership among the California Institute of Technology, the University of California and the National Aeronautics and Space Administration. The Observatory was made possible by the generous financial support of the W.M. Keck Foundation.

This research has made use of NASA's Astrophysics Data System and the NASA/IPAC Extragalactic Database (NED) which is operated by the Jet Propulsion Laboratory, California Institute of Technology, under contract with the National Aeronautics and Space Administration.

Funding for the DEEP2/DEIMOS pipelines (Cooper et al. 2012; Newman et al. 2013c) has been provided by NSF grant AST-0071048. The DEIMOS spectrograph (Faber et al. 2003) was funded by grants from CARA (Keck Observatory) and UCO/Lick

Observatory, a NSF Facilities and Infrastructure grant (ARI92-14621), the Center for Particle Astrophysics, and by gifts from Sun Microsystems and the Quantum Corporation.

This research made use of Astropy, a community-developed core Python package for Astronomy (Collaboration et al. 2018a). I acknowledge the use of other open source Python packages, including Numpy (van der Walt et al. 2011), Scipy (Virtanen et al. 2019), Matplotlib (Hunter 2007), Pandas (McKinney 2010), IPython (Perez & Granger 2007), Scikit-learn (Pedregosa et al. 2011). I acknowledge the use of the open source programming language Julia (Bezanson et al. 2017) as well as DifferentialEquations.jl (Rackauckas & Nie 2017).

I wish to recognize and acknowledge the very significant cultural role and reverence that the summit of Maunakea has always had within the indigenous Hawaiian community. We are most fortunate to have the opportunity to conduct observations from this mountain.

“Everyone must have two pockets, so that he can reach into the one or the other, according to his needs. In his right pocket are the words: ‘For my sake was the world created,’ and in his left: ‘I am earth and ashes.’ ”

– Simcha Bunim of Peshischa

Going through graduate school has brought me plenty of occasions to reach into both pockets. I would not have made it here were it not for support from family, friends, and the deeply caring community I have found here in Santa Cruz. Thank you for helping me find space to grow and thrive.

Chapter 1

Introduction

Using the motion of objects in space to infer the distribution of mass in the universe has a distinguished history. From foundational tests of general relativity to the discovery and characterization of planets outside of our own solar system, the principle that motion implies mass has led to great strides in our understanding of the universe. To first order, we can relate motion to mass with a simple dimensional analysis as

$$M \sim \frac{Rv^2}{G} \tag{1.1}$$

where M is the total (i.e., dynamical) mass, R is the length scale of the system, v is the velocity scale of the system (e.g., the velocity dispersion), and G is Newton's gravitational constant. Indeed, just flipping this relation around reveals that this is the virial theorem, which holds that the average kinetic energy of a system is proportional to the gravitational potential energy.

Observations of the dynamics of galaxies provided some of the earliest evidence for dark matter (DM), dating back to studies from the 1930s by Oort and Zwicky. More precise measurements of the rotation curves of spiral galaxies made in the 1970s (e.g., Rubin et al. 1978) helped demonstrate that this unseen matter, should it exist, must be spread throughout a large "halo" of mass that extends far beyond the spatial extent of stars and gas in galaxies. For further historical details, I refer readers to the reviews of Faber & Gallagher (1979), Trimble (1987), and de Swart et al. (2017).

One readily apparent challenge in measuring the DM content of galaxies is finding and measuring the kinematics of a suitable population of tracers of the galactic potential. For late-type spiral galaxies such as those studied by Rubin and collaborators, the rotations of gas could be observed out to tens of kiloparsecs, on the order of the sizes of the galaxies themselves. While these observations were sufficient to show flat rotational profiles consistent with large mass-to-light ratios, we often lack such convenient tracers in the form of gas or stellar disks for dispersion-supported systems like massive elliptical galaxies and dwarf spheroidal galaxies.

Globular clusters (GCs) are compact clusters of millions of stars. While the exact formation mechanisms of GCs are unknown, we do know that most of them formed very early in the history of the universe, and that many of the GCs we see today in the outer stellar halos of galaxies were accreted from smaller galaxies that merged to form the galaxies we see today (Beasley et al. 2002; Brodie & Strader 2006). This latter claim is bolstered by observations that the spatial distribution of GC systems is ~ 4 times more extended than the spatial extent of galaxies as measured by their integrated starlight (Forbes 2017). In light of this observation (and as illustrated in Figure 1.1), we see that GCs provide a particularly useful role in measuring the motions of galaxies in orbits far beyond those of the majority of their stars.

It should be noted that this population of kinematic tracers is separate from that of the field stars in the galaxy. In addition to the different spatial scale, GC systems often have different distributions of orbits from that of the field stars (e.g., Zhu et al. 2014). This difference can help us alleviate the well-known degeneracy between dynamical mass and orbital anisotropy, shown in Figure 1.2. We can get even more leverage over the dynamics of galaxies by exploiting our understanding of multiple subpopulations of GCs. Early studies of GC systems found evidence of bimodality in their color distributions (e.g., Zinn 1985; Zepf & Ashman 1993; Ostrov et al. 1993). These two color subpopulations are often referred to as metal-rich (red) and metal-poor (blue). When splitting GCs into these subpopulations, we find that they often follow different spatial and kinematic distributions (Pota et al. 2013; Zhu et al. 2016; Forbes 2017).

Modern studies of the DM content of galaxies has moved beyond the first-order calculation of the amount of DM around galaxies to questions about the small-scale spatial distribution of DM in the universe. In particular, what is the mass distribution of DM within galaxies, and how does DM content map to stellar content for lower mass dwarf galaxies? Much of the recent progress and current challenges surrounding these problems are documented by Weinberg et al. (2015); Bullock & Boylan-Kolchin (2017).

To learn something new from galaxy dynamics, we need to carefully integrate information from diverse sources and weigh the uncertainties from a variety of systematic effects. In addition, to answer questions about how surprising we find various observations,

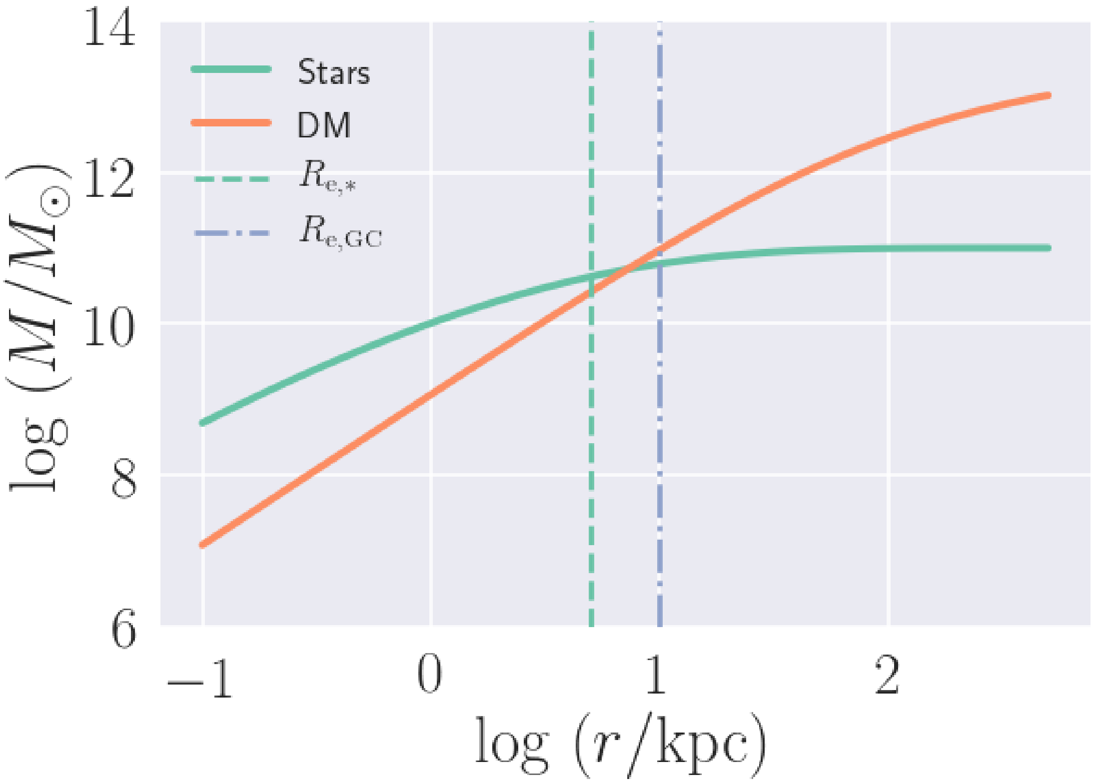

Figure 1.1: Enclosed mass profile for a model galaxy with a stellar mass of $\log_{10} M_*/M_\odot = 11$ and a DM halo mass of $\log_{10} M_{200\mathrm{c}}/M_\odot = 13$. The green dashed line shows the effective radius of the galaxy (as traced by integrated starlight) while the dot-dashed blue line shows the effective radius of the globular cluster population. We see that for a typical massive elliptical galaxy, the GC system probes a region of the galaxy that is dynamically dominated by dark matter.

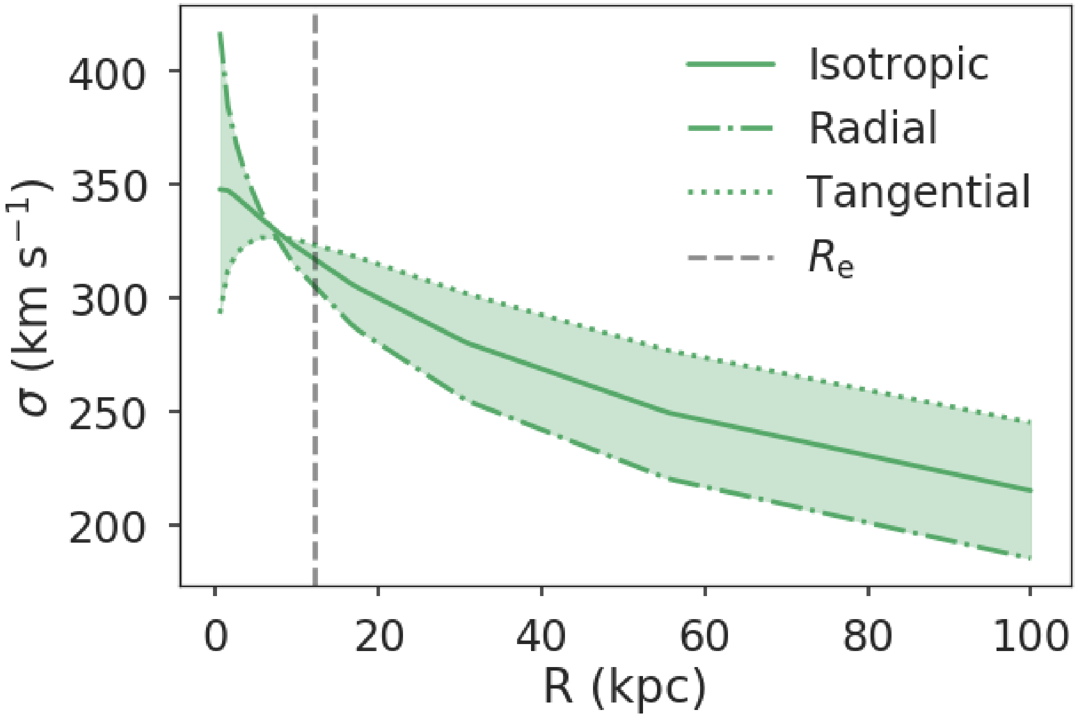

Figure 1.2: Velocity dispersion profile for a model galaxy under different assumptions for the orbital anisotropy of the tracer (but with a fixed mass profile). Uncertainty in the associated mass profile is minimized at the “pinch point” at approximately the effective radius of the galaxy, where the predictions from the different anisotropy models overlap.

we need a framework for evaluating the impact of our prior beliefs. The language of Bayesian statistical inference provides such tools. In this thesis, I show how combining simple dynamical models for spherical galaxies with techniques from Bayesian statistics can help us answer interesting questions about the relationships between galaxies, globular clusters systems, and dark matter halos.

In Chapter 2, I present a summary of the Bayesian dynamical modeling formalism. Chapters 3 through 5 are taken from Wasserman et al. (2018a,b, 2019). Each of these chapters represents an application or extension of the model from Chapter 2. Chapter 3, contains an application of the model to the dynamics of the massive elliptical galaxy NGC 1407. In Chapter 4, I investigate claims of missing DM around the ultra-diffuse galaxy NGC 1052-DF2. In Chapter 5, I use the model to evaluate evidence for fuzzy dark matter around the Coma Cluster ultra-diffuse galaxy Dragonfly 44. Finally in Chapter 6, I summarize this work and speculate on promising areas of future work.

Chapter 2

Bayesian Spherical Jeans Modeling

2.1 The spherical Jeans equation

Consider a spherical galaxy. More precisely, consider a population of collisionless point tracers[1] in dynamical equilibrium in a spherical galaxy. Our task is this: given the volume density $\rho(r)$ of this population of point tracers orbiting in a gravitational potential $\Phi(r)$, specified by the cumulative mass distribution $M(r)$, we would like to derive the statistical distribution of the velocities of these tracers and relate them to observable quantities such as the line-of-sight (LOS) velocity dispersion and kurtosis.

We use the notational convention that r refers to a three dimensional spherical radius (i.e., the de-projected radius) and R refers to a two dimensional cylindrical radius along the LOS (i.e., the projected radius).

Following Binney & Tremaine (2008), under the above assumptions we can

---

[1] In context, these tracers can be observable stars or star clusters in a galaxy for which we can reasonably assume that the relaxation time is sufficiently large.

derive the spherical Jeans equation from taking the second moment of the phase space distribution function as

$$\frac{\mathrm{d}(\rho(r)\sigma_r^2(r))}{\mathrm{d}r} + \frac{2\beta(r)}{r}\rho\sigma_r^2(r) = -\rho\frac{\mathrm{d}\Phi(r)}{\mathrm{d}r} = -\rho\frac{GM(r)}{r^2} \tag{2.1}$$

where σ_r is the radial velocity dispersion profile, M is the cumulative mass profile, and β is the anisotropy parameter profile, defined as

$$\begin{aligned} \beta &= 1 - \frac{\sigma_\theta^2 + \sigma_\phi^2}{2\sigma_r^2} \\ &= 1 - \frac{\sigma_\theta^2}{\sigma_r^2} \end{aligned} \tag{2.2}$$

where in the second line we have made use of the fact that, for our spherically symmetric galaxy, $\sigma_\theta = \sigma_\phi$. When $\beta = 0$, we say the system is isotropic, and Equation 2.1 can be greatly simplified. When $\beta \in (0, 1)$, we say the orbits of tracers in the system are radially-biased, since $\sigma_r^2 > \sigma_\theta^2$. When $\beta < 0$, we say the orbits of the tracers are tangentially-biased.

We can multiply both sides of Equation 2.1 by the integrating factor[2]

$$g_\beta(r) = \exp\left(\int_1^r \frac{2\beta(\tilde{r})}{\tilde{r}}\,\mathrm{d}\tilde{r}\right) \tag{2.3}$$

and then integrate both sides with respect to r to directly relate the radial velocity dispersion profile to the mass distribution:

$$\sigma_r^2(r) = \frac{1}{\rho(r)g_\beta(r)}\int_r^\infty \rho(\tilde{r})g_\beta(\tilde{r})\frac{GM(\tilde{r})}{\tilde{r}^2}\,\mathrm{d}\tilde{r} \tag{2.4}$$

---

[2] Since g appears once in both the numerator and denominator of Equation 2.4, the choice of lower integration bound in Equation 2.3 is arbitrary as the constant of integration becomes a common factor when exponentiated.

In general, with the exception of a handful of very nearby galaxies, we lack full six-dimensional phase space measurements of the tracers. Thus, we must first project σ_r^2 along the LOS and second, we must make some assumptions about β and how it changes with galactocentric radius.

2.1.1 Projecting the radial velocity dispersion

To derive the LOS velocity dispersion, we compute the tracer density-weighted component of the velocity dispersion tensor $\boldsymbol{\sigma}^2(\boldsymbol{x}) = \sigma_r^2\hat{r} + \sigma_\theta^2\hat{\theta} + \sigma_\phi^2\hat{\phi}$ projected along the LOS given by the unit vector $\hat{s}$. We then take the Abel transform of this quantity, given by $\rho(r)\ \hat{s}\cdot\boldsymbol{\sigma}^2\cdot\hat{s}$. For the spherically symmetric velocity dispersion tensor, with $\hat{s}$ arbitrarily aligned with the z axis (used as the reference axis for the polar angle, θ), we have

$$\begin{aligned}\hat{s}\cdot\boldsymbol{\sigma}^2\cdot\hat{s} &= \sigma_r^2(\hat{s}\cdot\hat{r})^2 + \sigma_\theta^2(\hat{s}\cdot\hat{\theta})^2 \\ &= \sigma_r^2\cos^2 i + \sigma_\theta^2\sin^2 i \\ &= \sigma_r^2\left(\frac{\sqrt{r^2-R^2}}{r}\right)^2 + \sigma_\theta^2\left(\frac{R}{r}\right)^2 \qquad (2.5)\end{aligned}$$

where i is the inclination angle between $\hat{s}$ and the vector $\hat{\boldsymbol{x}} = (\sin\theta\cos\phi, \sin\theta\sin\phi, \cos\theta)$, and $R = \sqrt{r^2 - s^2}$ is the projected radius. Note by construction, $\hat{s}\cdot\hat{\phi} = 0$. Thus applying the relation $\sigma_\theta^2 = (1-\beta)\sigma_r^2$, we have

$$\begin{aligned}\sigma^2_{\rm LOS}(R) &= \frac{2}{\Sigma(R)}\int_R^\infty \frac{r}{\sqrt{r^2-R^2}}\rho(r)\left(\sigma_r^2\frac{r^2-R^2}{r^2}+\sigma_\theta^2\frac{R^2}{r^2}\right)\,{\rm d}r\\ &= \frac{2}{\Sigma(R)}\int_R^\infty \frac{r}{\sqrt{r^2-R^2}}\rho(r)\sigma_r^2\left(1-\frac{R^2}{r^2}+(1-\beta)\frac{R^2}{r^2}\right)\,{\rm d}r\\ &= \frac{2}{\Sigma(R)}\int_R^\infty \left(1-\beta\frac{R^2}{r^2}\right)\rho(r)\sigma_r^2(r)\frac{r}{\sqrt{r^2-R^2}}\,{\rm d}r \qquad (2.6)\end{aligned}$$

where $\Sigma(R)$ is the projected surface density of the tracer population[3]. Replacing σ_r^2 in Equation 2.6 with the right-hand side of Equation 2.4, we obtain the following double integral expression

$$\sigma^2_{\rm LOS}(R) = \frac{2G}{\Sigma(R)}\int_R^\infty \frac{r}{\sqrt{r^2-R^2}}\left(1-\beta\frac{R^2}{r^2}\right)\frac{1}{g_\beta(r)}\int_r^\infty \rho(\tilde r)g_\beta(\tilde r)\frac{M(\tilde r)}{\tilde r^2}\,{\rm d}\tilde r\,{\rm d}r\ . \qquad (2.7)$$

2.1.2 The Jeans kernel

For some limiting assumptions about $\beta(r)$, we can simplify the above double integral into a more computationally efficient single integral. Mamon & Łokas (2005) derive a range of such formulae (listed in their appendix) of the form

$$\sigma^2_{\rm LOS}(R) = \frac{2G}{\Sigma(R)}\int_R^\infty K_\beta\left(r,R\right)\frac{\rho(r)M(r)}{r}\,{\rm d}r \qquad (2.8)$$

where

$$K_\beta(r,R) = \int_R^r \frac{1}{g_\beta(\tilde r)}\frac{\tilde r}{\sqrt{\tilde r^2-R^2}}\left(1-2\beta(\tilde r)\frac{R^2}{\tilde r^2}\right)\,{\rm d}\tilde r \qquad (2.9)$$

is the Jeans kernel. This kernel can be thought of as accounting for the projection effects of β on both the radial velocity dispersion and the LOS integral. For $\beta(r) = \beta$ (i.e.,

---

[3] Astute readers will note that the integrand in Equation 2.6 is undefined for $r = R$ at the lower integration bound. In practice, so long as the numerical integration is performed down to some value of $R+\epsilon$, the integral converges without problem.

anisotropy is invariant with galactocentric radius, Mamon & Łokas (2005) find

$$K_\beta(u) = \frac{u^{2\beta-1}}{2}\left[\left(\frac{3}{2}-\beta\right)\sqrt{\pi}\frac{\Gamma(\beta-1/2)}{\Gamma(\beta)} + \beta B\left(\frac{1}{u^2},\beta+\frac{1}{2},\frac{1}{2}\right) - \beta B\left(\frac{1}{u^2},\beta-\frac{1}{2},\frac{1}{2}\right)\right] \tag{2.10}$$

where $u = r/R$,

$$\Gamma(z) = \int_0^\infty x^{z-1}e^{-x}\,\mathrm{d}x \tag{2.11}$$

is the Gamma function, and

$$B(z;a,b) = \int_0^z x^{a-1}(1-x)^{b-1}\,\mathrm{d}x \tag{2.12}$$

is the incomplete Beta function. We note that the incomplete Beta function as used in Equation 2.10 will diverge for $\beta \leq 1/2$. Thus, we introduce the analytic continuation of the incomplete Beta function in terms of the hypergeometric function (e.g., Straton 2002)

$$B(z;a,b) = \frac{z^a}{a}\ {}_2F_1(z;a,1-b,a+1)\ . \tag{2.13}$$

where

$${}_2F_1(z;a,b,c) = \sum_{n=0}^{\infty}\frac{(a)_n(b)_n}{(c)_n}\frac{z^n}{n!} \tag{2.14}$$

is the hypergeometric function and

$$(q)_n = \begin{cases} 1 & n=0 \\ \prod_{i=0}^{n-1}(q+i) & n>0 \end{cases} \tag{2.15}$$

is the rising Pochhammer term. Computationally efficient evaluations of the hypergeometric function are readily available (e.g., Galassi et al. 2009), but care must still be taken to avoid divergences at half-integral values of β. Fortunately Mamon & Łokas (2005) provide limiting cases of $K_\beta(u)$ for the relevant cases.

2.1.3 A flexible anisotropy model

For many realistic models of $\beta(r)$, an analytic expression for K_β does not exist, and thus we must resort to computing the full double integral of Equation 2.7 numerically. Read & Steger (2017) proposed a flexible anisotropy model of the form

$$\beta(r) = \beta_0 + (\beta_\infty - \beta_0)\left(1 + \left(\frac{r_\beta}{r}\right)^{n_\beta}\right)^{-1} \tag{2.16}$$

where β_0 is the inner anisotropy value, β_∞ is the outer anisotropy value, r_β is the transition radius, and n_β controls the sharpness of the transition. For certain values of the parameter, this model is identical to that of Osipkov (1979) and Merritt (1985), as well as that preferred by Mamon & Łokas (2005). For those particular cases, Mamon & Łokas (2005) provide analytic expressions for K_β, but in general for arbitrary parameters we are left to numerically integrate both the inner and outer integral expressions for σ^2_{LOS}. There is – at least – a concise analytic expression for $g_\beta(r)$ with this model

$$g_\beta(r) = r^{2\beta_\infty}\left(\left(\frac{r_\beta}{r}\right)^{n_\beta} + 1\right)^{\frac{2}{n_\beta}(\beta_\infty - \beta_0)} \tag{2.17}$$

2.1.4 Line-of-sight kurtosis

By construction, odd velocity moments of the phase space distribution function in a spherically symmetric model do not exist (e.g., the mean velocity field is zero). However in addition to computing the second velocity moment of the distribution function (in the form of the velocity dispersion) and its associated LOS projection, we can also compute higher-order even velocity moments (i.e., the kurtosis).

The LOS velocity kurtosis is defined as

$$\kappa_{\rm LOS}(R) = \frac{\overline{v^4_{\rm LOS}(R)}}{\sigma^4_{\rm LOS}(R)} \tag{2.18}$$

where $\overline{v^4_{\rm LOS}}$ refers to the fourth-moment of the LOS velocity distribution. In the general case of a radially varying β this is infeasible to compute, but for the case of constant β, Łokas (2002) derived the following relations in analogy to those for the second-order velocity moments:

$$\rho(r)\overline{v^4_r}(r) = 3r^{-2\beta}\int_r^\infty \tilde{r}^{2\beta}\rho(\tilde{r})\sigma^2_r(\tilde{r})\frac{GM(\tilde{r})}{\tilde{r}}{\rm d}\tilde{r} \tag{2.19}$$

$$\begin{aligned}\overline{v^4_{\rm LOS}}(R) = \frac{2}{\Sigma(R)}\int_R^\infty \Bigg[\left(1-\frac{R^2}{r^2}\right)^2 + 2(1-\beta)\frac{R^2(r^2-R^2)}{r^4} \\ +\frac{(2-\beta)(1-\beta)}{2}\frac{R^4}{r^4}\Bigg]\frac{\rho(r)\overline{v^4_r}r}{\sqrt{r^2-R^2}}{\rm d}r\end{aligned} \tag{2.20}$$

2.2 Mass models

In many applications, the enclosed mass profile we wish to model is composed of different components, e.g., a stellar mass profile and a halo mass profile. Sometimes the tracer density profile, $\rho(r)$, will be identical to the dynamical mass density profile (i.e., a self-consistent model)

$$\rho_M(r) = \frac{1}{4\pi r^2}\frac{{\rm d}M}{{\rm d}r} \ . \tag{2.21}$$

However for many cases this is overly restrictive, and we will model the tracer density separate from the total mass density.

2.2.1 Sérsic model

The density distribution of stars (and star clusters systems) in galaxies are often described with a Sérsic model. The surface density profile in this model is given by

$$\Sigma(R) = \Sigma_0 \exp\left(-b_n \left(\frac{R}{R_\mathrm{e}}\right)^{1/n}\right) \tag{2.22}$$

where Σ_0 is the central surface density, R_e is the effective radius, n is the Sérsicindex, and b_n is a function of n chosen such that R_e matches the definition that $2L(< R_\mathrm{e}) = L_\mathrm{tot}$. Efficient and accurate approximations for b_n are given by Ciotti & Bertin (1999), but for a quick reference we can use $b_n \approx 2n - 1/3$.

The de-projected volume density profile of this model a complicated analytic form, but we can make use of the following approximation

$$\rho(r) = \Sigma_0 \frac{b_n^{n(1-p_n)}}{2R_e} \frac{\Gamma(2n)}{\Gamma((3-p_n)n)} \left(\frac{r}{R_e}\right)^{-p_n} \exp\left(-b_n \left(\frac{r}{R_e}\right)^{1/n}\right) \tag{2.23}$$

where Γ is the gamma function and the function p_n is chosen to match the Abel inversion of Equation 2.22, and whose approximation is found by Lima Neto et al. (1999). The enclosed mass (within de-projected radius r) is given by

$$M(r) = 2\pi n \Sigma_0 \left(\frac{R_\mathrm{e}}{b_n^n}\right)^2 \frac{\Gamma(2n)}{\Gamma((3-p_n)n)} \gamma\left[(3-p_n)n, b_n \left(\frac{r}{R_\mathrm{e}}\right)^{1/n}\right] \tag{2.24}$$

where γ is the lower incomplete gamma function. For an overview of the Sérsic density model, see the review of Graham & Driver (2005).

2.2.2 Halo models

In the absence of baryonic effects or beyond-CDM physics, the profiles of Navarro et al. and Einasto (the NFW and Einasto models, respectively) have been shown to be adequate descriptions of the structure of DM halos down to the smallest scales resolved by simulations.

When taking into account baryonic effects such as adiabatic contraction (Blumenthal et al. 1986) or bursty star formation (Pontzen & Governato 2012), the distribution of mass in the halo can change. A more flexible DM density profile is given by the double power law $\alpha\beta\gamma$ model:

$$\rho(r) = \rho_s \left(\frac{r}{r_s}\right)^{-\gamma} \left(1 + \left(\frac{r}{r_s}\right)^{\alpha}\right)^{(\gamma-\beta)/\alpha} \tag{2.25}$$

where ρ_s is the scale density, r_s is the scale radius, γ is the negative inner log slope, β is the negative outer log slope, and α controls the sharpness of the transition between the two slopes (Hernquist 1990; Di Cintio et al. 2014). The enclosed mass profile for this halo model is given by

$$M(r) = \frac{4\pi\rho_s r_s^3}{\omega} \left(\frac{r}{r_s}\right)^{\omega} {}_2F_1\left[\frac{\omega}{\alpha}, \frac{\beta-\gamma}{\alpha}, 1 + \frac{\omega}{\alpha}; -x^{\alpha}\right] \tag{2.26}$$

where $\omega = 3 - \gamma$ and ${}_2F_1$ is the hypergeometric function.

For $(\alpha, \beta, \gamma) = (1, 3, 1)$, this reduces to the NFW profile. For $(\alpha, \beta) = (1, 3)$ with γ left as a free parameter, this model is sometimes known as the generalized NFW (or gNFW) model. Di Cintio et al. (2014) fit relations for the three shape parameters as a function of the stellar-to-halo mass ratio.

The Einasto model is similar in structure to the Sérsic model, and a good overview is given by Retana-Montenegro et al. (2012). For modeling the halos of dwarf galaxies in particular, Read et al. (2016) proposed the coreNFW model, which introduces a DM core to the NFW model on the spatial scale of the galaxy.

2.3 Bayesian inference

The space of possible models to choose from when describing a dynamical system is infinitely large, but even once we have specified a particular model we are left with numerous free parameters. We would like to learn from data what are reasonable beliefs for these parameters. Denoting the model parameters as θ and the data as D, Bayes' Theorem relates the conditional probability of model given the data to the conditional probability of the data given the model.

$$P(\theta|D) = \frac{P(D|\theta)P(\theta)}{P(D)} \tag{2.27}$$

The left hand side of this expression is the posterior probability of θ, the inverse of the conditional posterior probability (first term in the numerator on the right hand side) is the likelihood of the data given the model, and $P(\theta)$ is the prior probability of the model parameters. The denominator on the right hand side is the marginal likelihood, and is equal to

$$P(D) = \int P(D|\theta)P(\theta)\mathrm{d}\theta \ . \tag{2.28}$$

For many purposes, we only need to know the posterior density up to some multiplicative constant of θ. Thus, we can safely ignore the normalization of the marginal likelihood.

2.3.1 Likelihood

For velocity dispersion as measured through integrated starlight, we have data of the form $D = (R_i, \sigma_i, \delta\sigma_i)$ where $\delta\sigma_i$ is the measurement error for the i-th measurement. If we assume a Gaussian measurement error model, then the likelihood for continuous tracers is given by

$$\mathcal{L}(\sigma_i|\delta\sigma_i, R_i, \theta) = \mathcal{N}\left(\sigma_i|\sigma_J(R_i, \theta), \delta\sigma_i\right) \tag{2.29}$$

where the Normal PDF is

$$\mathcal{N}\left(x|\mu, \sigma\right) = \frac{1}{\sqrt{2\pi}\sigma} \exp\left(-\left(\frac{x-\mu}{\sqrt{2}\sigma}\right)^2\right) \tag{2.30}$$

and the Jeans model prediction, $\sigma_J(R_i, \theta)$ is given by Equation 2.7. For discrete tracers (e.g., radial velocity measurements of star clusters), we have data of the form $D = (R_i, v_i, \delta v_i)$. The Gaussian measurement error model is slightly different in this case.

$$\mathcal{L}(v_i|\delta v_i, R_i, \theta) = \mathcal{N}(v_i|v_{\text{sys}}, \sqrt{\sigma_J^2(R_i, \theta) + \delta v_i^2}) \tag{2.31}$$

where v_{sys} is the systemic velocity of the galaxy.

In general, we often assume that a set of measurements are conditionally independent, which is to say that if we fix θ, then knowing the value of D_i doesn't tell us anything more about the value of D_j. In this case,

$$\mathcal{L}(D|\theta) = \prod_i \mathcal{L}(D_i|\theta) \ . \tag{2.32}$$

However, we should be careful to verify that this is a reasonable assumption. Breaking this assumption can lead to underestimated uncertainties in the resulting estimates.

We often have multiple tracer populations we wish to simultaneously model. As in the case of multiple data points from a single tracer, we often make the assumption that the set of measurements are conditionally independent, and so their likelihoods can be multiplied to form the joint likelihood. However it is important to maintain the consistency of the dynamical mass model used between different tracer populations.

When combining different datasets, it can be useful to treat the scaling of the measurement uncertainties as a free parameter (Hobson et al. 2002; Ma & Berndsen 2014). In addition to accounting for the possibilities of over or underestimated uncertainties, this naturally allows for a more equal weighting of datasets with different number of measurements.

2.3.2 Priors

One benefit of Bayesian inference is that it allows for a clear description of any prior beliefs held by the researcher. Sometimes we wish to leave allow a parameter in the model to vary, but we have a well-informed belief for what its value should be and wish to propagate the uncertainty in the value forward to any other inferences. In that case, we can place an informative prior over this parameter, such as a Normal distribution with a mean of our expected value of the parameter and a standard deviation quantifying our pre-existing uncertainty over the parameter.

In other cases, we may wish to place a much more uninformative prior over the parameter, as we expect the data to be able to constrain this quantity. In such cases, care must be taken to examine the effects of any chosen prior on the resulting posterior distribution. Often researchers will place a uniform prior over a parameter and claim that it is an "uninformative" prior assumption. Such claims can be misleading however, as a uniform prior in one parameterization is a non-uniform prior in some other reasonable transformation of the parameter.

To be concrete, suppose we wished to set the total dynamical mass of the system as a free parameter. It is common practice to transform any quantity that is restricted to be non-negative (e.g., mass, distance, etc.) to a log scale in order to guarantee that this requirement is met. However, a uniform distribution in $\log(M)$ is equivalent to a M^{-1} prior in the linearized space. While a true non-informative distribution is sometimes feasible (i.e., the Jeffreys prior), such a calculation is often impractical and may in fact result in an improper (i.e., unnormalizable) distribution.

2.3.3 Sampling

From Equation 2.27, we know both the likelihood, $P(D|\theta)$ and the prior, $P(\theta)$. To draw samples from the posterior distribution, $P(\theta|D)$, we only need to know this distribution up to a multiplicative constant, and thus it is sufficient to write down the posterior probability distribution as $P(\theta|D) \propto P(D|\theta)P(\theta)$. Once we have this expression, we can use a Markov Chain Monte Carlo (MCMC) algorithm to sample from $P(\theta|D)$. The original Metropolis-Hastings sampler algorithm (Metropolis & Ulam 1949; Hastings 1970) is simple to write down, but requires fine-tuning of the proposal step size. Goodman & Weare (2010) proposed an ensemble sampling method that requires no fine-tuning of the proposal and has the nice property that the proposal is invariant with respect to affine transformations of the parameter space. A well-known implementation of this algorithm is provided by the `emcee` Python package (Foreman-Mackey et al. 2013).

Care must be taken when analyzing the resulting MCMC samples to ensure that the chain is converged and the samples are representative of the actual posterior probability distribution of interest. The most basic strategy for establishing convergence is to look at a plot of the samples as a function of iteration in the chain. For well mixed samples, this should be a stationary distribution, and any subset of the chain should give the same estimates of the posterior mean.

For standard (i.e., non-ensemble) MCMC methods, the Gelman-Rubin statistic can be used with multiple independent chains to validate the convergence of the method (Gelman & Rubin 1992). For ensemble based methods like that of Goodman & Weare (2010), the multiple chains are, by construction, non-independent. We can, however, still compute the auto-correlation length for the chain and verify that we have run the sampler for a sufficient factor of the auto-correlation length (Sokal 1997).

In practice, we will run the sampler for a fixed number of iterations, then visual inspect the chain to see when (if at all) the Markov chain has reached a stable equilibrium. Early iterations prior to this point are discard from the chain, as they may bias any estimates made with the sample.

2.3.4 Model comparison

It is common practice to write down multiple models to describe the data, often with different numbers of parameters, different priors, and/or different forms of the likelihood. In the frequentist modeling framework, it is common to describe the goodness-of-fit of a maximum likelihood estimator with a reduced χ^2 statistic,

$$\chi^2_\nu = \frac{1}{\nu} \sum_i \left(\frac{y_{\mathrm{obs},i} - y_{\mathrm{exp},i}}{\sigma_i} \right)^2 \tag{2.33}$$

where $\nu = n - p$ is the degrees of freedom (equal to the number of datapoints minus the number of free parameters), $y_{\rm obs}$ are the observed data, $y_{\rm exp}$ are the model expectations for each data point, and σ_i^2 is the variance for the data (e.g., measurement error). The resulting χ^2_ν statistic should be ~ 1 for a well-fit model, with $\chi^2_\nu < 1$ suggesting that the model over-fits the data and $\chi^2 > 1$ suggesting that the model under-fits the data.

While this is appropriate for a Gaussian likelihood with non-informative priors, in realistic applications of Bayesian inference, we need a more flexible model comparison tool that takes into account the spread in the posterior probability distribution. There is an alphabet soup of information criterion methods for model comparison in the literature: AIC, BIC, DIC, WAIC, etc. The underlying principle of most of these methods is to try to estimate the out-of-sample predictive accuracy of the model, and for a good theoretical overview of model comparison I direct readers to Gelman et al. (2013). To construct this exact quantity, we would need to know the true data generating model, but if we did know this then there would clearly be no point in comparing models. For the purpose of practical model comparison, Vehtari et al. (2015) proposed a method for approximate leave-one-out cross validation (LOO-CV). As long as we keep track of the point-wise likelihood during sampling, computing a LOO-CV information criterion is relatively computationally cheap, and serves as a robust measure of the predictive accuracy of different models, regardless of differing parameterizations, priors, or likelihood forms.

Chapter 3

Multi-population Jeans modeling of NGC 1407

3.1 Introduction

The concordance cosmological model of dark energy plus cold dark matter (ΛCDM) has had numerous successes in describing the large scale structure of the universe. The story on the scale of galaxy formation has been more complicated, with discrepancies in the number of satellite galaxies expected around the Milky Way (Klypin et al. 1999; Moore et al. 1999), the masses of the Milky Way satellites that are observed (Boylan-Kolchin et al. 2011; Bullock & Boylan-Kolchin 2017), and the inner slope of the dark matter density profile of galaxies (Flores & Primack 1994). It is this last point that we focus on here.

Navarro, Frenk, & White (1997) introduced a double power law model (hereafter the NFW model) of the halo density profile with $\rho \propto r^{-1}$ in the inner regions and $\rho \propto r^{-3}$ in the outer regions, which they found to describe well the form of halos from N-body simulations. This model can be generalized to include a variable inner slope, γ, and is often parameterized as

$$\rho(r) = \rho_s \left(\frac{r}{r_s}\right)^{-\gamma} \left(1 + \frac{r}{r_s}\right)^{\gamma-3} \quad , \tag{3.1}$$

where r_s is the scale radius which determines where the change in density slope occurs.

For $\gamma = 1$, this corresponds to the original NFW profile[1]. While this "universal" profile provided a good match to their DM-only simulations, deviations from this profile have been observed in various mass regimes. For instance, dwarf galaxies have often been found to have shallower inner density slopes (Simon et al. 2003; Spekkens et al. 2005; Walker & Peñarrubia 2011; Oh et al. 2011, though see Adams et al. 2014; Pineda et al. 2017). On the opposite end of the mass spectrum, Newman et al. (2013a) used both gravitational lensing and stellar dynamics to measure $\langle\gamma\rangle \sim 0.5$ for a sample of massive galaxy clusters.

If DM halos start with an NFW-like steep inner profile, then some physical mechanism for transferring energy to DM in the inner regions is necessary to create the shallower DM profiles observed for some galaxies. Self-interacting or fuzzy DM scenarios have been proposed to solve this issue (e.g, Rocha et al. 2013; Robles et al. 2015; Di Cintio et al. 2017b). However, baryonic effects may also explain DM cores,

---

[1] In this work, we use the convention $\gamma = -\mathrm{d}\log\rho/\mathrm{d}\log r$, such that a larger value of γ implies a steeper slope.

either from bursty star formation at the low mass end (Navarro et al. 1996; Mashchenko et al. 2008; Pontzen & Governato 2012) or from dynamical friction during gas-poor mergers at the high mass end (El-Zant et al. 2004). In addition, Dekel et al. (2003) argued that merging satellites whose halos have DM cores would be disrupted outside of the central halo's core, leading to a stable DM core in the central galaxy. Whatever processes are responsible for flattening the DM density profile must compete with the effects of adiabatic contraction (Blumenthal et al. 1986), whereby the infalling of gas during the process of galaxy formation causes a steepening of the halo density profile.

To disentangle these many effects on the halo, we need to observationally map out how the inner DM slope changes as a function of halo mass across a wide range of mass regimes. While there are already many good constraints on this relation for dwarf galaxies and for clusters of galaxies, there remains a dearth of observational measurements of the inner DM slope for halos between the masses of 10^{12} and 10^{13} $M_\odot$, which typically host massive early-type galaxies (ETGs). These massive galaxies are particularly critical tests for the presence of new, non-CDM physics, as many of the baryonic effects on the halo are small compared to those for dwarf galaxies.

Mass inferences with dispersion-dominated dynamics suffer from a number of challenges. For one, the total mass is degenerate with the distribution of the orbits of the kinematic tracers being modeled. A general strategy for dealing with this mass–anisotropy degeneracy is to simultaneously model multiple kinematic tracers with separate distributions of their orbits.

Walker & Peñarrubia (2011) applied this approach to the Fornax and Sculptor dwarf spheroidal (dSph) galaxies by splitting their resolved stellar kinematic data into chemo-dynamically distinct components, then making separate mass estimates using each subpopulation. Previous studies of massive ETGs modeled multiple tracer populations such as globular clusters (GCs), planetary nebulae (PNe), and integrated-light stellar kinematics to alleviate the mass–anisotropy degeneracy (Schuberth et al. 2010; Agnello et al. 2014; Pota et al. 2015; Zhu et al. 2016; Oldham & Auger 2016).

These studies were able to provide good constraints on the total mass of DM halos, but inferring the detailed density distribution of halos requires a precise determination of the stellar mass distribution. In contrast to the dSph galaxies studied by Walker & Peñarrubia (2011), the inner regions of ETGs are dynamically dominated by baryonic matter. As Pota et al. (2015) found, the degeneracy between the inferred stellar mass-to-light ratio (Υ_*) and the inner DM density slope undermines attempts to draw robust conclusions about the slope of the DM halo. Furthermore, in all of the studies cited above, Υ_* was assumed to be constant across all galactocentric radii (but see Li et al. 2017; Poci et al. 2017; Mitzkus et al. 2017; Oldham & Auger 2018a for work that relaxes this assumption). Given that many ETGs are found to have spatially varying stellar populations, the constant Υ_* assumption is an important systematic uncertainty in understanding the inner DM density distribution (Martín-Navarro et al. 2015; McConnell et al. 2016; van Dokkum et al. 2017a).

Using data from the SAGES Legacy Unifying Globulars and GalaxieS (SLUGGS) survey[2] (Brodie et al. 2014), we model the dynamics of the massive elliptical galaxy

---

[2] `http://sluggs.ucolick.org`

NGC 1407. SLUGGS is a survey of 25 nearby ETGs across a variety of masses, environments, and morphologies. NGC 1407 has been studied by numerous authors (e.g., Romanowsky et al. 2009; Su et al. 2014; Pota et al. 2015), but here we revisit the galaxy with state-of-the-art stellar population synthesis results, a new method for modeling the stellar mass distribution, and a more rigorous statistical treatment of the influence of multiple disparate datasets. This paper is a pilot work for an expanded study of a larger subset of SLUGGS galaxies.

In Section 3.2, we summarize the observational data. In Section 3.3, we describe the dynamical modeling and our method for combining distinct observational constraints. In Section 3.4 we present the results of applying our model to NGC 1407. In Section 3.5 we interpret these results in the context of other observations and theoretical predictions. We summarize our findings in Section 3.6, and we present our full posterior probability distributions in Appendix A (Section 3.7.1). We show the result of various systematic uncertainty tests in Appendix B (Section 3.7.2).

3.2 Data

NGC 1407 is a bright ($M_K = -25.46$; Jarrett et al. 2000), X-ray luminous ($L_X = 8.6 \times 10^{40}$ erg s^{-1} within 2 R_e; Su & Irwin 2013), massive elliptical galaxy at the center of its eponymous galaxy group. Brough et al. (2006) argued on the basis of its high X-ray luminosity and low spiral fraction that the NGC 1407 group is dynamically mature. The central galaxy is a slow rotator ($\lambda_{R_\mathrm{e}} = 0.09$; Bellstedt et al. 2017). We adopt a systemic velocity of 1779 km s^{-1} (Quintana et al. 1994). The galaxy shows slight ellipticity (de Vaucouleurs et al. 1991 reported a flattening of $\epsilon = 0.07$), and so we calculate the projected galactocentric radius as

$$R^2 = q\Delta x^2 + q^{-1}\Delta y^2 \ , \tag{3.2}$$

where Δx and Δy are coordinate offsets along the major and minor axes respectively and q is the axial ratio (b/a). Here we have adopted a position angle of 58.4°(Spolaor et al. 2008).

There are numerous conflicting redshift-independent distances for NGC 1407 in the literature. Cantiello et al. (2005) used surface brightness fluctuation (SBF) measurements to obtain a value of 25.1 ± 1.2 Mpc, while Forbes et al. (2006) used the globular cluster luminosity function to obtain a value of 21.2 ± 0.9 Mpc. Using a weighted average of both SBFs and fits to the Fundamental Plane, Tully et al. (2013) derived a distance of 28.2 ± 3.4 Mpc. Using the Planck Collaboration et al. (2016) cosmological parameters and correcting the recession velocity to the Virgo infall frame, the galaxy has a luminosity distance of 24.2 ± 1.7 Mpc. When including the distance to the galaxy as a free parameter, we use a Gaussian prior with a mean of 26 Mpc and a standard deviation of 2 Mpc. We find an a posteriori distance of $21.0^{+1.5}_{-1.4}$ Mpc (see Sec. 3.4) corresponding to a distance scale of 0.102 kpc per arcsecond. It is this distance that we adopt for any distance-dependent results that are not already marginalized over this parameter. We report the effects of adopting a wide uniform prior on the distance in Appendix 3.7.2.1.

Here we summarize the kinematic, photometric, and stellar population data that we use for our models.

3.2.1 Stellar density

We use the same surface brightness profile as Pota et al. (2013), who combined Subaru/Suprime-Cam g band and *HST*/ACS F435 imaging into a single B band profile out to $440''$. Masking out the core at $R < 2''$, they fitted a single Sérsic component (Eqn. 3.3).

$$I(R) = I_0 \exp\left(-b_n \left(\frac{R}{R_e}\right)^{1/n}\right) \tag{3.3}$$

Here, I_0 is the central surface density, R_e is the effective radius, n is the Sérsic index, and b_n is a function of n chosen such that $2L(R_e) = L_\mathrm{tot}$ (see Eqn. 18 in Ciotti & Bertin 1999, for an asymptotic expansion of b_n). Pota et al. (2013) found an effective radius of $R_\mathrm{e} = 100'' \pm 3''$, a Sérsic index of $n = 4.67 \pm 0.15$, and a central surface brightness of $I_0 = 1.55 \times 10^{11}\ \mathrm{L}_{\odot,B}\ \mathrm{kpc}^{-2}$ (adopting a solar absolute magnitude of $M_{\odot,B} = 5.48$).

To derive a stellar mass surface density profile, we use the spatially-resolved Υ_* measurements of van Dokkum et al. (2017a), shown in Fig. 3.1. Details of the Low Resolution Imaging Spectrograph (LRIS) observations, data reduction, and modeling can be found in Sections 2 and 3 of van Dokkum et al. (2017a). Fitting of the extracted 1D spectra was performed with the stellar population synthesis (SPS) models of Conroy et al. (2018) (an update to those of Conroy & van Dokkum 2012), using the extended stellar library of Villaume et al. (2017) and the MIST stellar isochrones (Choi et al. 2016). The logarithmic slope of the initial mass function (IMF) was allowed to vary in the ranges of $0.08 < M/M_\odot < 0.5$ and $0.5 < M/M_\odot < 1$. For $M/M_\odot > 1$, a Salpeter

(1955) log slope of -2.35 was adopted.

Since these Υ_* values were computed for I band, we use the $B-I$ color profile measured by Spolaor et al. (2008) to convert to a B band Υ_*. We then multiply these Υ_* measurements by the stellar surface brightness profile to obtain the mass surface density profile shown in Fig. 3.2, propagating uncertainties under the assumption that the Υ_* uncertainties dominate over the photometric uncertainties. We compare this variable Υ_* density profile with one determined from multiplying the surface brightness profile by a constant $\Upsilon_* = 8.61$ (chosen to match the two enclosed stellar mass values at $100''$). We see that the variable Υ_* profile is noticeably more compact than the constant Υ_* profile. We discuss this more in Sec. 3.5.3.

The Sérsic fits to the stellar luminosity and mass surface density profiles are listed in Table 3.1.

3.2.2 GC density

Nearly all massive ETGs have been found to have GC systems with a bimodal color distribution (Brodie & Strader 2006), and NGC 1407 is no exception (Forbes et al. 2006). The red and blue modes are expected to trace metal-rich and metal-poor GCs respectively, with the basic galaxy formation scenario associating metal-rich GCs with in-situ star formation and metal-poor GCs with accretion (Brodie & Strader 2006; Peng et al. 2006; Harris et al. 2017).

Since we model the dynamics of the blue and red GC subpopulations simultaneously, we use separate surface number density profiles for each subpopulation, using the

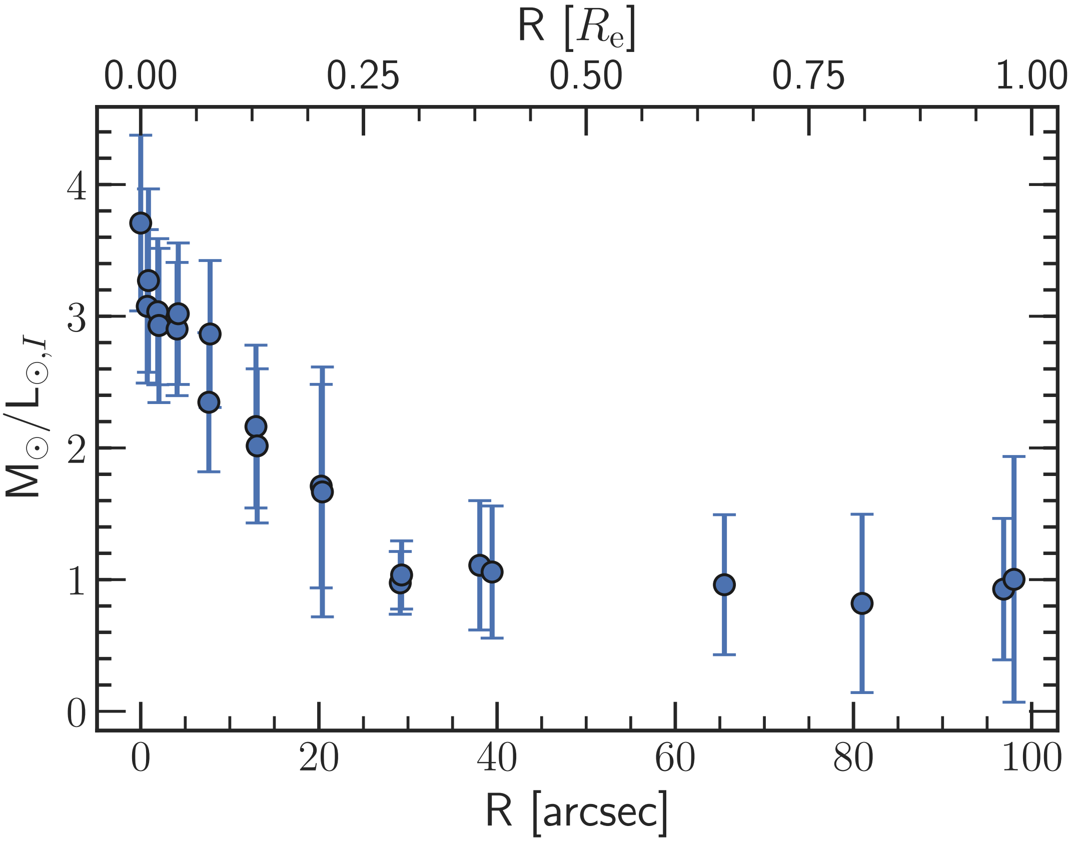

Figure 3.1: Stellar mass-to-light profile of NGC 1407 from van Dokkum et al. (2017a).

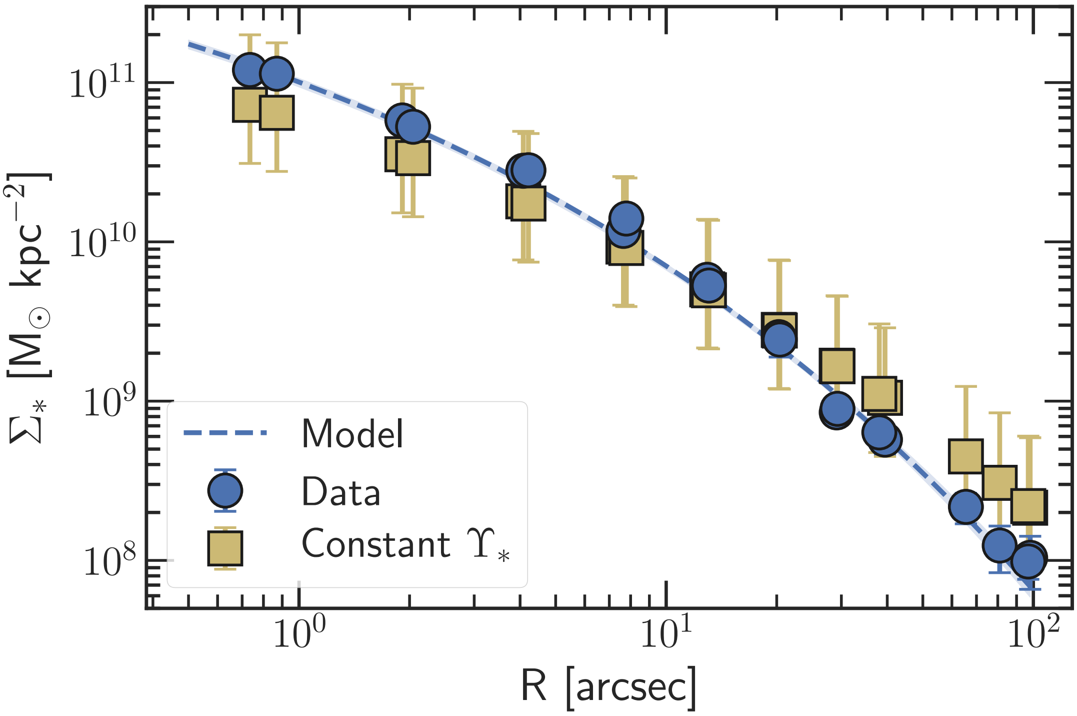

Figure 3.2: Stellar mass surface density. Blue circles show the measured values using the variable Υ_* profile. The blue dashed line shows the best fit model (see Sec. 3.3) of the surface density, with the width of the curve showing the inner 68% of samples. We compare this with a profile derived from a constant Υ_*, shown as the yellow squares. The uncertainties on these points are taken from the typical uncertainties on Υ_*.

	I_0	R_e	n
Stellar luminosity	1.55×10^{11}	100 ± 3	4.67 ± 0.15
Stellar mass	3.25×10^{12}	23 ± 2	3.93 ± 0.05
Red GCs	354	169 ± 7	1.6 ± 0.2
Blue GCs	124	346 ± 30	1.6 ± 0.2

Table 3.1: Sérsic profile parameters. Left to right: central surface density, effective radius (in arcseconds), and Sérsic index. The central surface density has units of $\mathrm{L}_{\odot,B}$ kpc^{-2} for the stellar luminosity, $\mathrm{M}_\odot$ kpc^{-2} for the stellar mass, and count arcmin^{-2} for the GCs.

results from Pota et al. (2013). With Subaru/Suprime-Cam g and i band imaging, they fitted a single Sérsic profile plus uniform background contamination model to both the red and blue subpopulations, splitting the two subpopulations at a color of $g - i = 0.98$ mag. Their resulting Sérsic parameters are listed in Table 3.1, and the profiles are shown in Fig. 3.3.

Relative to the field star density distribution, the GC profiles show flatter inner cores, possibly due to tidal destruction of GCs at small galactocentric radii. The red GC subpopulation is more compact than the blue GCs, though both are far more spatially extended than the field stars.

In Fig. 3.4 we show the log-slopes of the tracer surface density profiles as a function of radius. The density slope of the red GC subpopulation qualitatively matches that of the field stars in the outer halo, matching expectations that the metal-rich GCs are associated with the field star population (Forbes et al. 2012).

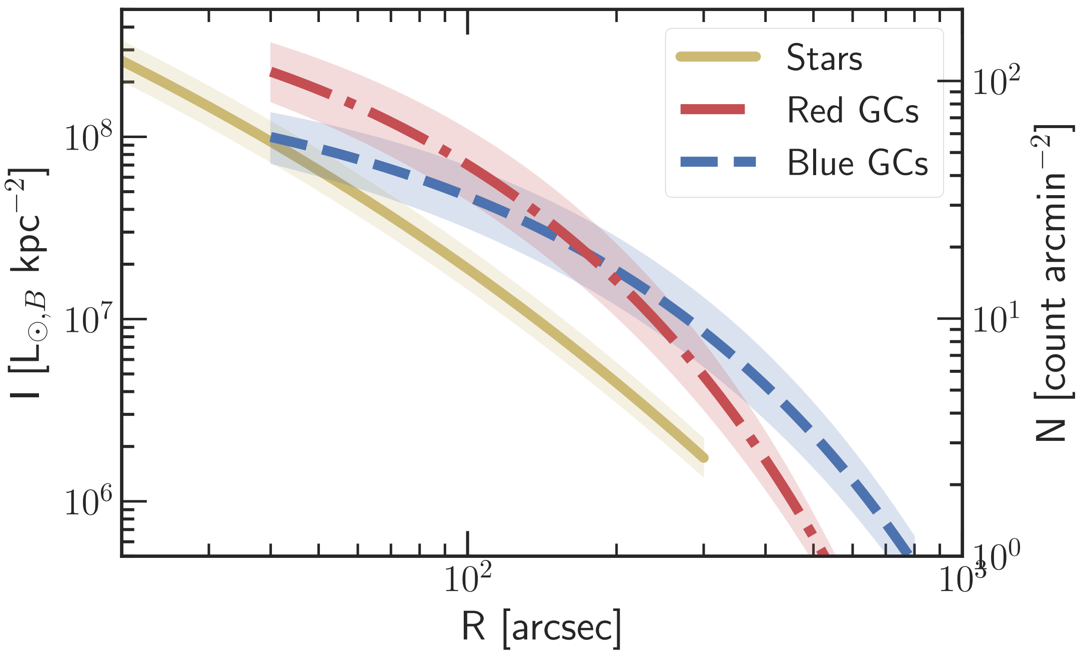

Figure 3.3: Surface brightness and surface number density profiles for the field stars, blue GCs, and red GCs. The extent of the radial ranges represent where the profiles were fitted to the photometric data, and the width of the curve shows the propagated uncertainty in the Sérsic parameters.

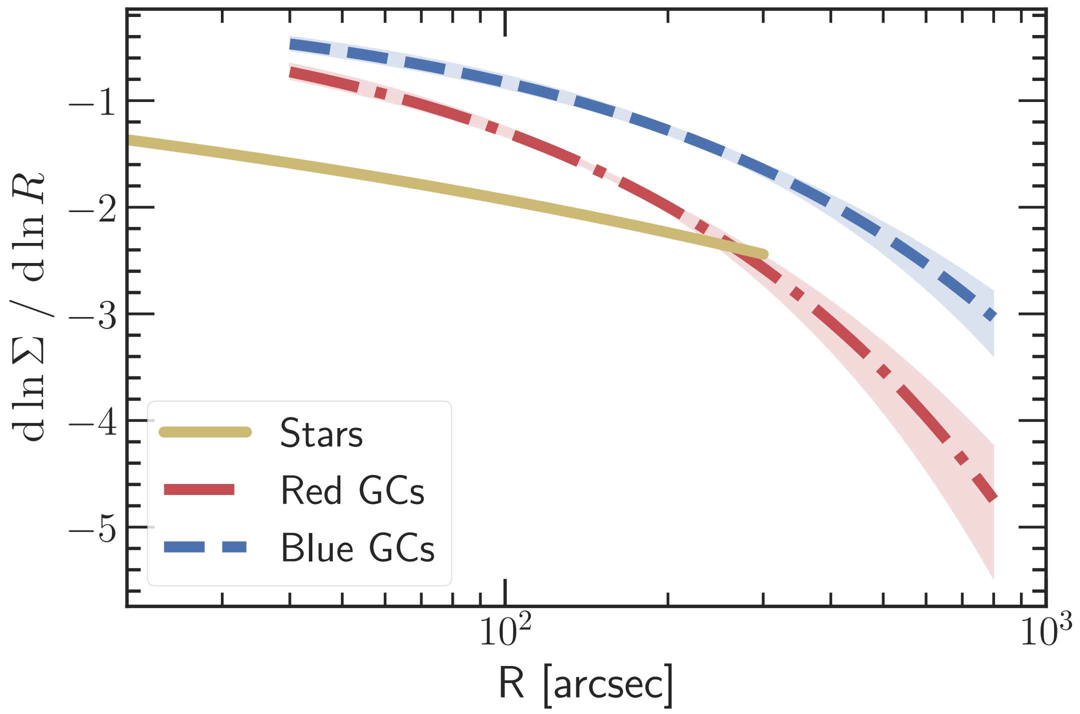

Figure 3.4: Log-slopes of the surface brightness and surface number density profiles for the field stars, blue GCs, and red GCs. The extent of the radial ranges represent where the profiles were fitted to the photometric data, and the width of the curve shows the propagated uncertainty in the Sérsic parameters.

3.2.3 Stellar kinematics

In the inner $\sim 40''$ ($0.4\ R_\mathrm{e}$) of the galaxy, we use longslit spectroscopy along the major axis from the ESO Faint Object Spectrograph and Camera (EFOSC2), originally analyzed by Spolaor et al. (2008). These data were re-analyzed by Proctor et al. (2009), who used penalized pixel fitting (Cappellari & Emsellem 2004) to calculate a velocity dispersion profile for the galaxy.

Here we define the velocity dispersion as the root mean square (RMS) velocity, $v_\mathrm{rms} = \sqrt{\langle v^2 \rangle}$. For the longslit data along the major axis, we account for the slight rotational motion by calculating v_rms as

$$v_\mathrm{rms} = \sqrt{\frac{v_\mathrm{rot}^2}{2} + \sigma^2} \tag{3.4}$$

where σ is the standard deviation of the line-of-sight velocity distribution (LOSVD) (Napolitano et al. 2009). With $\langle v/\sigma \rangle \sim 0.09$, there is a difference of less than 3 km s^{-1} between the σ and v_rms profiles.

To reach out to much farther galactocentric radii, we use the Keck/DEIMOS multislit observations presented by Arnold et al. (2014) and Foster et al. (2016), which sample the stellar light in 2D. Using only spectra visually classified as “good” by Foster et al. (2016), these stellar velocity dispersion measurements reach out to $\sim 200''$ ($2R_\mathrm{e}$), though of course with sparser spatial sampling than the longslit kinematic data. We calculate the velocity dispersion for these 2D measurements as

$$v_\mathrm{rms} = \sqrt{v_\mathrm{rot}^2 + \sigma^2}\ . \tag{3.5}$$

These stellar kinematic measurements are shown in Fig 3.5.

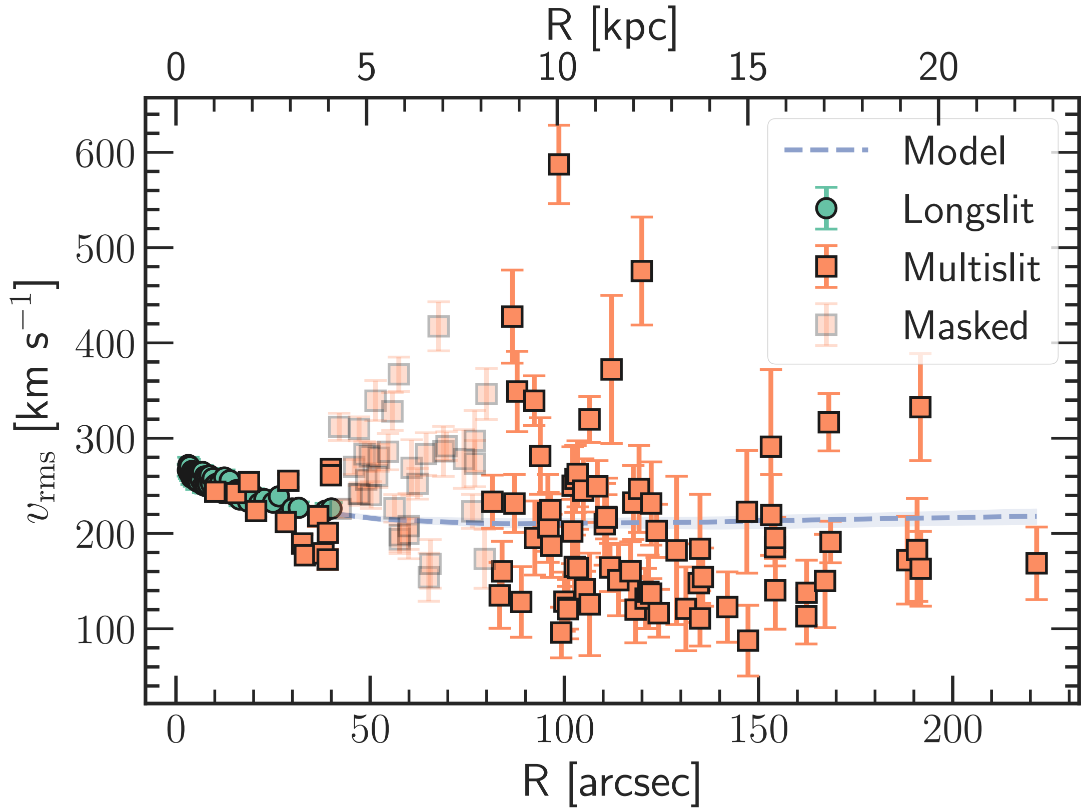

Figure 3.5: Stellar velocity dispersion data out to 2 $R_{\rm e}$ ($\sim$ 20 kpc). The lighter points between 40″ and 80″ show where we mask data due to substructure. The green circles show the longslit data, the orange squares show the multislit data, and the blue line shows the best fit stellar velocity dispersion model described in Sec. 3.3, with the width of the curve showing the inner 68% of samples. We note that the error bars have *not* been visually scaled following the best-fit weighting parameter (Sec. 3.3.2).

There are two complications in pre-processing the stellar kinematic data. The first is the potential presence of substructure in the kinematics in the region between $40''$ and $80''$. This deviation from a monotonically decreasing velocity dispersion profile was also seen in the velocity dispersion profile measured by van Dokkum et al. (2017a), and it is further mirrored in the metallicity bump seen by Pastorello et al. (2014). Following Pota et al. (2015), we mask out this region for our analysis (the lighter points in Fig. 3.5). We discuss the effects of removing these data in Appendix 3.7.2.2. The second complication is the influence of the central super-massive black hole (SMBH). Rusli et al. (2013) inferred the presence of a $\sim 4 \times 10^9$ $\mathrm{M}_\odot$ SMBH in NGC 1407 with a corresponding sphere of influence with radius $\sim 2''$. To avoid having to model the dynamical effects of the SMBH, we restrict our analysis to radii outside of $3''$.

3.2.4 GC kinematics and colors

We use the GC kinematics presented in Pota et al. (2015). The spectra for these measurements were obtained from ten Keck/DEIMOS slitmasks. The red and blue GC radial velocities (RVs) in Fig. 3.6 reveal that the two subpopulations have systematically different velocity dispersions in the outer regions. The GC radial velocity measurements for NGC 1407, as well as for the entire SLUGGS sample, can be found in Forbes et al. (2017).

The $g - i$ color distribution of our spectroscopic GC dataset, shown in Fig. 3.7, is well-matched to the photometric GC catalog presented in Pota et al. (2013). We fit a Gaussian Mixture Model to the spectroscopic sample color distribution and compare the

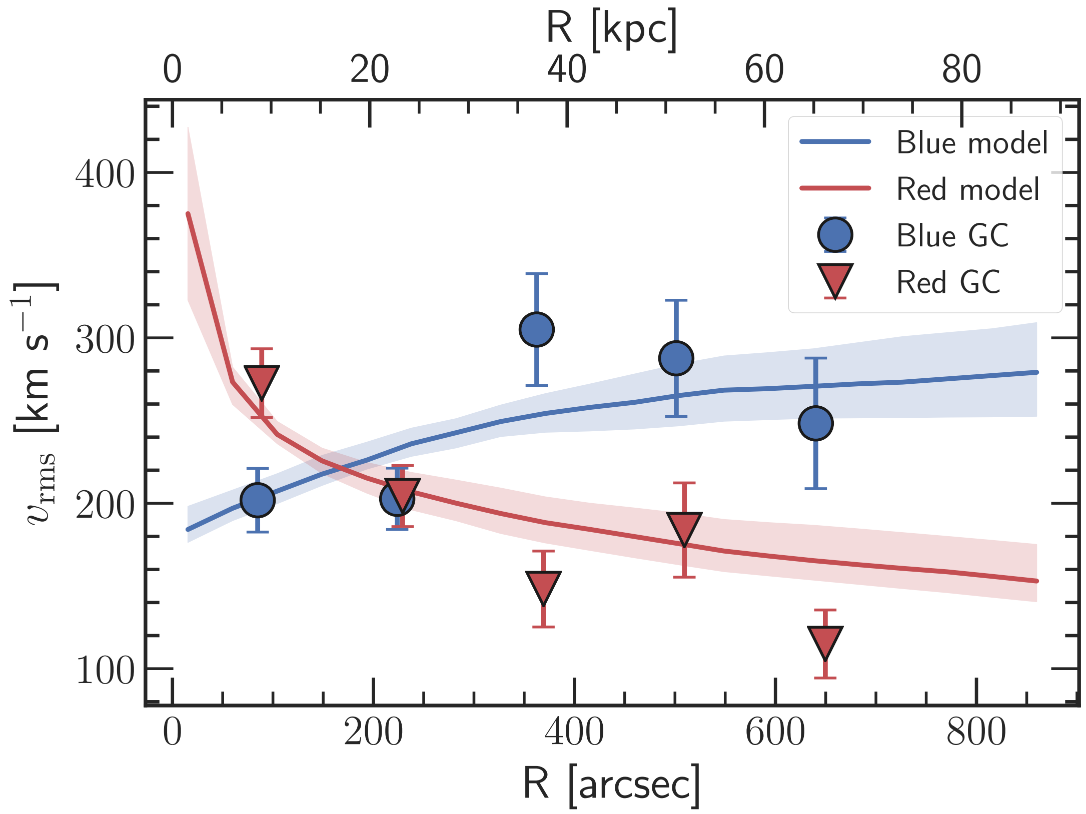

Figure 3.6: GC velocity dispersion vs. galactocentric radius, with blue GCs and red GCs showing systematically different trends in their scatter at large galactocentric radii. The blue GC subpopulation has a rising velocity dispersion profile, while the red GC subpopulation has a falling velocity dispersion profile. The associated best fit models of the GC velocity dispersion profiles are described in Sec. 3.3, with the width of the curves showing the inner 68% of samples.

	μ_c	σ_c	ϕ
Blue GCs (photometric sample)	0.85	0.05	—
Red GCs (photometric sample)	1.10	0.1	—
Blue GCs (RV sample)	0.87	0.067	0.52
Red GCs (RV sample)	1.12	0.094	0.48

Table 3.2: GC color Gaussian parameters. Comparison of the color distribution of our spectroscopic GC sample with that of the GC system overall. The weights, ϕ, indicate the fraction of GCs which come from the specified subpopulation.

result with the distributions found for the photometric sample of Pota et al. (2013)[3], listed in Table 3.2. We find that the color Gaussians of the RV GC sample have nearly identical means to those of the photometric sample, though the blue Gaussian of the RV sample has a slightly larger standard deviation than that of the photometric sample.

We emphasize that we do *not* split the GCs into red and blue subpopulations based on color for the dynamical analysis, but rather use this information to assign a probability of being in either subpopulation for each GC (Sec. 3.3.2).

3.3 Methods

Here we describe the dynamical (Sec. 3.3.1) and statistical (Sec. 3.3.2) methods that we use to model our data.

---

[3] We note that the mean color of the red GCs was swapped with that of NGC 2768 in the presentation of their Table 3.

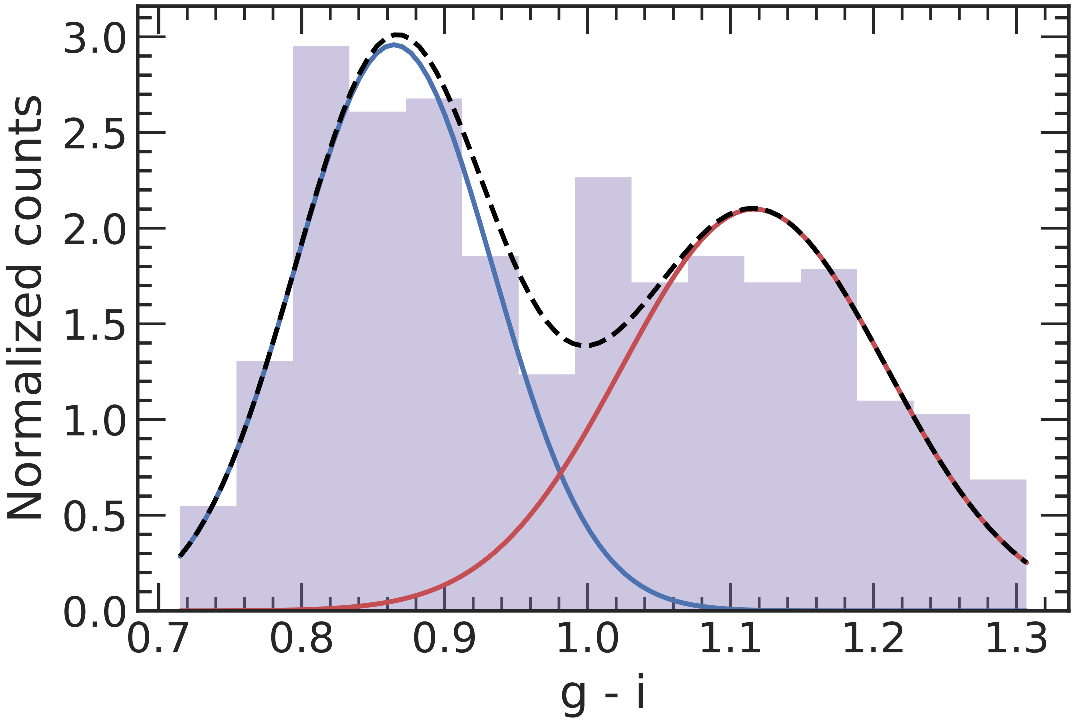

Figure 3.7: Gaussian mixture model of GC colors from our RV GC dataset. The blue and red curves show the Gaussian color distribution for the blue GC and red GC subpopulations respectively, while the dashed black curve shows that the sum of these distributions accurately captures the observed RV GC color distribution (in the violet histogram).

3.3.1 Dynamical model

Given the low v/σ and near-circular isophotes of the galaxy, we assume spherical symmetry for our model. Further assuming that we have a perfectly collisionless tracer population in steady-state, we can write the spherically symmetric Jeans equation as

$$\frac{\mathrm{d}(\nu \bar{v_r^2})}{\mathrm{d}r} + 2\frac{\beta}{r}\nu \bar{v_r^2} = -\nu \frac{\mathrm{d}\Phi}{\mathrm{d}r} \tag{3.6}$$

where ν is the volume density of the tracer, and

$$\beta \equiv 1 - \frac{\sigma_\theta^2 + \sigma_\phi^2}{2\sigma_r^2} \tag{3.7}$$

is the standard orbital anisotropy parameter (Binney & Tremaine 2008).

We can integrate once to obtain the mean square of the radial component of the velocity, and again to obtain the projected line-of-sight (LOS) RMS velocity. Following Mamon & Łokas (2005) the latter is,

$$v_{\mathrm{rms,los}}^2(R) = \frac{2G}{I(R)} \int_R^\infty K\left(\frac{r}{R},\ \beta\right) \nu(r) M(<r) \frac{dr}{r} \tag{3.8}$$

where $I(R)$ is the surface density profile, $\nu(r)$ is the volume density profile, $M(< r)$ is the enclosed mass profile, and $K(u, \beta)$ is the appropriate Jeans kernel. The Jeans kernel weighs the impact of the orbital anisotropy across the various deprojected radii, r, associated with the projected radius, R.

We note that we only model the LOS v_{rms}, and not any higher-order moments of the LOS velocity distribution. If we assume that the anisotropy parameter of a tracer is constant at all radii, then we have

$$\begin{aligned}K(u,\beta) = \frac{1}{2}u^{2\beta-1}\Bigg[\left(\frac{3}{2}-\beta\right)\sqrt{\pi}\frac{\Gamma(\beta-1/2)}{\Gamma(\beta)} \\ +\beta B\left(\beta+\frac{1}{2},\frac{1}{2};\frac{1}{u^2}\right) \\ -B\left(\beta-\frac{1}{2},\frac{1}{2};\frac{1}{u^2}\right)\Bigg]\end{aligned} \tag{3.9}$$

where $B(a,b;z)$ is the incomplete Beta function (Mamon & Łokas 2005, Appendix A). By writing the incomplete Beta function in terms of the hypergeometric function,

$$B(a,b;z) = a^{-1}z^a \; {}_2F_1[a, 1-b, a+1; z] \tag{3.10}$$

we can extend this formula to values of $\beta \leq 1/2$ that would otherwise make this expression undefined.

We model our tracer density as a Sérsic profile (Eqn. 3.3). For the blue and red GCs, the parameters of these Sérsic profiles are fixed to the values described in Sec. 3.2.2. For the stellar density profile, we freely vary the Sérsic parameters to jointly constrain the stellar surface density profile shown in Sec. 3.2.1 and the impact of the stellar mass on the kinematics.

The deprojected volume density profile in the Sérsic model is approximated as

$$\nu(r) = I_0 \frac{b_n^{n(1-p_n)}}{2R_e}\frac{\Gamma(2n)}{\Gamma((3-p_n)n)}\left(\frac{r}{R_e}\right)^{-p_n}\exp\left(-b_n\left(\frac{r}{R_e}\right)^{1/n}\right) \tag{3.11}$$

where the reciprocal polynomial p_n can be found by minimizing the difference with this equation and the density as computed from an inverse Abel transform of the projected surface density (see Eqn. 19 in Lima Neto et al. 1999 for an appropriate series approximation to p_n).

We use a generalized Navarro-Frenk-White (gNFW) dark matter density profile of the form given by Eqn. 3.1. The enclosed mass profile of this model is found by integrating the spherically-symmetric density profile,

$$\begin{aligned} M_{\mathrm{DM}}(<r) &= \int_0^r 4\pi r'^2 \rho(r')\,\mathrm{d}r' \\ &= 4\pi\rho_s \int_0^r r'^2 \left(\frac{r'}{r_s}\right)^{-\gamma} \left(1+\frac{r'}{r_s}\right)^{\gamma-3} \mathrm{d}r' \end{aligned} \tag{3.12}$$

Comparing this with the integral form of the hypergeometric function

$$ {}_2F_1[a,b,c;z] = \frac{1}{B(b,c-b)} \int_0^1 x^{b-1}(1-x)^{c-b-1}(1-zx)^{-a}\,\mathrm{d}x \tag{3.13}$$

where $B(x,y)$ is the complete Beta function, we obtain

$$M_{\mathrm{DM}}(<r) = \frac{4\pi\rho_s r_s^3}{\omega}\left(\frac{r}{r_s}\right)^{\omega} {}_2F_1\left[\omega,\omega,\omega+1;-\frac{r}{r_s}\right] \tag{3.14}$$

where $\omega \equiv 3-\gamma$.

The stellar mass is the deprojected enclosed luminosity of the Sérsic density profile, given by

$$M_*(<r) = 2\pi n\Sigma_0 \left(\frac{R_{\mathrm{e}}}{b_n^n}\right)^2 \frac{\Gamma(2n)}{\Gamma((3-p_n)n)}\,\gamma\left[(3-p_n)n, b_n\left(\frac{r}{R_{\mathrm{e}}}\right)^{1/n}\right] \tag{3.15}$$

where $\Gamma(z)$ is the complete Gamma function and $\gamma(z,x)$ is the lower incomplete Gamma function (Lima Neto et al. 1999). We note that here Σ_0 refers to the central surface mass density, not the surface brightness.

The total enclosed mass is thus given by

$$M(<r) = M_{\mathrm{DM}}(<r) + M_*(<r) + M_{\mathrm{BH}} \tag{3.16}$$

where we have included the central supermassive black hole (M_{BH}) as a single point mass at $r=0$.

3.3.2 Measurement model

We construct a Bayesian hierarchical model from the previously described dynamical model that is simultaneously constrained by the longslit stellar kinematics, the multislit stellar kinematics, the GC kinematics and colors, and the stellar mass surface density measurements. Since these data cover a range of different observations and modeling assumptions, we use the hyperparameter method of Hobson et al. (2002) to allow the properties of each dataset to determine their own relative weights.

For each dataset, we assign a parameter, α, that scales the uncertainties on the dataset as $\delta x \rightarrow \delta x/\sqrt{\alpha}$. This α parameter can be interpreted as the "trust" in the dataset, given the other data available and the model context in which the data are being evaluated. This is similar to the approach adopted by Oldham & Auger (2016) for balancing the contribution of stellar kinematics and GC kinematics to the overall likelihood, though we assign a weight parameter to each dataset under consideration. We do not model the co-variance between uncertainties in the datasets (see Ma & Berndsen 2014 for an extension of this method to covariant uncertainties).

We note that the introduction of these weight parameters means that we need to take care in specifying the likelihood. For a typical Gaussian likelihood, we can drop the constant $1/\delta x$ uncertainty factor (where δx refers to the measurement uncertainty), as it does not influence our sampling of the posterior distribution. However, the log likelihood for data, x, drawn from a Gaussian of mean, μ, and standard deviation,

$\delta x/\sqrt{\alpha}$, would now be

$$\ln \mathcal{L}(x, \delta x) = -\frac{1}{2}\left(\ln\left(\frac{2\pi\delta x^2}{\alpha}\right) + \alpha\left(\frac{x-\mu}{\delta x}\right)^2\right) \tag{3.17}$$

Thus there is now a free parameter in the first term which we cannot neglect. The following description of our joint likelihood assumes that all uncertainties on the data have already been weighted as specified here.

For the sake of visual clarity, in this section we write all velocity dispersion quantities as σ, despite the measured velocity dispersions being given by the RMS velocity and not the standard deviation of the LOSVD.

We model the stellar velocity dispersion data, $\sigma_i \pm \delta\sigma_i$, as being drawn from a Gaussian distribution about the Jeans model prediction, $\sigma_J(R_i)$.

$$\mathcal{L}_*(\sigma_i, \delta\sigma_i | \sigma_J(R_i)) = \frac{1}{\sqrt{2\pi\delta\sigma_i^2}} \exp\left(-\frac{(\sigma_J(R_i) - \sigma_i)^2}{\delta\sigma_i^2}\right) \tag{3.18}$$

We treat both the longslit and the multislit data as measuring the same kinematic tracer (and hence σ_J for both is calculated with the same density profile and anisotropy), but we use different weight parameters as discussed above. When separated, we use $\mathcal{L}_{\rm ls}$ and $\mathcal{L}_{\rm ms}$ to refer to the longslit and multislit likelihoods respectively.

We model the stellar mass surface density data, $\Sigma_i \pm \delta\Sigma_i$, as being drawn from a Gaussian distribution about the proposed Sérsic profile, $\Sigma_m(R_i)$.

$$\mathcal{L}_m(\Sigma_i, \delta\Sigma_i | \Sigma_m(R_i)) = \frac{1}{\sqrt{2\pi\delta\Sigma_i^2}} \exp\left(-\frac{(\Sigma_m(R_i) - \Sigma_i)^2}{\delta\Sigma_i^2}\right) \tag{3.19}$$

This is the same Sérsic profile used for the mass modeling, and so while the parameters of this model are primarily constrained by the data presented in Sec. 3.2.1, these Sérsic parameters also influence the predicted kinematic data.

Our analysis of the GC kinematic data differs from that of Pota et al. (2015) in that we do not use a strict color cut or bin GC RV measurements by radius. Rather, we follow the approach of Zhu et al. (2016) in modeling GC RVs as a mixture of Gaussians associated with each GC subpopulation. Here the mean velocity is the systemic velocity of the galaxy and the standard deviation is the predicted σ_J from the Jeans model associated with that subpopulation. We model the GC colors as being drawn from the mixture of Gaussians as described in Sec. 3.2.4.

Thus the likelihood for a particular GC measurement (with velocity $v_i \pm \delta v_i$ and $g-i$ color $c_i \pm \delta c_i$), under the assumption that it comes from a particular subpopulation, k, (described by a distinct density profile, anisotropy, and color distribution) is

$$\begin{aligned}&\mathcal{L}_k(v_i, \delta v_i, c_i, \delta c_i | \sigma_{J,k}(R_i)) = \\ &\frac{1}{\sqrt{2\pi(\delta v_i^2 + \sigma_{J,k}^2(R_i))}} \exp\left(-\frac{v_i^2}{\delta v_i^2 + \sigma_{J,k}^2(R_i)}\right) \\ &\times \frac{1}{\sqrt{2\pi(\delta c_i^2 + \sigma_{c,k}^2)}} \exp\left(-\frac{(c_i - \mu_{c,k})^2}{\delta c_i^2 + \sigma_{c,k}^2}\right)\end{aligned} \tag{3.20}$$

where $\mu_{c,k}$ and $\sigma_{c,k}$ are the mean and standard deviation of the color Gaussian for the k-th subpopulation, and $\sigma_{J,k}$ is the Jeans model prediction.

The likelihood for the GC data is therefore

$$\mathcal{L}_{\mathrm{gc}}(v_i, \delta v_i, c_i, \delta c_i) = \sum_{k \in \{b,r\}} \phi_k \mathcal{L}_k(v_i, \delta v_i, c_i, \delta c_i) \tag{3.21}$$

where ϕ_k is the mixture model weight for the k-th GC subpopulation, satisfying $\sum_k \phi_k = 1$. We note that the probability that an individual GC comes from a particular subpopulation is given by

$$P_k(v, \delta v, c, \delta c) = \frac{\phi_k \mathcal{L}_k(v, \delta v, c, \delta c)}{\sum_j \phi_j \mathcal{L}_j(v, \delta v, c, \delta c)} \ . \tag{3.22}$$

Putting all of the likelihoods together, our final joint likelihood is

$$\mathcal{L} = \prod_i \mathcal{L}_{\rm ls} \times \prod_i \mathcal{L}_{\rm ms} \times \prod_i \mathcal{L}_{\rm m} \times \prod_i \mathcal{L}_{\rm gc} \ . \tag{3.23}$$

In practice, we compute the log-likelihood.

$$\ln \mathcal{L} = \ln \mathcal{L}_{\rm ls} + \ln \mathcal{L}_{\rm ms} + \ln \mathcal{L}_{\rm m} + \ln \mathcal{L}_{\rm gc} \tag{3.24}$$

Our model has fifteen free parameters, listed in Table 3.3. The parameters are as follows: the scale density of the DM halo (ρ_s), the scale radius of the DM halo (r_s), the inner DM density log-slope (γ), the SMBH mass ($M_{\rm bh}$), the anisotropy of the field stars (β_s), the anisotropy of the blue GCs (β_b), the anisotropy of the red GCs (β_r), the distance (D), the central stellar mass surface density ($\Sigma_{0,*}$), the stellar mass effective radius ($R_{\rm e}$), the stellar mass Sérsic index (n_*), the weight for the longslit dataset ($\alpha_{\rm ls}$), the weight for the multislit dataset ($\alpha_{\rm ms}$), the weight for the GC dataset ($\alpha_{\rm gc}$), and the weight for the stellar mass surface density dataset ($\alpha_{\rm m}$).

The dynamical model and measurement model was constructed with SLOMO[4], a *python*-based code doing Jeans modeling of spherically symmetric systems. To sample our posterior probability distribution, we use *emcee* (Foreman-Mackey et al. 2013), an implementation of the affine-invariant Markov Chain Monte Carlo (MCMC) ensemble sampler described by Goodman & Weare (2010). We run our sampler with 128 walkers

---

[4] `https://github.com/adwasser/slomo`

Parameter	Unit	Prior	Fit value
$\log_{10}\rho_s$	$[\mathrm{M}_\odot\ \mathrm{kpc}^{-3}]$	$\mathcal{U}(3.0,\ 9.0)$	$6.65^{+0.74}_{-0.99}$
$\log_{10} r_s$	[kpc]	$\mathcal{U}(1.0,\ 3.0)$	$1.79^{+0.56}_{-0.36}$
γ	[—]	$\mathcal{U}(0.0,\ 2.0)$	$1.06^{+0.22}_{-0.37}$
$\log_{10}\ \mathrm{M}_{\mathrm{bh}}$	$[\mathrm{M}_\odot]$	$\mathcal{U}(0.0,\ 11.0)$	$5.11^{+3.11}_{-3.32}$
$\tilde{\beta}_s$	[—]	$\mathcal{U}(-1.5,\ 1.0)$	$-0.31^{+0.08}_{-0.10}$
$\tilde{\beta}_b$	[—]	$\mathcal{U}(-1.5,\ 1.0)$	$-1.08^{+0.32}_{-0.29}$
$\tilde{\beta}_r$	[—]	$\mathcal{U}(-1.5,\ 1.0)$	$0.23^{+0.25}_{-0.24}$
D	[Mpc]	$\mathcal{N}(26.0,\ 2.0)$	$21.01^{+1.37}_{-1.35}$
$\log_{10}\Sigma_{0,*}$	$[\mathrm{M}_\odot\ \mathrm{kpc}^{-2}]$	$\mathcal{U}(12.0,\ 13.0)$	$12.53^{+0.05}_{-0.06}$
$\log_{10} R_{\mathrm{eff},*}$	[arcsec]	$\mathcal{U}(1.0,\ 2.5)$	$1.41^{+0.06}_{-0.05}$
n_*	[—]	$\mathcal{U}(1.0,\ 8.0)$	$4.07^{+0.14}_{-0.13}$
α_{ls}	[—]	Exp	$1.89^{+0.47}_{-0.42}$
α_{ms}	[—]	Exp	$0.13^{+0.02}_{-0.02}$
α_{gc}	[—]	Exp	$1.89^{+1.27}_{-0.80}$
α_{sp}	[—]	Exp	$0.36^{+0.15}_{-0.12}$

Table 3.3: Model parameters. List of free parameters in our model with their best fit values. The fit values show the median of the posterior, along with the 68% credible region.

for 6000 iterations, rejecting the first 4800 iterations where the chains have not yet fully mixed. The traces of these walkers are shown in Appendix 3.7.1 in Fig. 3.17.

3.3.3 Parameterizations and Priors

For scale parameters such as ρ_s or r_s, we use a uniform prior over the logarithm of the parameter. For the anisotropy parameters, we re-parameterize to $\tilde{\beta} = -\log_{10}(1-\beta)$. By adopting a uniform prior over this symmetrized anisotropy parameter, we treat radial and tangential anisotropy values as equally probable. For the distance, we adopt a Gaussian prior as discussed in Sec. 3.2. In practice, we truncate this distribution for negative distances. Following Hobson et al. (2002) we adopt an exponential prior over all weight parameters.

3.3.4 Mock data test

After sampling from our posterior distribution, we validate our model by generating a mock dataset and performing the same inference as described above on these generated data. We emphasize that, rather than being a test of the appropriateness of our model, this is a test to see how well recoverable is our posterior distribution, given the assumed correctness of our model.

We take the median parameter values from Table 3.3 to be our "true" parameter values. For each stellar kinematic dataset, we use our dynamical model to generate new velocity dispersion values at each radial sample. We sample from a Gaussian with a standard deviation taken from the associated uncertainties in original data at the respective radial points to generate the mock stellar kinematic data. We generate mock stellar mass surface density measurements analogously.

For the GC dataset, we create a blue GC and red GC dataset by sampling from the respective model at each radial point for which we have data. We then assign each radial point to either be from the blue or the red subpopulation by comparing a draw from the standard uniform distribution with the ϕ_b value (from Table 3.2) in our model.

When generating each dataset, we scale the standard deviation by the respective best-fit weight values (the α hyperparameters from Table 3.3). The input uncertainties to the mock model are the same as those in the original data.

3.3.5 Caveats

Before presenting our results, we discuss a number of caveats to our work. We leave the relaxation of these assumptions for future work.

We have explicitly assumed that NGC 1407 has a spherically symmetric halo and stellar mass distribution. Wet major merger remnants can produce triaxial halos, with the expectation that the stars end up in an oblate spheroid with its minor axis perpendicular to the major axis of its prolate dark matter halo (Novak et al. 2006). However, NGC 1407 likely built up its halo through many minor mergers, and if the distribution of incoming merger orbits was largely isotropic as could be expected in a group environment, the galaxy could be expected to have a more spherical halo.

The Jeans equations assume that the tracers of the potential are in equilibrium. This requirement will be violated if there are recently-accreted tracers or if the relaxation time is relatively short. For the globular clusters in the outer halo, the long crossing times (on the order of $0.1 - 1$ Gyr) ensure that the relaxation time is long, but mean that any recently-accreted GCs will take a long time to phase mix. While there is not any blatantly obvious substructure in the GC kinematic data, a quantitative description of substructure in the tracer population would require a more rigorous determination of the completeness of our kinematic sample.

Since most of the stellar mass (and hence GCs) of the halo was built up by $z \sim 0.1$ (Buitrago et al. 2017, see also Rodriguez-Gomez et al. 2016), this would give GCs accreted prior to this point several crossing times to come into equilibrium. Efforts at quantifying the effect of non-equilibrium tracers on the mass profiles inferred from spherical Jeans modeling have found a systematic uncertainty on the order of 10-25% (Kafle et al. 2018; Wang et al. 2018).

We assume that the LOSVD is intrinsically Gaussian. More detailed models (e.g., Romanowsky & Kochanek 2001; Napolitano et al. 2014) would be necessary to make use of higher-order moments of the LOSVD.

Another major assumption we make is that the orbital anisotropies of our tracers are constant with radius. Generically, we would expect the anisotropy to take on different values at different distances from the center of the galaxy (e.g., Xu et al. 2017). There are a multitude of ways of parameterizing this anisotropy profile, including that presented by Merritt (1985) and that preferred by Mamon & Łokas (2005). However, given both the diversity of anisotropy profiles seen in simulated galaxies and the complexity evident in the Milky Way stellar anisotropy profile (e.g, Kafle et al. 2012), we opt for a simpler model that can be easily marginalized over. We show the result of modeling constant-β profiles given mock data generated with varying-β profiles in Appendix 3.7.2.3. This anisotropy assumption contributes the largest systemic uncertainty to the mass inference, and thus motivates the future study of orbital anisotropy in the outer stellar halos of galaxies.

To the extent that we expect any cores created in DM halos to have their own spatial scale independent of the scale radius of the halo, a more robust test to distinguish between a DM cusp and a core should treat these two radii separately. For instance, one can allow for a DM core out to some r_{core}, then have $\rho \propto r^{-1}$ between that core radius and the scale radius, r_s, then transition to having $\rho \propto r^{-3}$ as in a standard NFW halo.

We only have direct constraints on the stellar mass-to-light ratio, Υ_*, in the region studied by van Dokkum et al. (2017a), within $100''$. The stellar mass inferred for the outer regions of the galaxy is thus extrapolated from the Sérsic model that best fits the data in the inner region. We show a comparison inference for a radially-invariant Υ_* model in Appendix 3.7.2.4.

3.4 Results

We show the full posterior distribution in Fig. 3.18 in Appendix 3.7.1. We show the DM halo parameters in Fig. 3.8, where we have converted the halo parameters of ρ_s and r_s to the virial halo mass and concentration. We use the convention of defining the virial mass as the enclosed mass with an average density 200 times that of the critical density of the universe at $z = 0$.

$$M_{200} \equiv M(< r_{200}) = \frac{4\pi}{3} r_{200}^3 \left(200\rho_{\rm crit}\right) \tag{3.25}$$

The halo concentration is then defined as $c_{200} \equiv r_{200}/r_s$. With the Planck Collaboration et al. (2016) cosmological parameters, $\rho_{\rm crit}(z = 0) = 127.58\ \mathrm{M}_\odot\ \mathrm{kpc}^{-3}$. These halo parameters, along with other derived quantities, are reported in Table 3.4. We find strong evidence for a dark matter cusp in NGC 1407, with $\gamma = 1.0^{+0.2}_{-0.4}$. The posterior distribution has 92.9% of samples with $\gamma > 0.5$, disfavoring a cored-NFW profile.

Our best-fitting model predictions are shown along with the corresponding data for the stellar kinematics in Fig. 3.5, for the GC kinematics in Fig. 3.6, and for the

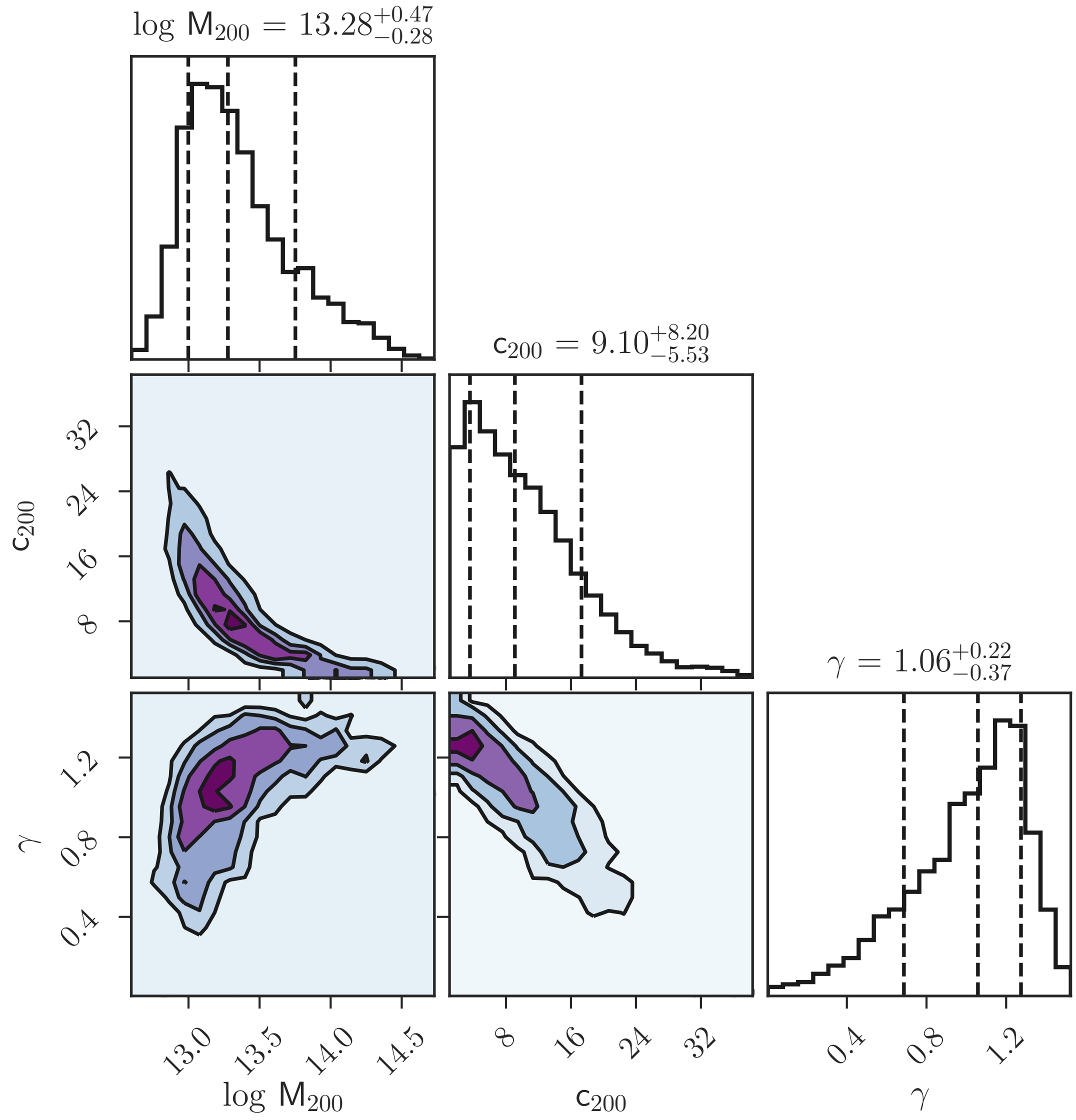

Figure 3.8: Posterior distribution of halo parameters. Histograms along the diagonal show the marginalized posterior distributions of halo mass (in $M_{\odot}$), halo concentration, halo inner density slope. The dashed vertical lines mark the 16th, 50th, and 84th percentiles. The contours (at levels equivalent to 0.5, 1, 1.5 and 2 σ for a 2D Gaussian distribution) show the covariances between these parameters. We note the strong degeneracy among all three halo parameters.

	Unit	Value
$\log_{10} M_{200}$	[M$_\odot$]	$13.3^{+0.5}_{-0.3}$
c_{200}	[—]	9^{+8}_{-6}
r_{200}	[kpc]	560^{+250}_{-110}
$\log_{10} M_*$	[M$_\odot$]	$11.34^{+0.06}_{-0.07}$
$f_{\rm DM}$	[—]	$0.91^{+0.01}_{-0.01}$

Table 3.4: Derived parameters. List of quantities derived from free parameters. γ is listed in Table 3.3.

stellar mass surface density in Fig. 3.2.

We show the decomposition of the enclosed mass profile into stellar, DM, and BH components in Fig. 3.9. Here we see that the overlap in the spatial regions probed by the GC and stellar kinematic data cover the crucial region where the DM halo becomes gravitationally dominant over the stellar mass. As anticipated, we have weak constraints on the mass of the central SMBH, which we have treated as a nuisance parameter in the modeling.

3.4.1 Mock data test results

Our inference on the mock data shows that most of the parameters used to generate the mock data are well recovered. We show the recovery of our input halo model parameters in Fig. 3.10, and we show the full parameter set in Appendix 3.7.1 in Fig. 3.19. We find excellent recovery of the halo mass parameters. However, our recovery of the stellar anisotropy is biased towards more tangential orbits.

Since these mock data were generated using the model which was used for

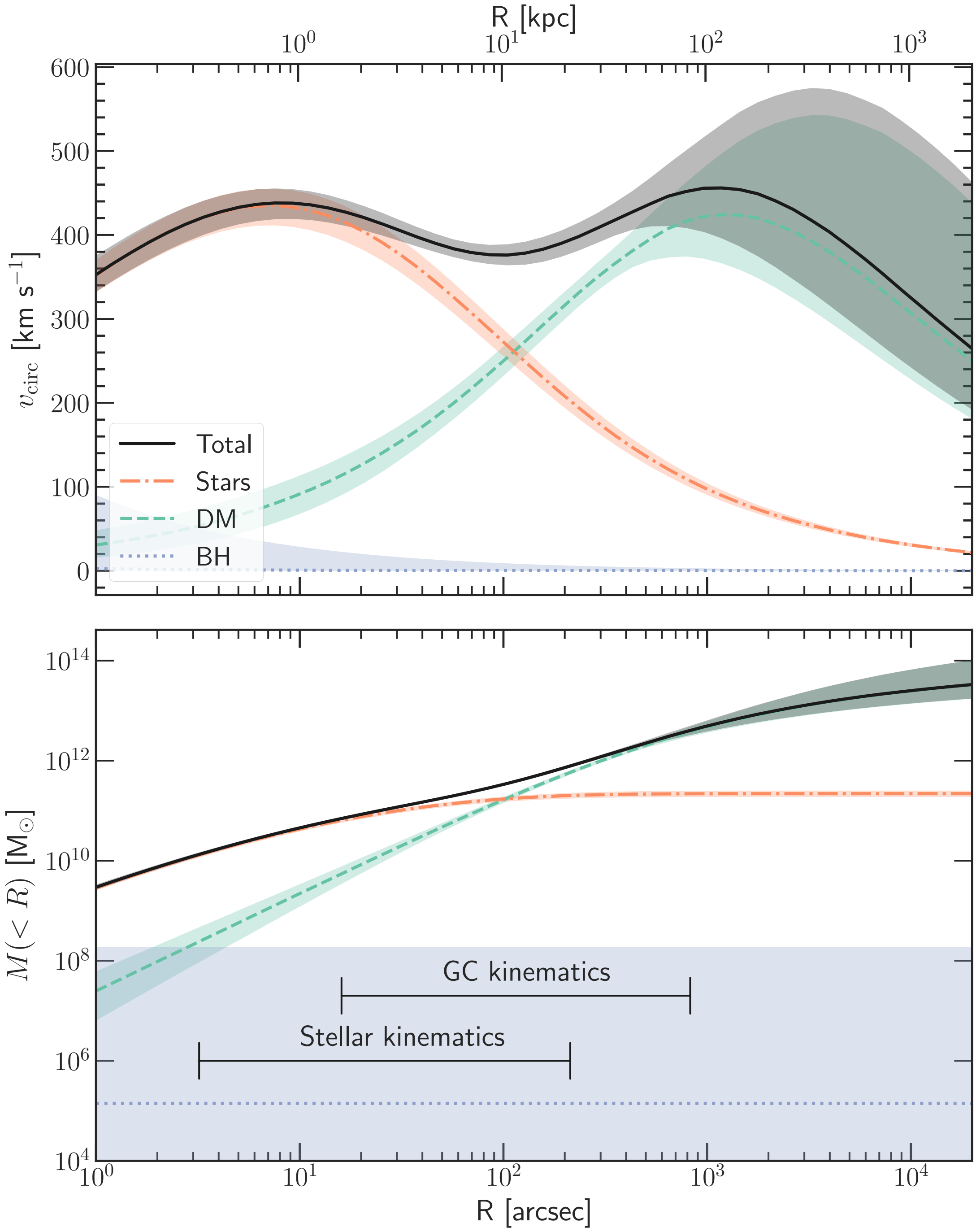

Figure 3.9: Top: circular velocity profiles of the mass components of the best fit model, with the width of the curve showing the central 68% of samples. Bottom: same, but showing the enclosed mass of each component. The horizontal bars indicate where we have constraints from stellar and GC kinematics.

fitting, the successful recovery merely validates our statistical uncertainties; we defer an in-depth discussion of the systematic uncertainties of our modeling assumptions to Appendix 3.7.2. The largest quantified source of systematic uncertainty in the halo inner density slope is from the choice of anisotropy profile, which lowers γ by ~ 0.5.

3.4.2 Literature comparisons for NGC 1407

In this section, we compare our mass inferences with those from some recent observational studies. We compare both the dark matter fraction,

$$f_{\rm DM}(< R) = 1 - M_*(< R)/M_{\rm tot}(< R) \ , \tag{3.26}$$

and the circular velocity

$$v_{\rm circ}(R) = \sqrt{GM/R} \ . \tag{3.27}$$

The dark matter fractions and circular velocity profiles from Pota et al. (2015), Deason et al. (2012), Su et al. (2014), and Alabi et al. (2017) are compared with our results in Fig. 3.11. These are both quantities which vary with radius, so we plot values at a given angular radius on the sky to make a proper comparison. For the dark matter fractions, we scale the reported measurements by

$$1 - f_{\rm DM} \rightarrow \left(\frac{d_{\rm us}}{d_{\rm them}}\right)(1 - f_{\rm DM}) \tag{3.28}$$

to account for the differences in their adopted distances. The stellar mass will scale with two factors of the distance for the luminosity distance dependence, and the dynamical mass will scale inversely with one factor of distance, leading to the scaling of the baryon fraction by one factor of the adopted distance.

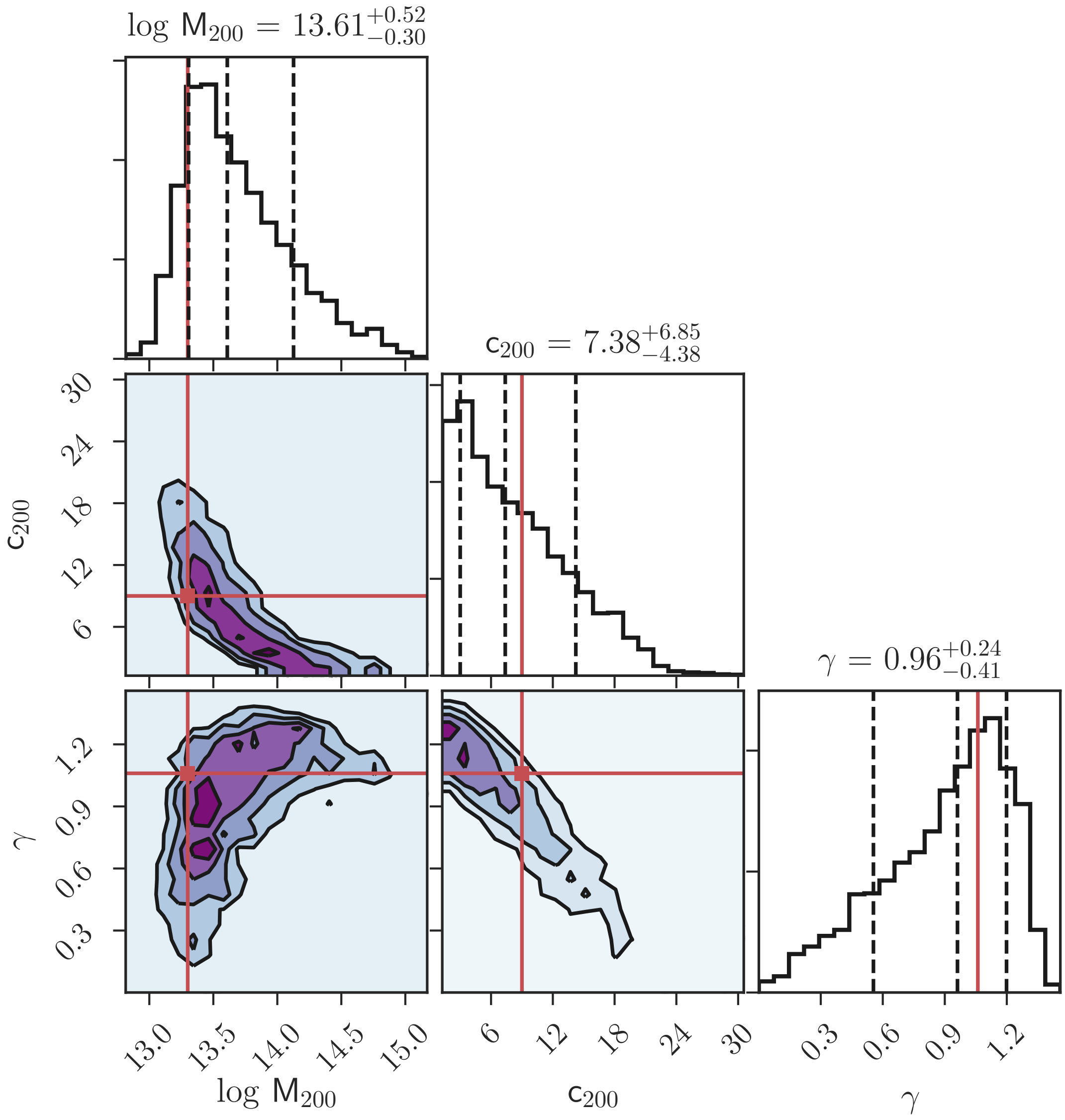

Figure 3.10: Posterior probability distribution from modeling our mock dataset. Red solid lines show the model parameters used to generate the dataset.

Our total mass result is consistent with that of Pota et al. (2015), who adopted a distance of 28.05 Mpc. This is to be expected, given that we use a similar dataset and modeling technique. They reported $f_{\rm DM} = 0.83^{+0.04}_{-0.04}$ at $500''$, slightly below the value of $0.90^{+0.01}_{-0.02}$ that we find at the same radius.

Deason et al. (2012) used a distribution function-maximum likelihood method to constrain the mass of 15 ETGs using PNe and GCs. They assumed a distance to NGC 1407 of 20.9 Mpc, and they modeled the total mass as a power law. For an assumed Salpeter IMF ($6 < \Upsilon_{*,B} < 10$), they found $f_{\rm DM} = 0.67 \pm 0.05$ within $285''$, whereas we find $f_{\rm DM} = 0.82^{+0.02}_{-0.03}$.

Su et al. (2014) modeled the X-ray emission of hot gas surrounding NGC 1407. Under the assumption that the gas is in hydrostatic equilibrium, they constrained the total mass profile of the galaxy and decomposed this into stellar, gas, and DM components. They modeled the DM halo using an NFW profile, and assumed a mass-to-light ratio of $\Upsilon_{\rm K} = 1.17$ M$_\odot$ / L$_{\odot,K}$ and a distance of 22.08 Mpc. Within the inner $934''$(100 kpc at their adopted distance), they found $f_{\rm DM} = 0.94$. We find $f_{\rm DM} = 0.95^{+0.01}_{-0.01}$ within the same enclosed area.

Alabi et al. (2017) also used GCs as tracers, but applied the tracer mass estimator technique of Watkins et al. (2010) to 32 ETGs, including NGC 1407. They assumed a distance of 26.8 Mpc. They reported results for multiple assumptions for β, and we compare with their result ($f_{\rm DM} = 0.82 \pm 0.04$ at 60.7 kpc) that assumes an anisotropy of $\beta = 0$ for all the GCs (though we note that their value of $f_{\rm DM}$ only varies by 0.04 between the $\beta = -0.5$ and the $\beta = 0.5$ cases).

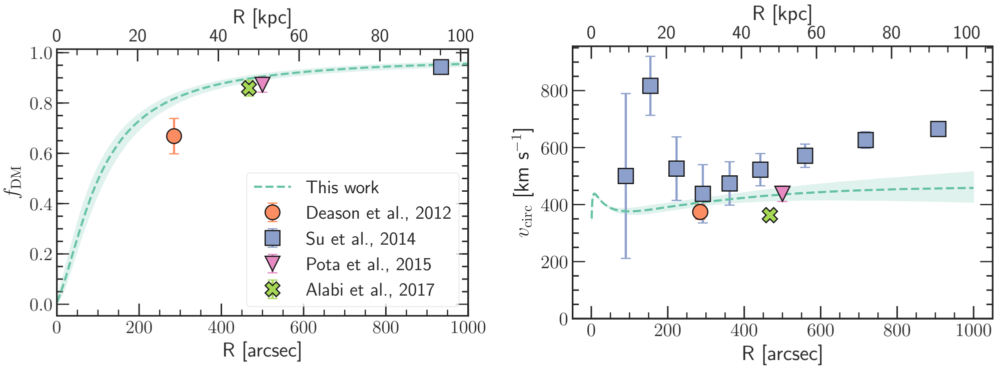

(a)

(b)

Figure 3.11: Left: Dark matter fraction as a function of radius, compared with measurements from the literature. Right: Circular velocity as a function of radius, compared with measurements from the literature. The width of the curves indicate the central 68% of samples.

We find good agreement in the measured DM fractions shown in Fig. 3.11, though there is a slight offset between our value and that of Deason et al. (2012). Our total mass estimate is largely in agreement with those of other dynamical studies of NGC 1407, though we find that the X-ray mass measurements of Su et al. (2014) are noticeably larger at $R \sim 20$ kpc and also at $R \gtrsim 50$ kpc. This is consistent with other X-ray studies of NGC 1407 (e.g., Zhang et al. 2007; Romanowsky et al. 2009; Das et al. 2010, though see Humphrey et al. 2006), and it suggests systematic differences in the X-ray and the dynamical modeling.

Disagreements between X-ray and dynamical mass measurements have been seen before in numerous studies of ETGs, and are sometimes attributed to hot halo gas being out of hydrostatic equilibrium or supported by non-thermal pressures (Churazov et al. 2010; Shen & Gebhardt 2010). Furthermore, directional gas compression and decompression can cause asymmetric deviations from optically-derived mass measurements (Paggi et al. 2017).

3.4.3 Halo mass–concentration and stellar mass–halo mass relations

Given that we find a nearly-NFW halo, we compare our virial mass and concentration with the M_{200}–c_{200} relation of relaxed NFW halos from Dutton & Macciò (2014). This relation, along with measurements from the literature, are shown in Fig. 3.12. Here we see good agreement between our median DM halo parameters and those expected from the mass–concentration relation.

Fig. 3.13 compares our inference of the halo mass and stellar mass with the

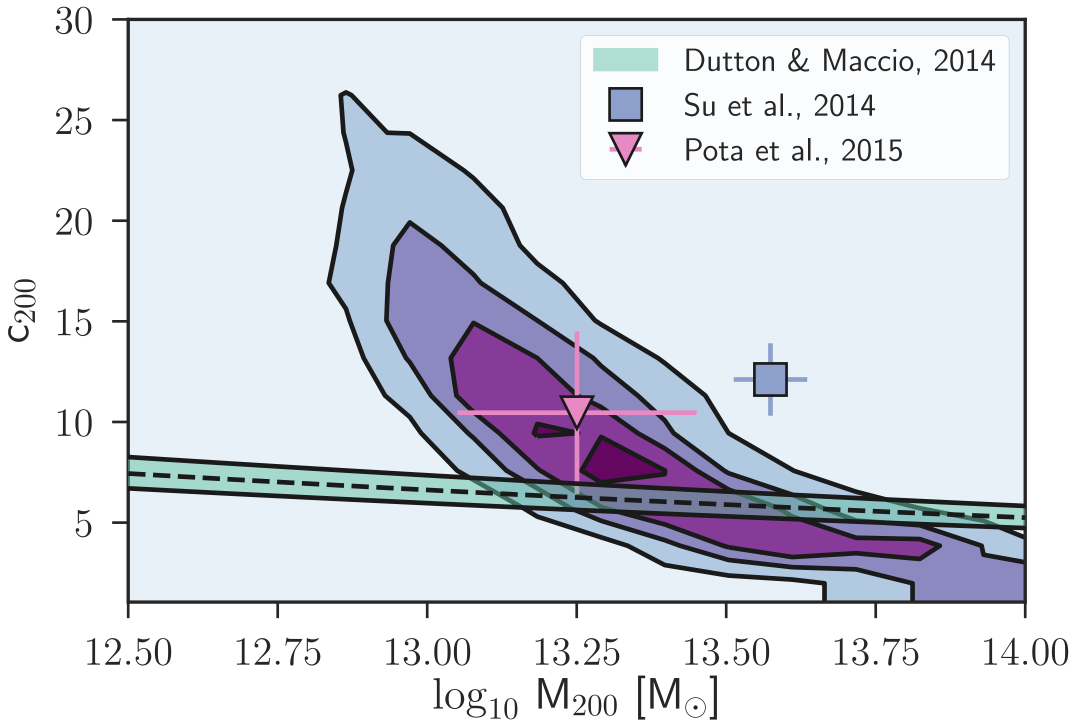

Figure 3.12: Posterior distribution of halo mass and concentration for NGC 1407 shown in contours. The green line shows the relation from Dutton & Macciò (2014) with characteristic scatter.

M_*–$M_{\rm halo}$ relation from Rodríguez-Puebla et al. (2017). Here we have re-calculated our virial mass to match the definition used by Rodríguez-Puebla et al. at $z = 0$, with $h = 0.678$ and $\Delta_{\rm vir} = 333$. We find that NGC 1407 lies slightly above the M_*–$M_{\rm halo}$ relation from Rodríguez-Puebla et al. (2017). However, we have indicated the shift in stellar mass that would occur if they had adopted a Salpeter IMF rather than a Chabrier IMF. We see that this Salpeter IMF stellar mass–halo mass relation is consistent with our inference.

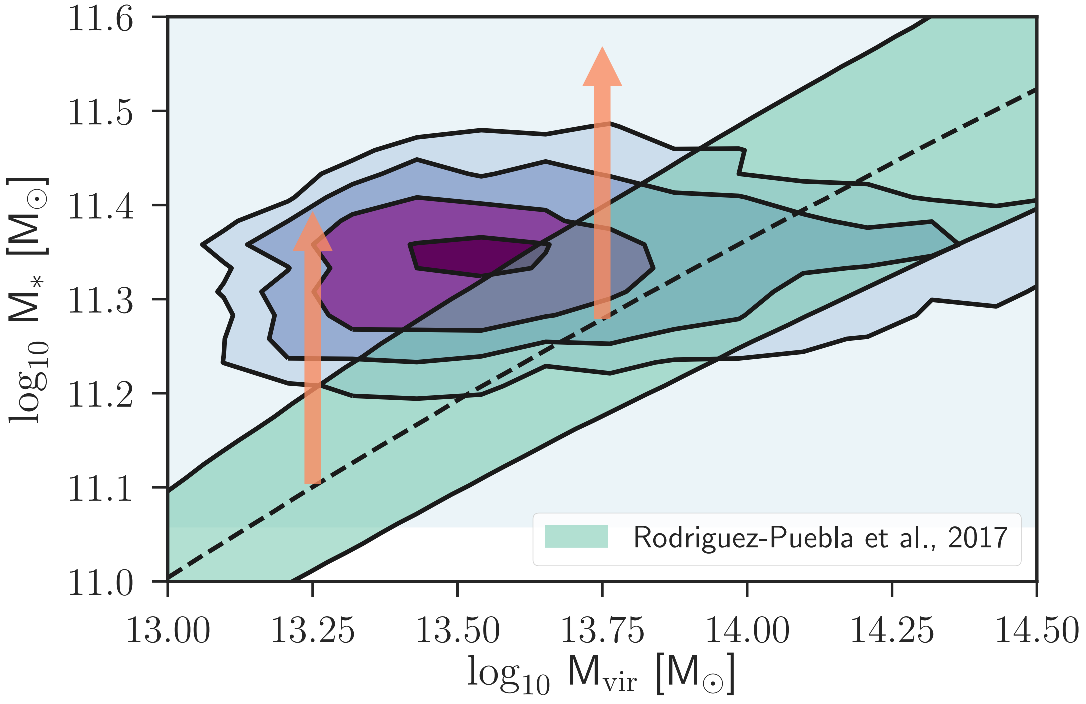

Figure 3.13: Posterior distribution of stellar mass and halo mass for NGC 1407 shown in contours. The green line shows the stellar mass-halo mass relation from Rodríguez-Puebla et al. (2017) with uncertainties propagated for the 68% credible interval. The orange arrows show change in stellar mass from a Chabrier (2003) IMF to a Salpeter (1955) IMF, with a resulting shift for the prediction of 0.3 dex.

3.4.4 Distance

One unique aspect of this work is that we freely vary the distance, informed by a weak Gaussian prior from previous redshift-independent distance measurements (see Section 3.2). With the stellar mass-to-light ratio known to a reasonable degree of uncertainty, this becomes a non-trivial systematic uncertainty, as indicated by the covariance of distance with the inner DM density slope, the stellar anisotropy, and the stellar mass distribution parameters (Fig. 3.18).

We find a distance of $21.0^{+1.4}_{-1.4}$ Mpc. This is a notable offset from our prior distribution on distance, which was a Gaussian with a mean of 26 Mpc and a standard deviation of 2 Mpc. Our result is inconsistent with the Tully et al. (2013) combined SBF/Fundamental Plane measured distance. However, our inferred distance is closer to the luminosity distance of 24.2 ± 1.7 Mpc at the observed redshift, and in full agreement with the Forbes et al. (2006) distance constraint from modeling the globular cluster luminosity function. We ran tests fixing the distance to the mean of our prior distribution, and found a lower value of γ, consistent with the negative covariance between the two parameters seen in Fig. 3.18. Thus to the extent that our adopted distance is considered low (compared to the wide range of literature values), we find a robust upper bound on γ.

3.4.5 SMBH

Rusli et al. (2013) modeled the stellar kinematics of 10 ETGs to constrain their super-massive black hole (SMBH) masses. For NGC 1407, they found $M_{\mathrm{BH}} =$

$4.5^{+0.9}_{-0.4} \times 10^9~M_\odot$. Since we, by design, do not model the detailed dynamics of stellar orbits near the SMBH, we only get weak constraints on its mass. However, our constraints indicate that the SMBH mass of NGC 1407 could be somewhat lower. With a uniform prior for $\log_{10} M_{\rm bh} < 11$, we find that the posterior distribution on $M_{\rm bh}$ cuts off at approximately $2 \times 10^9~{\rm M}_\odot$.

While Rusli et al. (2013) treated the systematics of having a DM halo in their inference of the SMBH mass, they treated the stellar mass as a constant Υ_* times the stellar luminosity profile. NGC 1407 lies slightly above standard $M_{\rm BH}$–σ relation, by a factor of approximately 1.5 times the intrinsic scatter (McConnell et al. 2013). It is conceivable that some of the mass inferred for the SMBH is in fact associated with a more bottom-heavy IMF in the center of the galaxy.

McConnell et al. (2013) investigated the effect of radial Υ_* gradients on the inferred masses of SMBHs, finding that a log-slope, $\mathrm{d}\log\Upsilon_*/\mathrm{d}\log r$, which varied from -0.2 to 0.2 had little impact on the inferred $M_{\rm bh}$. However, the radial variation in Υ_* for NGC 1407 appears to be somewhat steeper, with a log-slope of ~ -0.3 (van Dokkum et al. 2017a).

3.5 Discussion

3.5.1 The γ–$M_{\rm halo}$ relation

Few measurements have been made of the inner DM density slope for massive ETGs for reasons discussed in Sec. 3.1. Here we discuss both the measurements and predictions for galaxies in this mass regime and for galaxies across a broad range of masses, focusing first on giant elliptical galaxies.

Pota et al. (2015) also modeled NGC 1407 using GC and stellar kinematics, finding $\gamma \sim 0.6$. We attribute the difference between this value and our own inference to be primarily due to our more precise determination of the stellar mass distribution and also to fitting distance as a free parameter. Agnello et al. (2014) modeled the dynamics of the GC system of M87, the Virgo cluster central galaxy. They found that the behavior of the inner DM density profile followed a power law, $\rho \sim r^{-\gamma}$ with $\gamma \approx 1.6$. Oldham & Auger (2016, 2018a) also modeled the dynamics of M87, but found evidence for a DM core ($\gamma \lesssim 0.5$). They attributed this difference to their inclusion of central stellar kinematics in the inference, although we also note that they used a less restricted GC spectroscopic sample than Agnello et al.. Zhu et al. (2016) modeled the dynamics of field stars, GCs, and planetary nebulae (PNe) in the massive elliptical galaxy NGC 5846 (based in part on SLUGGS data). They ran models with a fixed DM core and with a fixed DM cusp, finding a preference for the model with the cored halo.

Thomas et al. (2007) modeled the stellar dynamics of 17 ETGs in the Coma cluster with both NFW halo models and LOG halo models (which include a central core), though they were unable to distinguish between the two scenarios with the available data. Napolitano et al. (2010) looked at trends of central DM density and radius for a large sample of low-redshift ETGs, finding evidence for an inner DM density log-slope of ~ 1.6, in turn suggesting the need for baryonic processes to contract the halo. While this result is fairly independent of assumptions about the IMF, it is based on stacked galaxy data and thus it cannot be used to provide γ for individual galaxies.

In Fig. 3.14 we show how NGC 1407 compares with the observed and predicted dependence of γ on halo mass. We restrict our observational comparisons in this figure to studies which allowed for a variable inner DM density log-slope. We emphasize that due to the varied definitions, methods of inference, and sources of data used to constrain γ, Fig. 3.14 is intended merely as a schematic of what we might expect of DM halos across a wide mass range ($10.5 < \log_{10} M_{200}/M_{\odot} < 16$).

We summarize the cited observational studies shown in this figure. Chemin et al. (2011) modeled the rotation curves of spiral galaxies with Einasto halos. They reported the log-slope of the best fit Einasto density profile at $\log(r/r_s) = -1.5$, and we compare with their result which assumes a Kroupa IMF. Adams et al. (2014) modeled the gas and stellar dynamics of dwarf galaxies using both a gNFW profile and a cored Burkert profile. Newman et al. (2013b,a) modeled galaxy clusters and groups with constraints from lensing and stellar dynamics with a gNFW profile, finding halos with both NFW cusps and slightly shallower ($\gamma \sim 0.5$) slopes. Oldham & Auger (2018b) modeled strongly-lensed ETGs, confirming the decreasing γ trend at large halo masses. We remove the two systems (J1446 and J1606) for which they find minimal constraints from the lensing data.

The observations of high-mass galaxy clusters suggest a decreasing trend of γ with $M_{\rm halo}$. NGC 1407 is consistent with this trend, though it may lie on the turnover region that would be necessary to connect to the increasing trend of γ at the low-mass regime. In subsequent work we will check where this turnover happens with a larger

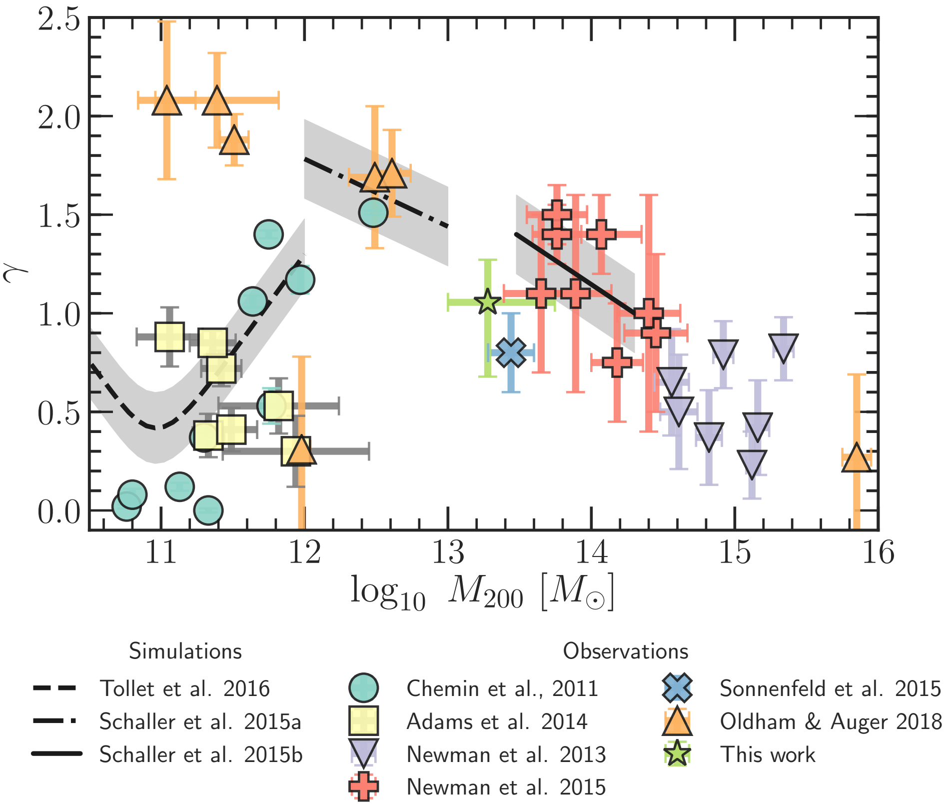

Figure 3.14: The γ–M_{halo} relation from a wide range of theoretical and observational studies. We see that ΛCDM simulations with hydrodynamics (black lines) largely agree with observations (multi-colored points, described in text). DM core creation occurs most strongly for 10^{11} $\mathrm{M}_\odot$ halos, with an additional trend towards shallower halos at the highest halo masses. NGC 1407 follows the general trend of steepening density slope with decreasing halo mass, thought the median value of γ is slightly below what would have been interpolated from both theory and observation.

sample of galaxies down to lower halo masses.

Simulations that constrain the relation shown in Fig. 3.14 must address physics across a wide range of spatial scales. Tollet et al. (2016) used the NIHAO hydrodynamical cosmological zoom-in simulations to make predictions at $\log M_{200}/M_{\odot} < 12$. They measured the DM density profiles for their galaxies and reported the log-slope in the region between 1% and 2% of the virial radius. Schaller et al. (2015a,b) used the EAGLE simulations to make predictions for higher-mass galaxy clusters. They fitted a gNFW density profile to their halos and reported the inner asymptotic log-slope.

We see two emerging trends in the γ–$M_{\rm halo}$ relation. At the range of dwarf and spiral galaxies ($M_{200} \sim 10^{11} - 10^{12}$ M$_{\odot}$), γ is predicted to increase with halo mass, though there is a large range of observed γ values in the observations. For hydrodynamic simulations in this regime, DM core creation is associated with bursty star formation (Tollet et al. 2016). Thus, this trend can be understood as the energy associated with baryonic feedback becoming less and less significant relative to the depth of the potential associated with the halo. At the range of galaxy groups and clusters ($M_{200} \sim 10^{13} - 10^{16}$ M$_{\odot}$), there is a decreasing trend of γ with halo mass. This has often been interpreted as increased dynamical heating for halos which have experienced more satellite mergers (El-Zant et al. 2004; Laporte & White 2015).

Massive elliptical galaxies like NGC 1407 ought to have the steepest inner density profiles with $\gamma > 1$, owing to the fact that they lie at the intersection of the two competing trends discussed above (i.e., minimal heating from stellar feedback and mergers), and due to the effect of adiabatic contraction (Blumenthal et al. 1986; Gnedin et al. 2004).

We see that our median value for γ falls slightly below the predictions from Schaller et al. (2015a,b) (though consistent within the uncertainty). However, this value is consistent with the results from the analysis of Sonnenfeld et al. (2015), who found an average inner DM density slope of $\gamma = 0.80^{+0.18}_{-0.22}$ for a sample of 81 strongly lensed massive ETGs.

The above discrepancy between theory and observation could be an indication that some mechanism is needed to prevent the steepening of the halo density profile. Self-interacting dark matter (SIDM) could be one such mechanism, as the non-zero collisional cross-section allows for heat transfer in the inner regions of the halo. Rocha et al. (2013) compared the structure of self-interacting DM halos with that of standard CDM halos for two cross-sections, $\sigma/m = 0.1$ cm^2 g^{-1} and $\sigma/m = 1$ cm^2 g^{-1}. They found that large cross-sections lead to DM cores within ~ 50 kpc. Our result disfavors this large a cross-section, though we note that it is difficult to rule out their result for the smaller cross-section. In addition, the lack of baryonic physics in these simulations makes a proper comparison difficult.

Di Cintio et al. (2017b) used hydrodynamic simulations to explore the effect of SIDM on the baryonic and DM density distributions of Milky Way-mass galaxies. They used a significantly higher cross-section, $\sigma/m = 10$ cm^2 g^{-1}, than Rocha et al.. They reported the log-slope of the density profiles between 1% and 2% of the virial radius for both standard CDM simulations and SIDM runs and found a decrease of $0.5 - 0.7$ in γ from the standard run to the SIDM one.

Alternatively, feedback from AGNs could be an important mechanism for transferring energy to the central DM (Martizzi et al. 2013; Peirani et al. 2017), analogous to the way that bursty star formation induces potential fluctuations in low mass galaxies (Pontzen & Governato 2012). Even in absence of any AGN feedback, dry merging of galaxies can slightly decrease the DM density slope, though not enough to fully counteract the effects of adiabatic contraction (Dutton et al. 2015).

Given the paucity of observational constraints and the non-trivial systematic uncertainties in measuring the halo density slope, any connection between our best-fit value of γ and any particular physical cause is largely speculation at this point. However, this ambiguity motivates further work to fill in the remaining observational gaps.

3.5.2 Halo anisotropy

The orbital anisotropy of stars and star clusters in the outer stellar halos of galaxies has received much attention in recent years. We find that the blue (metal-poor) GCs have tangentially-biased orbits ($\beta_{\rm blue} \lesssim -4$), while the red (metal-rich) GCs have radially-biased orbits ($\beta_{\rm red} \sim 0.4$).

Dynamical differences between the red and blue GC subpopulations have been seen before. Pota et al. (2013) calculated the kurtosis of the GC LOSVD as a proxy for orbital anisotropy for a sample of 12 ETGs. While they found that the kurtosis values for individual galaxies were largely consistent with isotropic orbits, they found that the blue GCs had, on average, negative kurtosis (suggesting tangential anisotropy) in the outskirts while red GCs had, on average, positive kurtosis (suggesting radial anisotropy) in the outer regions.

Pota et al. (2015) also found tangential blue GCs and radial red GCs for NGC 1407 using Jeans models; we note that we have modeled the same GC dataset as the Pota et al. study.

There have been numerous studies of the dynamics of the GC system of M87. Romanowsky & Kochanek (2001) used the Schwarzschild orbit library method to model the GCs and stars. They found that the orbits of the GCs as a whole system were near isotropic at large radii. Zhu et al. (2014) used made-to-measure models to infer the orbits of GCs as a single population, and found orbits that were similarly near-isotropic across most of the spatial extent of the galaxy. Agnello et al. (2014) found evidence for three GC subpopulations. For both the bluest and reddest subpopulations they found mildly tangential orbits at 1 $R_{\rm e}$, while they found the intermediate subpopulation to have slightly radial orbits at the same distance. Zhang et al. (2015) modeled the dynamics of the red and blue GC subpopulations separately using Jeans models. They found slightly tangential ($\beta \sim -0.5$) blue GCs in the inner and outer regions of the galaxy, and radially-biased ($\beta \sim 0.5$) red GCs. Oldham & Auger (2016) also modeled blue and red GC subpopulations of M87, finding mildly radially-biased orbits for both blue and red GCs. Overall the consensus for halo anisotropy in M87 seems to be that, if red and blue GCs have different orbital anisotropies, the blue GC orbits are somewhat more tangentially-biased.

Zhu et al. (2016) used made-to-measure models to constrain the β-profiles of stars, PNe, and GCs in NGC 5846, following up on earlier Jeans modeling work by

Napolitano et al. (2014). They found the opposite trend for this galaxy compared with NGC 1407, with tangentially-biased or isotropic red GCs and radially-biased blue GCs. The PNe trace the field star population in the center and go from radial to marginally tangential orbits out to ~ 30 kpc.

We compare some of these studies that separately analyze blue and red GCs in Fig 3.15. There seems to be a diversity of results, with some studies finding the blue GCs to have more tangential orbits than the red GCs, and others finding the opposite result. However, none of the studies find both red and blue GCs in a single galaxy to have radial orbits (the upper right quadrant of the figure).

This result is puzzling, since the outer stellar halos of galaxies built up by mergers are expected to produce radially-biased orbits (e.g., Dekel et al. 2005; Oñorbe et al. 2007; Prieto & Gnedin 2008), and the majority of blue GCs have most likely been brought into the present day host galaxy via satellite accretions.

Röttgers et al. (2014) used hydrodynamic zoom simulations from Oser et al. (2010) to examine the connection between orbital anisotropy and the fraction of stars formed in-situ. They found that accreted stars were more radially biased than in-situ stars. To the extent that the blue and red GCs could be expected to trace accreted and in-situ populations of the stellar halo, our result that blue GCs have an extreme tangential bias is an interesting counter-example to their result.

One possible explanation for the tangential orbits is that we are seeing a survival-bias effect, whereby GCs on radially-biased orbits are more likely to be disrupted, as they reach more deeply into the center of the potential. However, for this scenario to

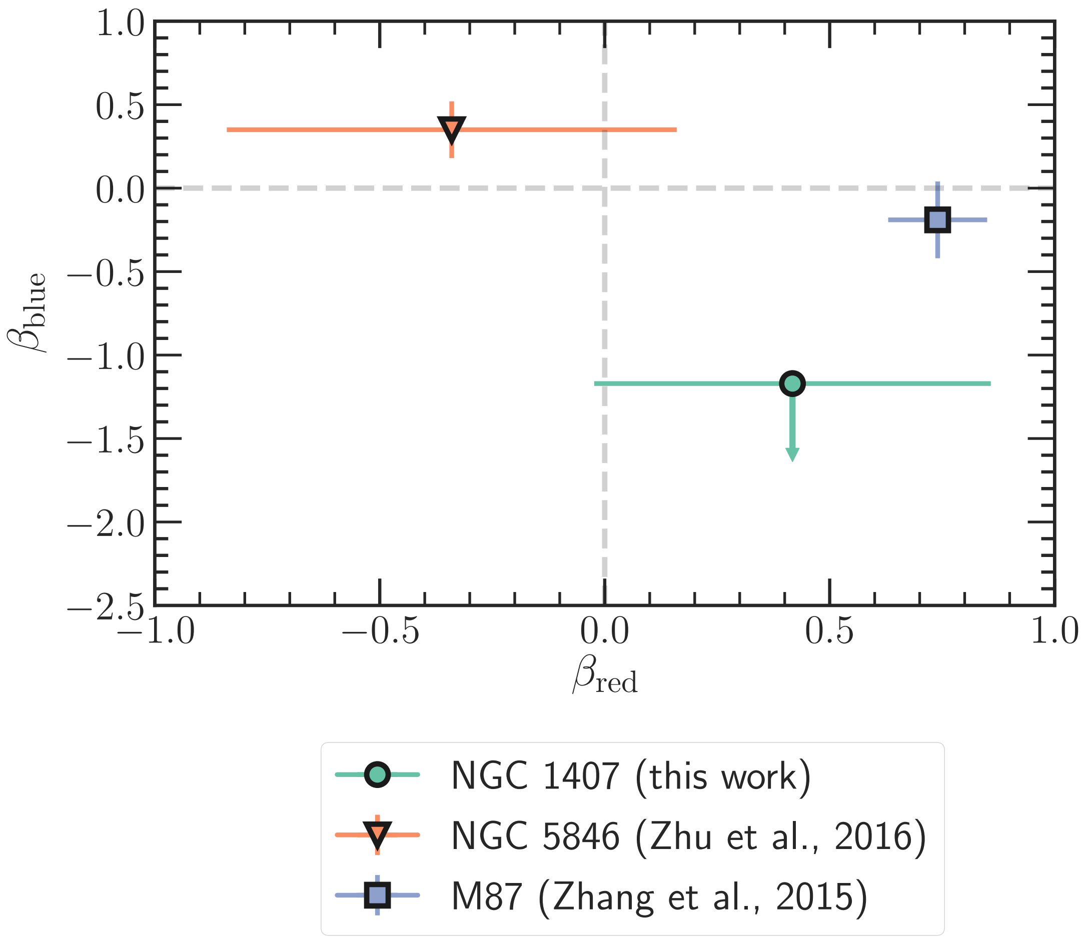

Figure 3.15: Blue GC orbital anisotropy versus red GC anisotropy for NGC 1407 compared with those of NGC 5846 (Zhu et al. 2016) and M87 (Zhang et al. 2015). For M87, we show their result at a distance of 100 kpc. Isotropic values of β are indicated by the dashed grey line.

work, the metal-poor GCs would have to be in place longer than the metal-rich GCs, contrary to the expectation that the former are accreted and the latter form in-situ.

Another possibility would be a dynamical effect noted by Goodman & Binney (1984) whereby gradual accretion of mass at the center of a spherical system will preferentially circularize orbits in the outer regions.

The origin of this peculiar halo anisotropy remains an open question, deserving further study.

3.5.3 Stellar mass distribution

Since we have chosen to model the stellar mass of the galaxy as its own Sérsic profile, as opposed to a constant mass-to-light ratio multiplied by the enclosed luminosity, we have a handle on how the stellar mass distribution differs from the stellar light distribution. We find a half-mass effective radius of $26^{+4}_{-3}{}''(2.7^{+0.5}_{-0.4}$ kpc when marginalizing over distance), much smaller than the B band half-light effective radius of $100''(10.2^{+0.7}_{-0.7}$ kpc).

This relative concentration of the stellar mass is intriguingly similar to the situation at high redshift. van der Wel et al. (2014) used results from 3D-HST and CANDELS to trace the evolution in the stellar size–mass relation out to $z \sim 3$, finding a strong size evolution of ETGs at fixed mass of $R_{\rm e} \propto (1+z)^{-1.48}$. We compare our measurement of the stellar half-mass radius with the ETG relations from van der Wel et al. (2014) in Fig. 3.16. We see that the stellar mass distribution of NGC 1407 most closely matches the light distribution of compact galaxies at $z \sim 2$.

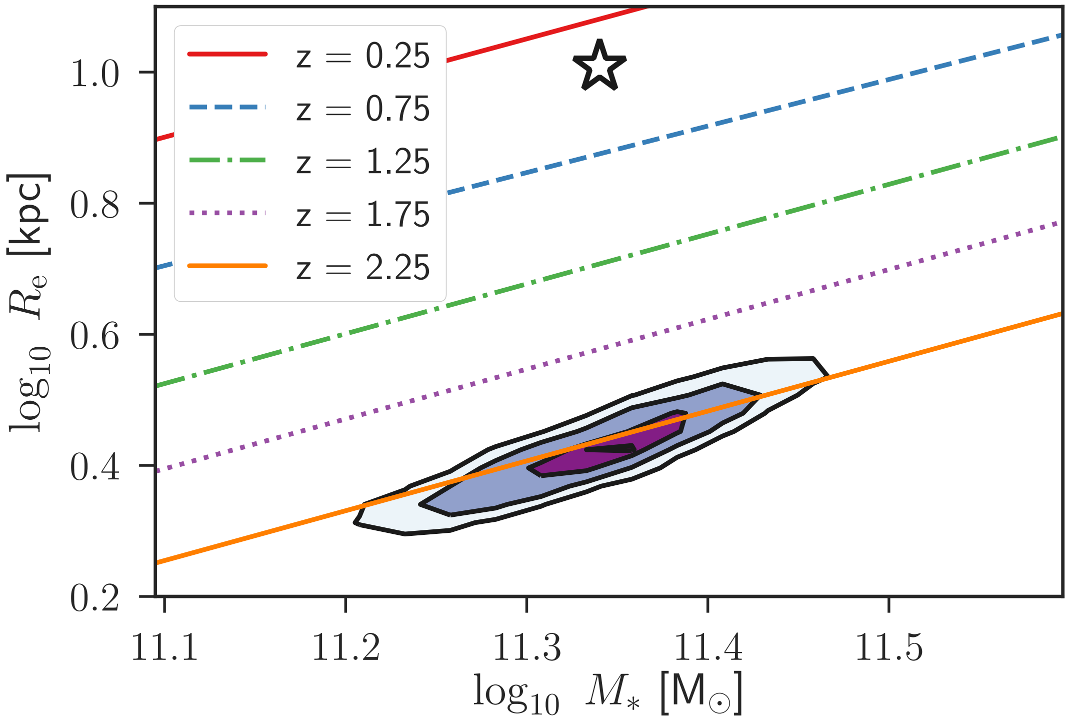

Figure 3.16: Stellar size–mass relations at different redshifts from van der Wel et al. (2014), compared with our inference for NGC 1407 (purple contours). The B band R_e value of NGC 1407 is indicated by the star.

We note that our modeling may be biased towards smaller effective radii, as we are only fitting to the stellar mass surface density profile where we have data at $R < 100''$. If the mass-to-light profile does remain at a Milky Way-like value past $1R_{\mathrm{e}}$, then this would result in a less compact Sérsic fit than we find here.

3.6 Conclusions

We have presented a new analysis of the dynamics of the massive elliptical galaxy NGC 1407. We constrained the dynamical mass of the galaxy using a variety of datasets, including metal-rich and metal-poor globular cluster velocity measurements, the stellar velocity dispersion measurements from longslit and multislit observations, and the spatially-resolved mass-to-light ratio from stellar population models.

We found the following:

1. The dark matter virial mass and concentration are well-matched to expectations from ΛCDM.
2. The dark matter halo of NGC 1407 likely has a cusp ($\gamma = 1$). This is shallower than expected for a normal ΛCDM halo with adiabatic contraction, although a larger sample size is needed to constrain the physical origin of this result.
3. The blue (metal-poor) globular clusters of NGC 1407 are on tangentially-biased orbits (contrary to expectations for accreted stellar mass), while the red (metal-rich) clusters are on slightly radially-biased orbits.

4. The stellar mass distribution is significantly more compact than the stellar luminosity distribution, reminiscent of compact "red nugget" galaxies at high redshift.

We are just beginning to probe the $\gamma - M_{\rm halo}$ relation in the regime of giant early-type galaxies. Here we have shown that it is feasible to populate this parameter space with individual galaxies, and we intend to follow up this work with a larger study of galaxies from the SLUGGS survey.

3.7 Appendix

3.7.1 Markov Chain Monte Carlo Sampling

Here we show the detailed results of our sampling of the posterior probability distribution for the model parameter space described in Sec. 3.3.

3.7.2 Systematics tests

We performed a number of tests to investigate the systematic uncertainty on the recovered DM halo parameters. For each of the tests described below, we plot a comparison of the DM halo parameter posterior distribution (re-parameterized $\log_{10}(M_{200}/M_\odot)$ and c_{200}) of the reference model described in the main text (in purple) with the distribution found when doing the specified test (in red). The contours are drawn at the 1 and 2 sigma levels.

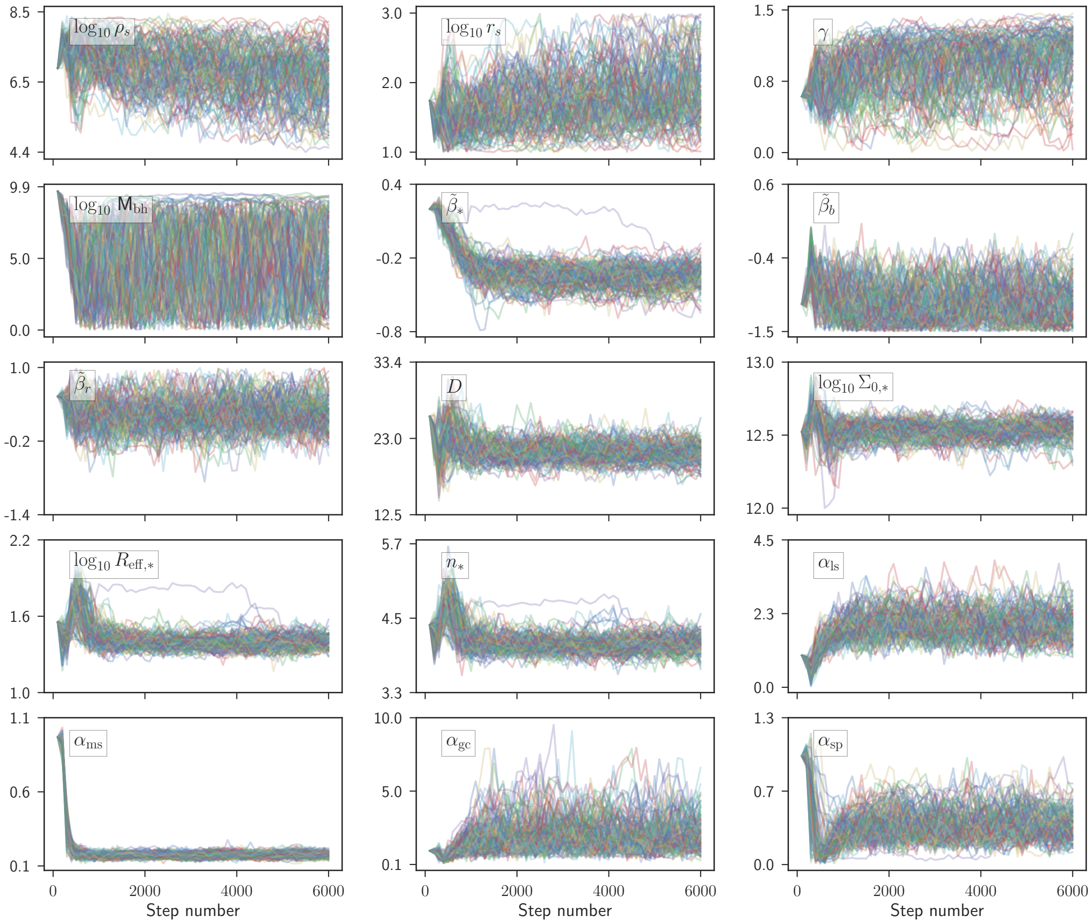

Figure 3.17: Walker traces across each iteration. Units are taken from Table 3.3. ρ_s, r_s, $M_{\rm bh}$, $\Sigma_0, *$, and $R_{{\rm e},*}$ are shown as the logarithm (base 10) of those quantities, and the anisotropy parameters (β) are shown as the symmetrized anisotropy parameter, $\tilde{\beta} = -\log_{10}(1-\beta)$. We reject the first 4500 walker steps in our analysis, where it is clear from the walker traces that the sampler has not yet converged.

3.7.2.1 Wide distance prior

We replaced our informative distance prior with a wide uniform distance prior, $D \sim \mathcal{U}(15Mpc, 30Mpc)$. We recover a lower distance value ($\sim$ 17 Mpc, compared to 21 Mpc with the informative prior). This has the effect of increasing the inner DM slope value, as the lower distance at fixed surface brightness results in a lower luminosity, and hence lower stellar mass and steeper DM density slope.

3.7.2.2 Masked stellar kinematic dataset

We fit all stellar kinematic data, including those masked out as described in Sec. 3.2.3. We find a more concentrated halo and hence a lower value for γ (shown in Fig. 3.21). We also find a slightly worse agreement of the multi-slit data with the model, as quantified by the weight hyperparameter α_{ms}, which changes from 0.13 to 0.10. While there is still work to be done to inference the presence and extent of substructure in stellar kinematic data, we thus find that an imperfect cut is better than no cut at all. However, the open question of whether or not the outer stellar halo of NGC 1407 is in entirely in equilibrium adds $\sim$ 0.2 dex systematic uncertainty to the halo mass measurement and $\sim$ 8 to that of the halo concentration measurement.

3.7.2.3 Varying anisotropy profiles

We performed similar mock data tests to those described in Sec. 3.3.4, but rather than using the constant anisotropy profile, we used a radially varying profile to generate the mock kinematic data. We ran one test where we replaced the stellar kinematic data with one generated using a Mamon & Łokas (2005) profile (shown in Fig. 3.22). This model transitions from isotropic in the center to $\beta = 0.5$ in the outskirts, with the transition radius, r_a. Here we set $r_a = 10$ kpc to be consistent with the value of $r_a = 0.018 r_{\rm vir}$ from theory, e.g., Fig. 2 from Mamon & Łokas (2005). We find a good recovery of the mass parameters, and we find the recovery of the stellar anisotropy to be isotropic to within the uncertainty.

We performed a similar test, but instead of replacing the stellar anisotropy profile, we replaced the red GC anisotropy profile with a Mamon & Łokas (2005) radially varying profile where we set $r_a = 56$ kpc. This value was chosen to lie in the range of $0.018 < r_a/r_{\rm vir} < 0.18$, where the lower bound was shown to be a good match to the stellar orbits from merger remnants and the upper bound was found to be a good match to the DM orbits for collisionless N-body simulations (Mamon & Łokas 2005). As shown in Fig. 3.23, we found a notable difference in the recovered halo parameters, with c_{200} changing from 9 to 25 (and hence a lower value of γ and lower value of M_{200}). Given this difference, we emphasize that our findings are conditional on the adopted anisotropy profile. We defer the in-depth analysis of the GC anisotropy for future work.

3.7.2.4 Non-varying Υ_*

We removed our knowledge of the stellar population constraints for NGC 1407 and instead used a stellar mass model where $M_*(r) = \Upsilon_* L(r)$, using a fixed stellar surface brightness distribution given in Sec. 3.2.1. With this model we found weaker constraints on γ and a slightly higher value of the halo mass. For the mass-to-light ratio we find $\Upsilon_{*,B} = 8.97^{+0.98}_{-1.08} M_{\odot}/L_{\odot,B}$ ($\Upsilon_{*,I} \sim 4 M_{\odot}/L_{\odot,I}$ when adopting the mean $B - I$ color from Spolaor et al. (2008)).

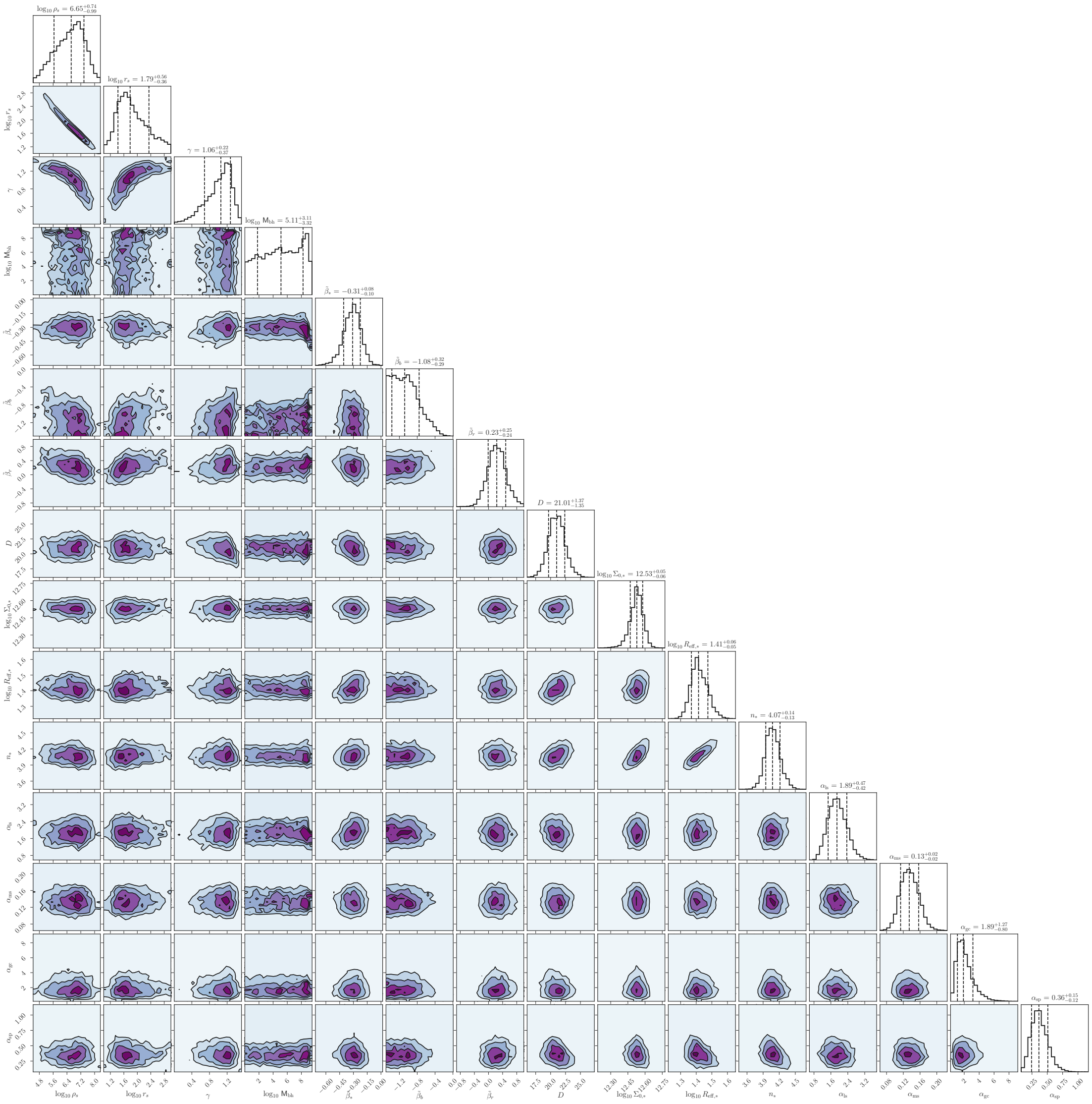

Figure 3.18: Posterior probability distribution for our model. Histograms along the diagonal show the marginalized posterior distributions for the respective parameters. The dashed vertical lines mark the 16th, 50th, and 84th percentiles. The contours (at levels equivalent to 0.5, 1, 1.5 and 2 σ for a 2D Gaussian distribution) show the covariances between these parameters. We hit the prior bounds for M_{bh} and $\tilde{\beta}_b$. For the SMBH, we have very little constraints by design, so we restrict it to be less than 10^{11} $\mathrm{M}_{\odot}$. For all anisotropy parameters, we restrict the range to such that $-1.5 < -\log_{10}(1-\beta)$ to avoid floating-point underflows. However, at such tangential orbital anisotropies, the physical differences in the dynamics are negligible.

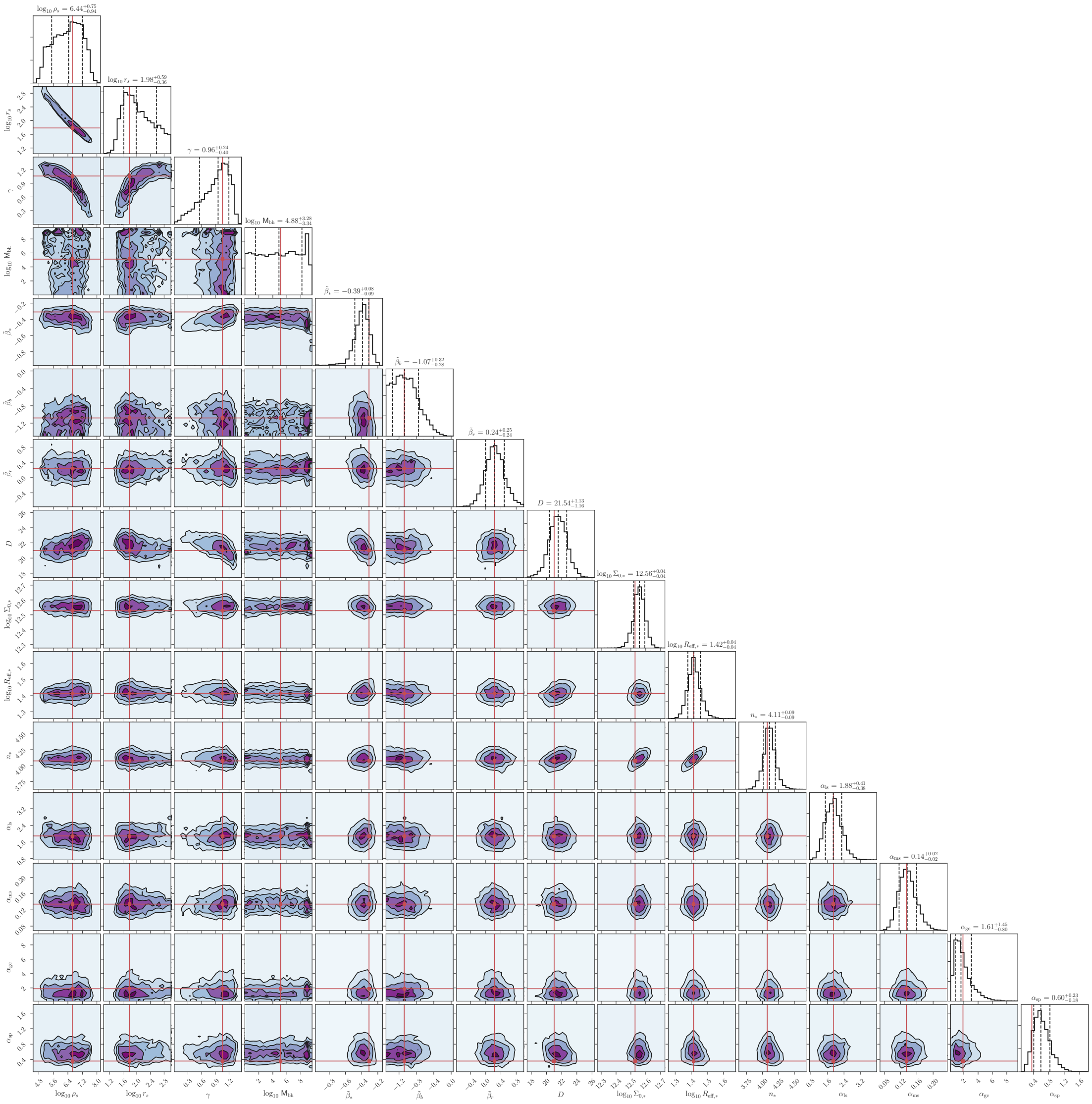

Figure 3.19: Posterior probability distribution for our model applied to the mock data, as discussed in Sec. 3.4.1.

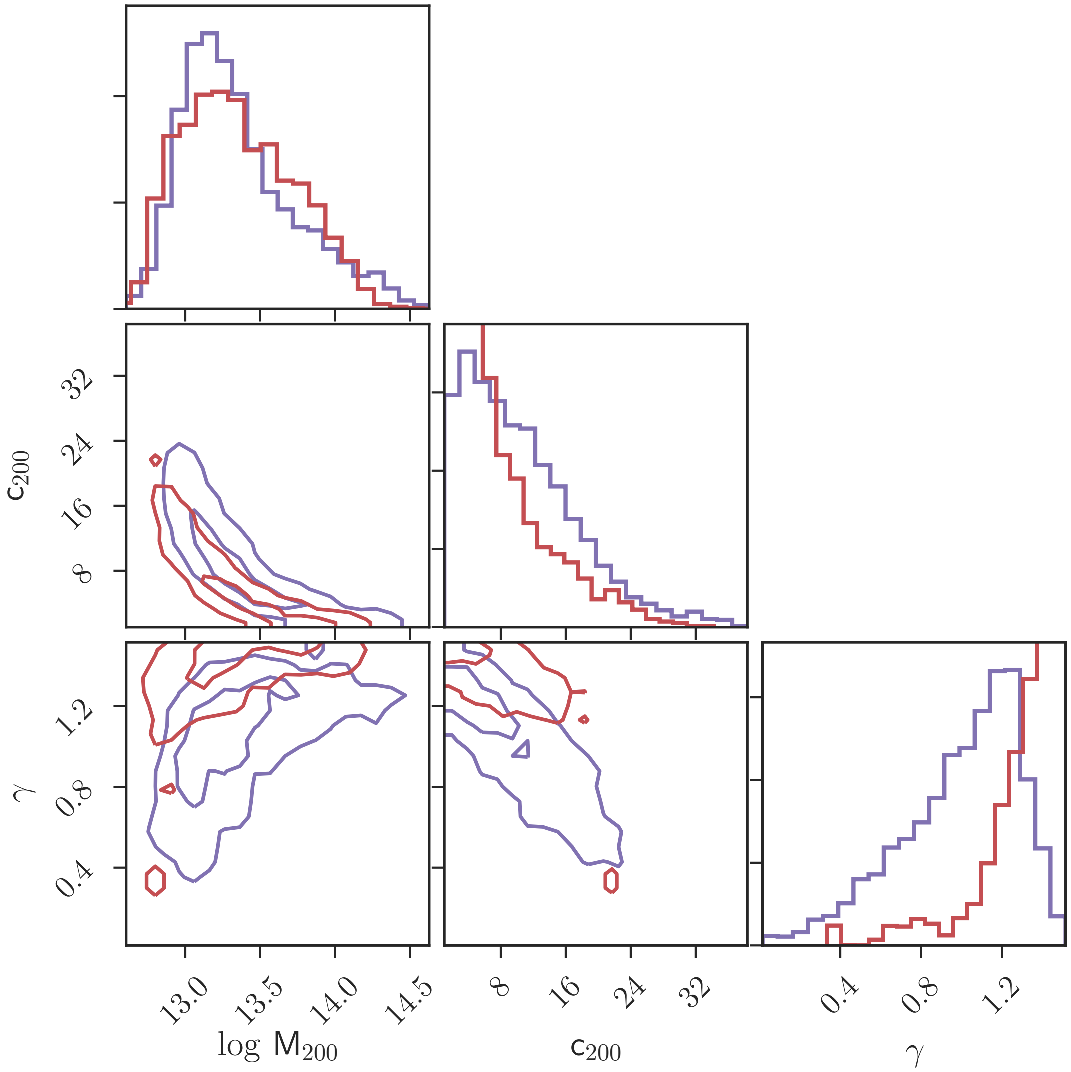

Figure 3.20: Comparison of the posterior probability distributions for the dark matter halo parameters. Purple contours show the reference inference, and the red contours show the inference with a wide uniform prior on the distance, between 15 Mpc and 30 Mpc.

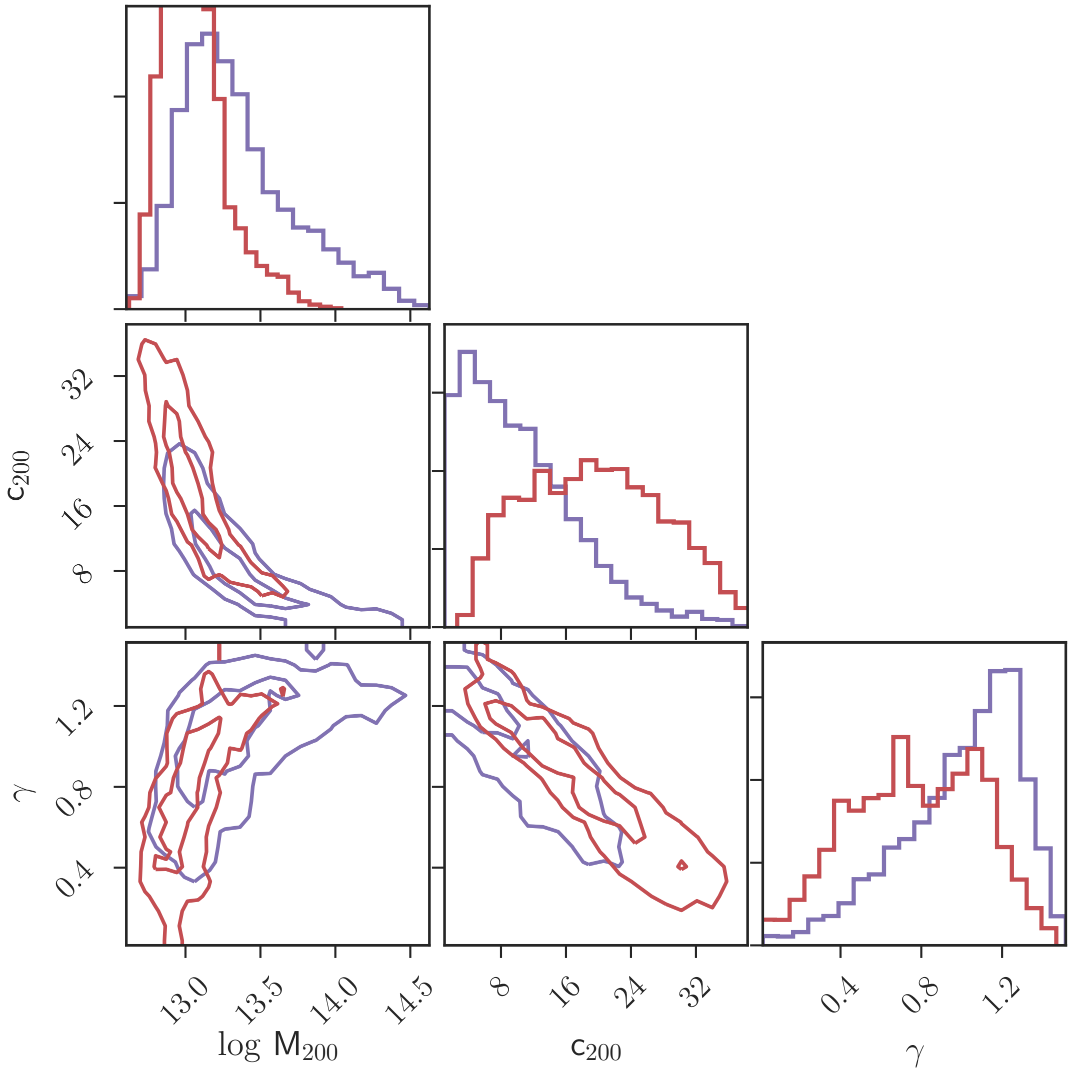

Figure 3.21: Comparison of the posterior probability distributions for the dark matter halo parameters. Purple contours show the reference inference, and the red contours show the inference when we do not mask any of the stellar kinematics data points.

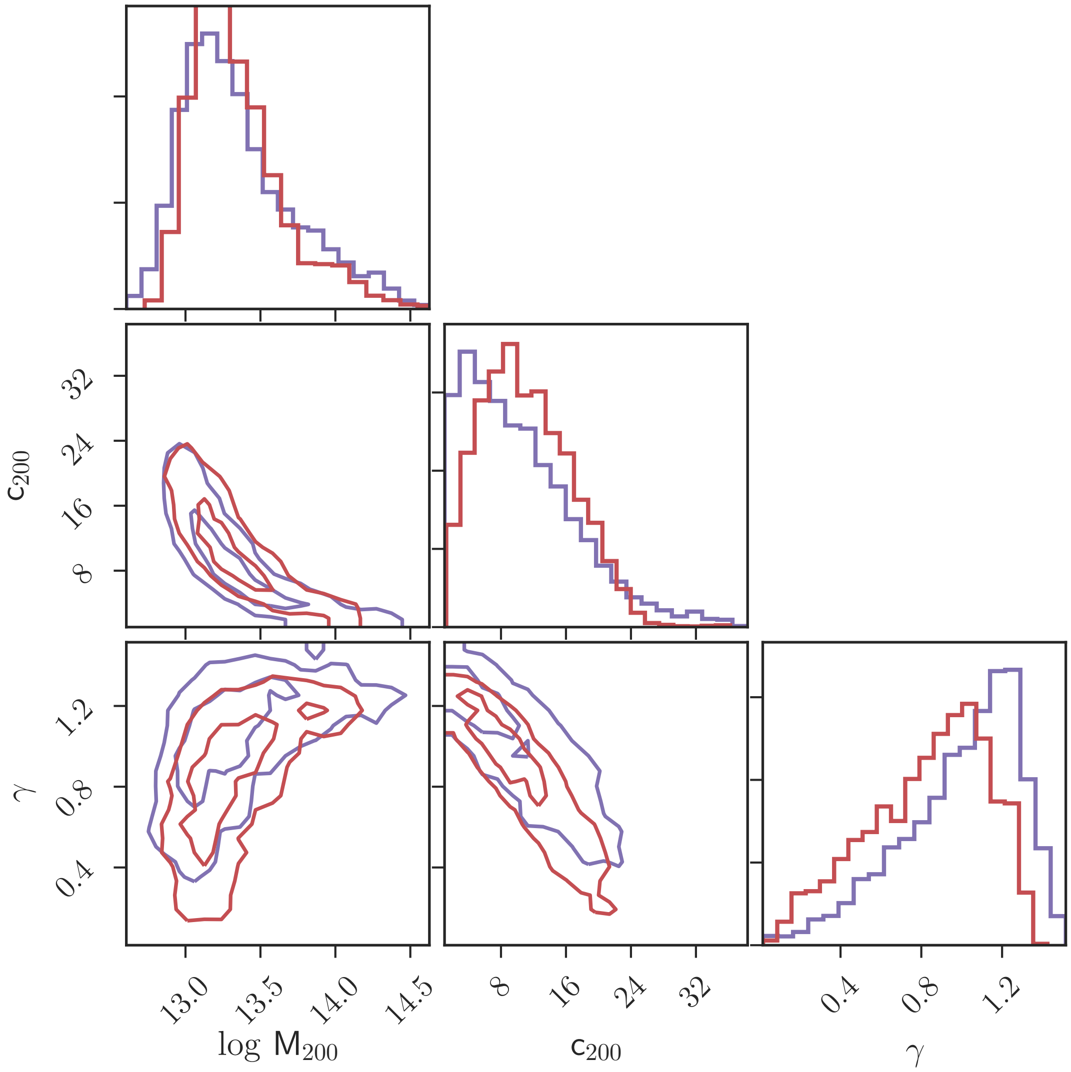

Figure 3.22: Comparison of the posterior probability distributions for the dark matter halo parameters. Purple contours show the reference inference, and the red contours show the recovery of the parameters when the stellar kinematics are generated with a Mamon & Lokas anisotropy profile.

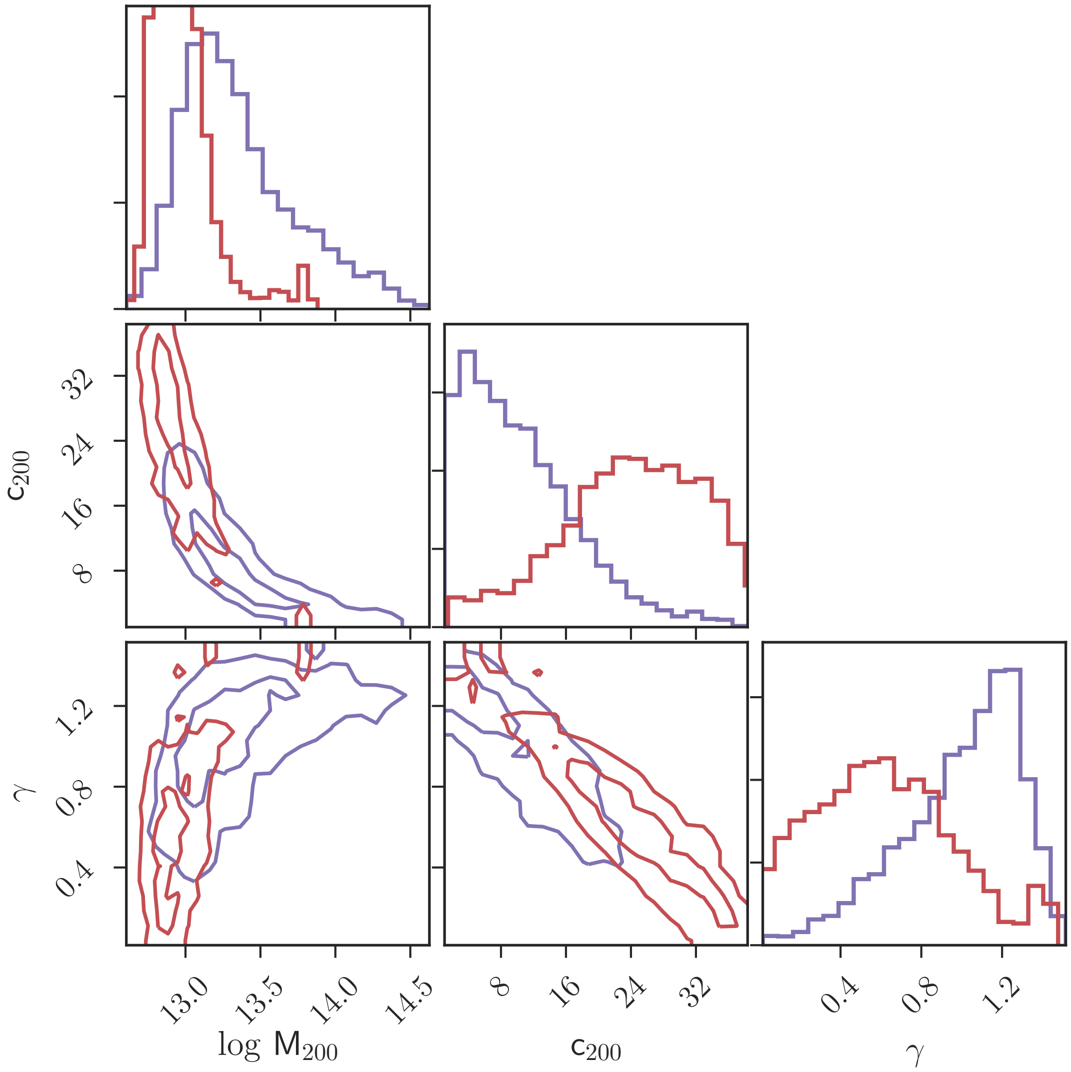

Figure 3.23: Comparison of the posterior probability distributions for the dark matter halo parameters. Purple contours show the reference inference, and the red contours show the recovery of the parameters when the red GC kinematics are generated with a Mamon & Lokas anisotropy profile.

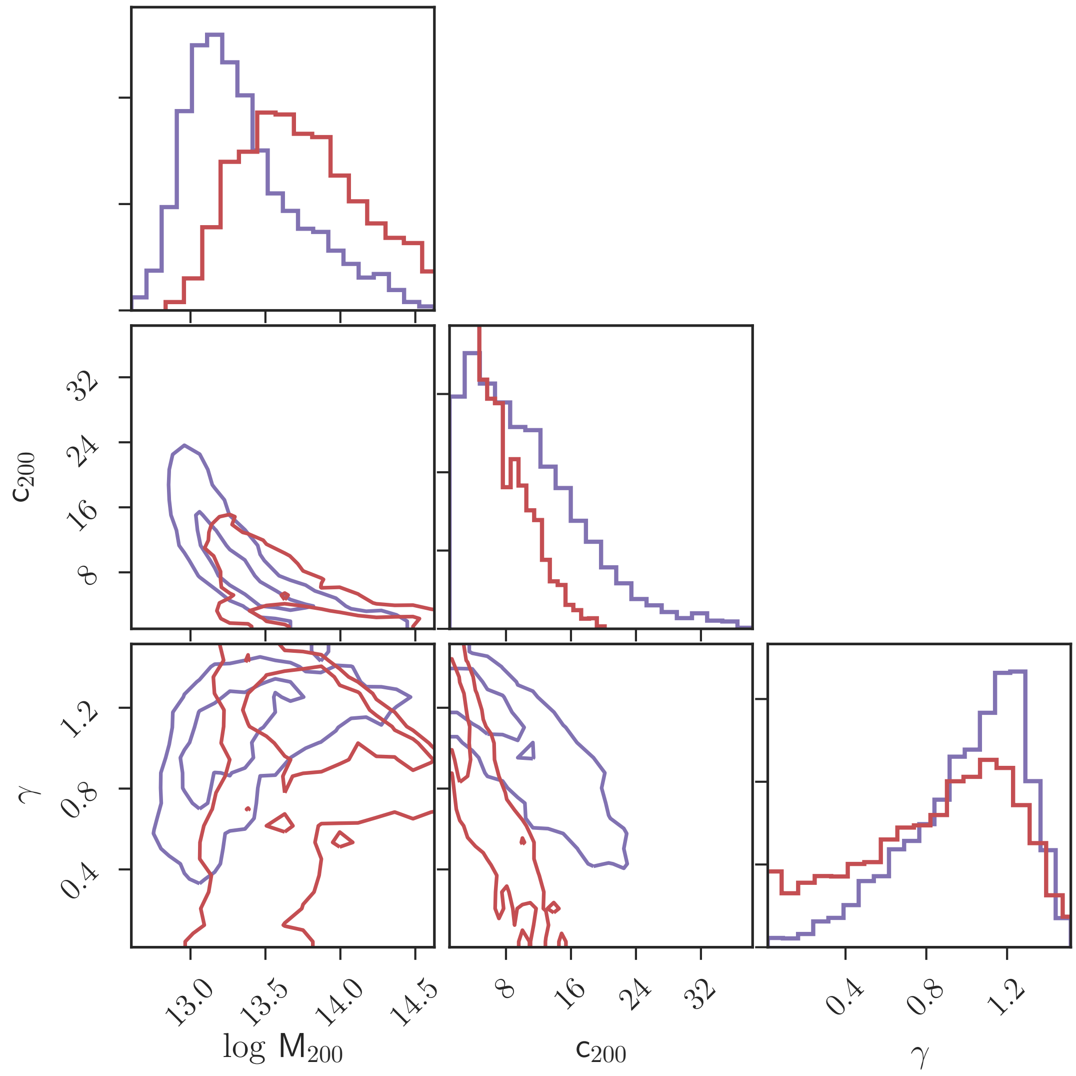

Figure 3.24: Comparison of the posterior probability distributions for the dark matter halo parameters. Purple contours show the reference inference, and the red contours show the inference assuming that the mass-to-light ratio (Υ_*) does not vary with radius.

Chapter 4

Quantifying the deficit of dark matter in NGC 1052-DF2

4.1 Introduction

Ultra-diffuse galaxies (UDGs) were recently recognized as a ubiquitous class of low-surface-brightness stellar systems with luminosities like dwarf galaxies but sizes like giants (van Dokkum et al. 2015; Yagi et al. 2016). They are found in all environments from clusters and groups to the field (e.g., Martínez-Delgado et al. 2016; van der Burg et al. 2017), and appear to originate from multiple formation channels, including an extension of normal dwarfs to lower surface brightness, as tidal debris, and perhaps as "failed" galaxies (e.g., Peng & Lim 2016; Greco et al. 2018; Pandya et al. 2018).

The failed-galaxy scenario was motivated partly by inferences of UDG halo masses based on dynamics and on number-counts of globular star-clusters – masses that in some cases appear significantly higher than for the overall dwarf-galaxy population (Beasley et al. 2016; van Dokkum et al. 2016, 2017a; Amorisco et al. 2018; Lim et al. 2018). The implication is that the stellar-to-halo mass relation (SHMR; e.g., Moster et al. 2013; Rodríguez-Puebla et al. 2017) for luminous dwarf galaxies ($L \sim 10^8 L_\odot$) may have a much larger scatter than was presumed, requiring revisions in galaxy formation models at halo masses of $\sim 10^{11} M_\odot$ (see also Smercina et al. 2018).

In this context, one of the nearest known UDGs, NGC 1052-DF2 in a galaxy group at $\sim$ 20 Mpc (Fosbury et al. 1978, Karachentsev et al. 2000; van Dokkum et al. 2018b (hereafter vD+18a)), presents a valuable opportunity for detailed dynamical study. vD+18a used deep Keck spectroscopy to measure radial velocities for 10 luminous star-clusters around DF2, estimating its dynamical mass within a radius of $\sim$ 8 kpc (cf. Virgo-UDGs work by Beasley et al. 2016; Toloba et al. 2018). The result was very surprising: rather than an unusually *high* mass-to-light ratio (M/L) as found for previous UDGs, the M/L was unusually *low*, and consistent with harboring no dark matter (DM) at all.

The low/no-DM result generated spirited debate, much of which focused on how best to estimate the intrinsic velocity dispersion σ of DF2 (e.g., Martin et al. 2018; Laporte et al. 2019; van Dokkum et al. 2018c).

However, the more fundamental question is what range of halo mass profiles is permitted by the data, which we examine in detail in this Letter. We adopt a generative modeling approach where the individual velocity measurements are mapped statistically onto halo parameter space, without the intervening steps of estimating σ and applying a mass estimator. In addition to deriving constraints on the dynamical mass profile, we consider the potential impact of tidal stripping, and furthermore compare DF2 with Local Group dwarfs.

4.2 Observational Constraints

NGC 1052-DF2 has position, redshift, surface brightness fluctuation (SBF), and tip of the red giant branch measurements all consistent with being a satellite of the giant elliptical galaxy NGC 1052 (vD+18a; van Dokkum et al. 2018a). We adopt a distance of 19 Mpc, matching the measured SBF distance to DF2 (Cohen et al. 2018), while allowing for a ±1 Mpc uncertainty in our analysis[1].

The UDG surface brightness follows a Sérsic profile with index $n = 0.6$, effective radius $R_{\rm e} = 22.6''$ (2.08 kpc), and total luminosity of $1.2 \times 10^8\ L_{V,\odot}$. For the stellar M/L, we adopt a Gaussian prior with mean of $\Upsilon_{*,V} = 1.7$ in Solar units and standard deviation of 0.5 (based on stellar population modeling; van Dokkum et al. 2018d). We truncate this distribution to be between 0.1 and 10.

NGC 1052-DF2 has ten star-clusters with radial velocity measurements in vD+18a. We use one updated velocity from van Dokkum et al. (2018c); this has only a mild impact on the results. Although the mass uncertainties from using so few tracers is relatively large (as we will find here), there is ample precedent in the literature for drawing meaningful conclusions from small sample sizes (Aaronson 1983; Kleyna et al.

---

[1] A distance of 13 Mpc has been proposed (Trujillo et al. 2019), but see van Dokkum et al. (2018a) for an in-depth discussion of the evidence for the greater distance.

2005; Chapman et al. 2005; Brown et al. 2007; Koposov et al. 2015).

The surface-density distribution of the star-cluster population is highly unconstrained. We assume an exponential distribution of tracers (i.e., a Sérsic profile with $n = 1$) where the half-number radius is drawn from a Gaussian prior with a mean of the observed half-number radius ($32''$) and standard deviation of $10''$. We truncate this distribution to be between $10''$ and $70''$. Our adopted mean half-number radius is 40% larger than R_e of the galaxy diffuse starlight, consistent with studies of the star-cluster systems of other UDGs (Peng & Lim 2016; van Dokkum et al. 2017a; Toloba et al. 2018; cf. Forbes 2017).

4.3 Jeans Modeling Methods

We use the Bayesian Jeans modeling formalism of Wasserman et al. (2018b) to infer the mass distribution of DF2. Here a given mass profile and a tracer density profile are linked to a predicted line-of-sight velocity dispersion profile $\sigma_\mathrm{J}(R)$. The assumptions include spherical symmetry, dynamical equilibrium, and velocity-dispersion anisotropy ($\beta = 1 - \sigma_t^2/\sigma_r^2$) that is constant with galactocentric radius. (There is no evidence for rotation in the system, although individual velocity uncertainties are too large for strong constraints; vD+18a). We adopt a Gaussian prior on $\tilde{\beta} = -\log_{10}(1-\beta)$ with a mean of 0 (isotropic) and standard deviation of 0.5 (truncated to the range of $\tilde{\beta} = -1$ to $+1$).

Since we do not directly constrain the dynamical mass beyond ~ 8 kpc, we must rely on priors on the halo characteristics – on the DM profile shape, and also on expected correlations between halo mass, concentration, and stellar mass.

We model the mass distribution as the sum of the stellar mass, with spatial distribution described in Section 4.2, and a DM halo. For the halo density distribution we use the generalized Navarro–Frenk–White (gNFW) profile,

$$\rho(r) = \rho_s \left(\frac{r}{r_s}\right)^{-\gamma} \left(1 + \frac{r}{r_s}\right)^{\gamma-3} \tag{4.1}$$

where r_s is the scale radius, ρ_s is the scale density, and γ quantifies the inner log-slope. For $\gamma = 1$, this matches the usual NFW halo model (Navarro et al. 1997), but letting γ vary below 1 allows for models which have a cored, shallower density profile.

We re-parameterize the halo in terms of virial mass (M_{200c}) and concentration (c_{200c}), where

$$M_{\mathrm{200c}} = 200\rho_{\mathrm{crit}}\frac{4\pi r_{\mathrm{200c}}^3}{3} \tag{4.2}$$

and $c_{\mathrm{200c}} = r_{\mathrm{200c}}/r_s$.

We then consider two flavors of mass models: one in which the stellar and halo masses are drawn from a SHMR, and one where the stellar and dark masses are decoupled. For the latter model, we use a uniform prior on $\log_{10} M_{\mathrm{200c}}/M_\odot$ between 2 and 15. This effectively allows for the case of no DM, since the stellar mass is $\log_{10} M_\star/M_\odot \sim 8.3$.

For both types of models we assume that the halo concentration is drawn from a mass–concentration relation (MCR; Diemer & Kravtsov 2015; Diemer 2018) based on the *Planck 2015* cosmology. We use a log-normal distribution about this expected concentration with a scatter of 0.16 dex.

For the SHMR we use the $z = 0$ relation of Rodríguez-Puebla et al. (2017), where halos with mass $M_{200c} \sim 10^{10.8} M_{\odot}$ host galaxies with M_* similar to DF2 (note that for a satellite galaxy such as DF2, the halo mass is pre-infall, before tidal stripping). We allow for variation around this mean relation through a variable scatter:

$$\sigma_{\log M_*} = 0.2 - 0.26(\log M_{\rm vir} - \log M_1) \tag{4.3}$$

below virial masses of $M_1 = 10^{11.5}\ M_{\odot}$ (note $M_{\rm vir} \neq M_{200c}$; at M_1, $M_{200c} \sim 0.9 M_{\rm vir}$), while at higher masses, $\sigma_{\log M_*}$ is a constant 0.2 dex scatter (Garrison-Kimmel et al. 2017; Munshi et al. 2017).

Given the wide range of possible baryonic effects on the inner slope of DM halos (Oh et al. 2011; Adams et al. 2014; Pineda et al. 2017), we adopt a uniform prior on γ between 0 and 2.

To connect the Jeans model predictions for $\sigma_{\rm J}$ to the velocity observations, we use a Gaussian likelihood for the probability of drawing data, v_i, given the location R_i and the various model parameters θ,

$$\begin{aligned} \mathcal{L}(v_i|R,\theta) &= \mathcal{N}\left(v_i - v_{\rm sys},\ \sigma^2 = \sigma_{\rm J}^2(R|\theta) + \delta v_i^2\right) \qquad (4.4) \\ &= \left(2\pi\sigma^2\right)^{-1/2} \exp\left(-\frac{(v_i - v_{\rm sys})^2}{\sigma^2}\right) \end{aligned}$$

where $v_{\rm sys}$ is the systemic velocity (drawn from a Gaussian prior with a mean of the observed velocities, 1801.6 km s^{-1}, and with a 5 km s^{-1} standard deviation), and δv_i is the measurement uncertainty.

We draw from our posterior with the *emcee* Markov Chain Monte Carlo (MCMC) ensemble sampler (Foreman-Mackey et al. 2013). We run our sampler with

128 walkers for 2000 iterations, rejecting the first 1500 to ensure fully-mixed chains. The posterior distributions of $v_{\rm sys}$, Υ_*, and distance closely match those of the associated prior distributions. For the inference with the SHMR-informed prior, the posterior distribution of the star-cluster system $R_{\rm e}$ is slightly lower (with median of $26''$). The weak-prior model prefers a slightly tangential orbital anisotropy, although consistent with isotropy, while the posterior anisotropy in the SHMR-prior model matches the prior.

4.4 Halo Mass Inferences

Before discussing the best-fitting results, in Figure 4.1 we present a comparison between the data and a simple model with a cuspy NFW halo that follows the mean SHMR, assuming isotropic orbits. The individual star-cluster velocity measurements (absolute value relative to $v_{\rm sys}$) versus galactocentric radius are shown along with a model line-of-sight σ profile (dashed-green curve). It is clear that this is not a favorable model: ~ 3 of the observed velocities should lie above the curve, which has a spatially-averaged $\sigma \sim 36$ km s^{-1}, compared to an observed $\sigma \sim 5$–10 km s^{-1}.

This is not however the only plausible model, as there is scatter in the predicted SHMR and in the halo concentration. Furthermore, UDGs and luminous dwarfs in general are expected to inhabit cored DM halos (Chan et al. 2015; Di Cintio et al. 2017a). Allowing for a DM core (dot-dashed purple curve) reduces the tension with the data somewhat ($\sigma \sim 22$ km s^{-1}). Introducing scatter in the SHMR and the MCR as discussed

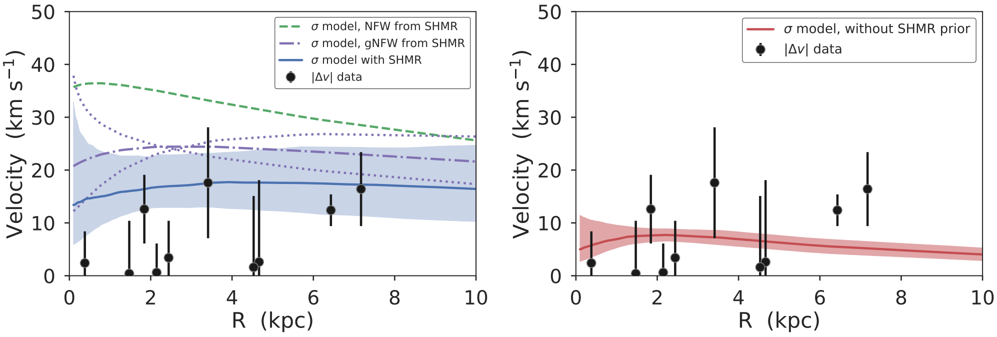

(a)

(b)

Figure 4.1: DF2 observed star-cluster velocity offsets (points with error-bars), compared with the posterior predictive distribution of the velocity dispersion profiles associated with the star+halo model fit with freely-varying anisotropy and R_e. The shaded regions give the inner 68% of samples. *Left:* The dashed green curve shows an isotropic model with a standard DM halo ($\gamma = 1$ cusp) and halo mass fixed to the SHMR mean. The dot-dashed purple curve is for a cored DM halo ($\gamma = 0.2$), with fixed halo mass, and isotropic orbits. The dotted purple lines around this curve show the effect of assuming radial (falling profile) and tangential (rising profile) anisotropy. The blue solid curve shows a cored halo with mass informed by a log-normal prior about a standard SHMR. *Right:* The red solid curve shows the model fit with the relaxed prior on halo mass – a model that we see is less in tension with the data than the models with large amounts of DM (left panel).

in Section 4.3, we present the best "standard" model from our MCMC fitting, including a freely varying orbital anisotropy, as a solid-blue curve with uncertainty envelope in Figure 4.1. This model dispersion profile is fairly constant with spatially-averaged $\sigma = 17^{+6}_{-4}$ km s^{-1} and appears more reasonably close to the data, although still in tension with the many observed near-zero relative velocities. The posteriors on some key model parameters are: $\beta = 0.0^{+0.7}_{-2.5}$, $\log_{10} M_{200\mathrm{c}}/M_\odot = 10.7^{+0.2}_{-0.3}$, $c_{200\mathrm{c}} = 9^{+4}_{-3}$ (implying $r_s = 8^{+4}_{-3}$ kpc), and $\gamma = 0.2^{+0.3}_{-0.2}$, although we note that the samples of γ hit the prior boundary at 0. This is a model solution with a normal halo and concentration (consistent with the priors: see Figure 4.2, *left*) but a large central density core – strongly disfavoring the NFW model.

We next consider a model that allows for deviation from the standard SHMR, along with a free central DM slope, while still imposing the standard prior on halo mass versus concentration. We find that the DM halo all but disappears, with $M_{200\mathrm{c}} < 1.2 \times 10^8\ M_\odot$ ($M_{\mathrm{DM}}/M_* < 0.6$) at the 90$^{\mathrm{th}}$ percentile. The posterior velocity dispersion profile is shown in Figure 4.1 (right), with an average $\sigma = 7 \pm 1$ km s^{-1}. This model prefers a more tangential $\beta = -1.0^{+1.2}_{-2.7}$.

For a measure of relative predictive accuracy of these two models, we use the Watanabe–Akaike Information Criterion (WAIC), an approximation of cross-validation (Gelman et al. 2013), defined as

$$\mathrm{WAIC} = -2\sum_{i}^{n} \ln \int \mathcal{L}(v_i \mid \theta) p_{\mathrm{post}}(\theta)\, \mathrm{d}\theta + 4\sum_{i}^{n} \mathrm{var}_{\mathrm{post}} \left[\ln \mathcal{L}(v_i \mid \theta)\right] \tag{4.5}$$

where $p_{\mathrm{post}}(\theta)$ is the posterior distribution, $\mathcal{L}(v_i|\theta)$ is the likelihood, and $\mathrm{var}_{\mathrm{post}}$ is the variance over the posterior. The first term measures the predictive accuracy marginalized over the posterior distribution, while the second term penalizes for model complexity by computing an approximation of the effective number of model parameters (analogous to reduced χ^2). We find ΔWAIC $= 1.5$ (equivalent to a model odds ratio of ~ 2), slightly favoring the model without the SHMR prior, although not enough to reject the SHMR model outright.

As a summary of these results, Figure 4.2 shows the distribution of stellar and dark mass within a three-dimensional aperture of 10 kpc, as well as the halo concentration for these two models. For the SHMR-prior model, the data prefer a lower enclosed dark mass than in the prior, with a shift in the median $M_{\rm DM}$ within 10 kpc from $1.2\times10^{10}\ M_\odot$ to $5.1\times10^{9}\ M_\odot$. For the weak-priors model, the posterior distribution of $M_{\rm DM}(< 10\,{\rm kpc})$ extends all the way to the lower prior boundary ($\sim 10^2\ M_\odot$), with a 90th-percentile upper bound of $1.2 \times 10^8\ M_\odot$. Thus the data prefer a relatively low amount of DM within the region probed.

The more tightly constrained quantity of interest is the *total* dynamical mass within 10 kpc, which is $(2.2^{+0.9}_{-0.6}) \times 10^8 M_\odot$, or dynamical $M/L_V = 1.7^{+0.7}_{-0.5}$. The latter value is remarkably coincident with the independent stellar population estimate for DF2 (Section 4.2). We conclude that data-driven dynamical modeling of DF2 allows for at most an extremely low-mass DM halo, and suggests that this UDG is comprised purely of stars.

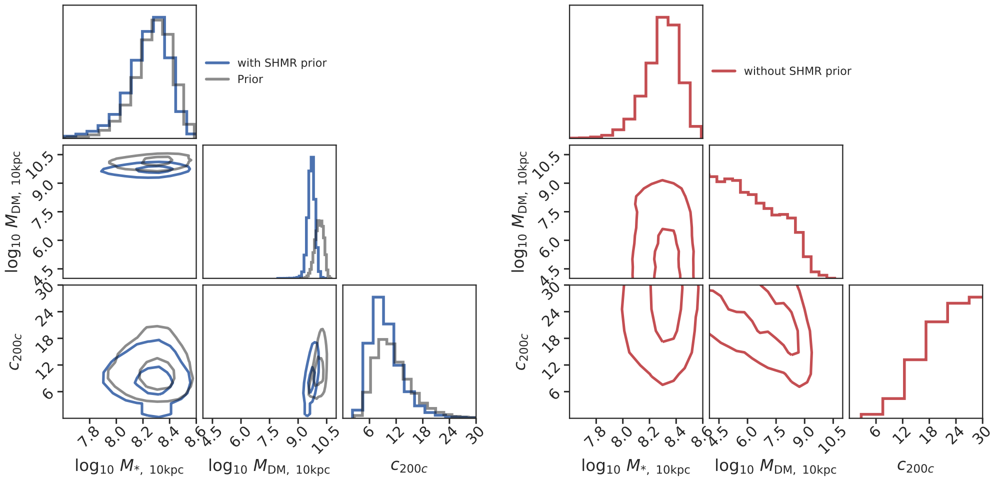

(a) (b)

Figure 4.2: Distributions of select model parameters. The contours showing the covariance between the two parameters are placed at 1- and 2-σ intervals. Masses are in $M_\odot$. *Left:* For the model with the SHMR prior (in blue). The prior distribution is shown in gray. From left to right, the parameters are the stellar mass within 10 kpc, the DM mass within 10 kpc, and the halo concentration. *Right:* The same model parameters but for the model without the SHMR prior. We see that the SHMR prior model largely recovers the prior distribution, though with slightly lower halo mass, while the data-driven model has a halo mass that hits the prior lower-boundary.

4.5 Tidal Effects

The models considered in the previous sections were for an isolated dwarf and neglected any influence from the nearby massive elliptical galaxy, NGC 1052. In particular, infall of a satellite into a larger host initiates a process of tidal stripping, first from the outer DM halo, then from the central regions, followed by total disruption. Tidal stripping and heating has been proposed as the dominant mechanism for forming UDGs, which could be considered as exemplars for galaxies undergoing tidal disruption (Carleton et al. 2019). Some previously studied UDGs are clearly in the process of disruption (Merritt et al. 2016), while many others have undisturbed morphologies out to $\sim 4\ R_\mathrm{e}$ (Mowla et al. 2017).

vD+18a presented analysis of tidal stripping to constrain the physical separation between DF2 and NGC 1052. Here our aim is to develop a holistic model where the inferred UDG mass distribution is checked for consistency with tidal constraints, propagating uncertainties on viewing angle, satellite mass distribution, and central galaxy mass. In particular, is a no-DM scenario implausible owing to a likelihood of disruption?

We use a simple model for the tidal radius given enclosed masses of satellite and central galaxies:

$$r_\mathrm{tidal} = \left(\frac{M_\mathrm{sat}(r_\mathrm{tidal})}{(\alpha - \gamma_M) M_\mathrm{cen}(d)} \right)^{1/3} d, \tag{4.6}$$

where d is the 3D distance between the two galaxies, γ_M is the local log-slope of the enclosed mass profile of the central galaxy at d, and $\alpha = 2$ if we assume the orbit of the satellite is radial and 3 if we assume the orbit is circular (van den Bosch et al.

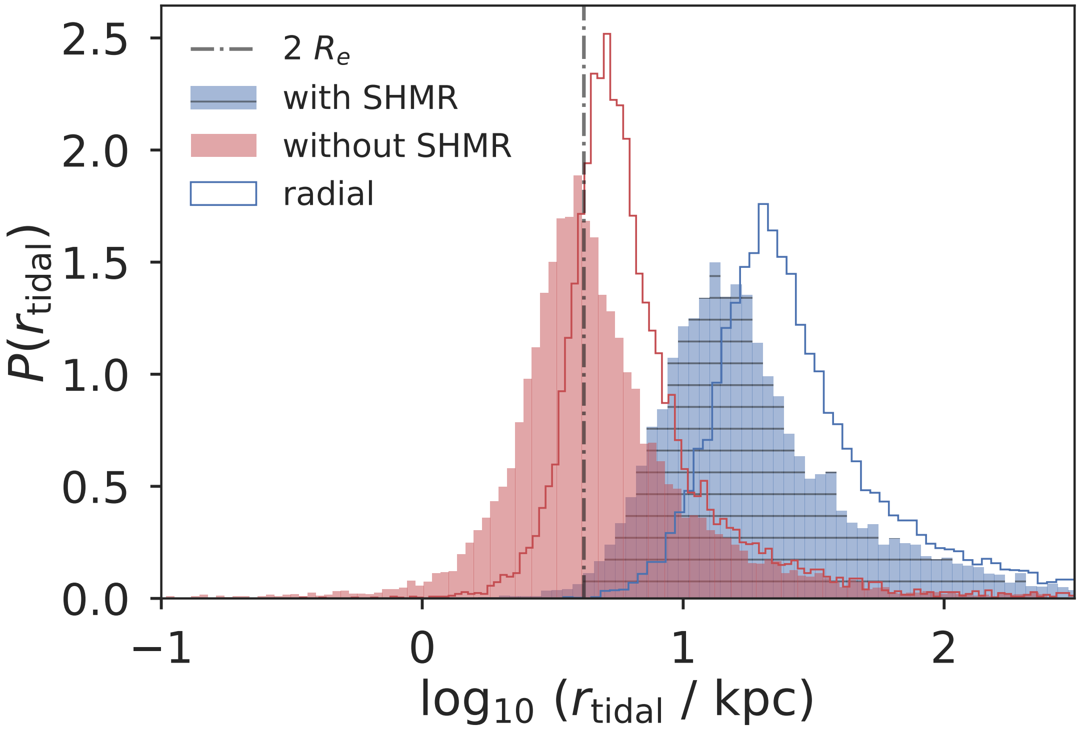

Figure 4.3: The distribution of DF2 tidal radii inferred for each of the two models. The blue histograms show the limits inferred with a strong SHMR prior, while the red histograms show those for the model without the SHMR prior. The filled histograms show the tidal radius from assuming a circular orbit, while the empty histograms show the same distributions from assuming a radial orbit. The vertical dash-dotted line shows 2 $R_{\rm e}$ for the starlight. We see that 52% (81%) of the no-SHMR-prior model samples for the circular (radial) orbit are above this lower bound, thus allowing for little/no-DM solutions that do not exhibit tidal disturbances.

2018). Without modeling any constraints on the actual orbit of DF2, we compare results assuming either radial or circular orbits for the satellite, assuming that the truth lies somewhere in between these two cases. For our sampled central mass profiles and separation distances, $\gamma_M \sim 1$. DF2 shows no obvious evidence of tidal disturbances, with regular isophotes out to $\approx 2R_\mathrm{e}$ (~ 4 kpc; vD+18a). This provides a tidal constraint that $r_\mathrm{tidal} \gtrsim 4$ kpc.

To estimate the central-galaxy mass, we use the halo-to-stellar mass relation from Rodríguez-Puebla et al. (2017). For $M_* = 10^{11} M_\odot$ (Forbes 2017), we expect $M_\mathrm{200c} = 4.9 \times 10^{12} M_\odot$ with a scatter of 0.25 dex (from inverting the SHMR scatter of 0.15 dex). We then adopt an NFW profile with concentration from the MCR and calculate the enclosed mass at a given radius.

To fold in all the uncertainties together (central mass, satellite mass posterior from the previous inference, and distance), we randomly sample from the underlying parameters, including a uniform distribution of projection angles. We plot the resulting distribution of tidal radii in Figure 4.3.

For the data-driven model, $r_\mathrm{tidal} = 4.3^{+4.7}_{-1.7}$ $(5.7^{+5.09}_{-1.71})$ kpc when assuming a circular (radial) orbit. Thus there is a large fraction of model-posterior space (52% for circular, 81% for radial) where DF2 can have little/no DM yet be tidally undisturbed out to 4 kpc. We note that the low-velocity star clusters observed out to ~ 7.5 kpc could still be bound even with $r_\mathrm{tidal} \sim 4$ kpc, if they have retrograde orbits (Read et al. 2006).

Turning to the SHMR-prior model, the dwarf would be naturally much more resistant to tides, and the tidal radius would be farther out (Figure 4.3). However, the predicted value of $r_{\rm tidal} = 16^{+28}_{-7}$ kpc (or 24^{+33}_{-10} kpc for the radial case) implies that DF2 would still likely have most of its DM stripped away by now, as $M_{\rm DM}(r_{\rm tidal})/M_{\rm 200c} \sim 0.2$ (~ 0.4).

The latter point leads us to the possibility that DF2 started out with a normal DM halo, but has been tidally eroded, not only by removing the outer parts but also by stripping out much of the central DM prior to disruption of the visible galaxy. Such a solution was studied through N-body simulations by Ogiya (2018), who found that the final dark mass within 10 kpc could be $\sim 10^8 M_\odot$ – which is consistent with our observations (see red curves in Figure 4.2). We note however two major caveats to this interpretation: (1) there is a small range of orbital parameter space that allows for the necessary degree of stripping; (2) the dynamical time within the UDG is comparable to its orbital period, which may prevent it from relaxing into a visually undisturbed system with cold kinematics.

The difference in predicted tidal radii between the DM and no-DM models motivates looking beyond 4 kpc for tidal features around DF2 to help distinguish between these two scenarios.

4.6 DF2 in a Wider Context

We have found through Jeans modeling that the observations of cold kinematics in DF2 imply a very low DM content. However, Martin et al. (2018) disputed the unusual nature of this galaxy by noting its similar σ and dynamical M/L to previously studied dwarfs. Here we emphasize that such comparisons neglect the different measurement radii used, and we clarify the position of DF2 in a wider context by constructing a plot relating galaxy stellar masses, halo masses, and sizes (Fig. 4.4).

We take the compilation of Local Group (LG) dwarf galaxies from Fattahi et al. (2018), selecting only galaxies with $M_* > 10^5\ M_\odot$ and updating with sizes from Martin et al. (2016) where available. Taking the dynamical mass within $r_{1/2} \approx 1.3R_\mathrm{e}$ and subtracting the associated stellar mass, we compute the DM contribution to the circular velocity,

$$v_\mathrm{circ,DM} = \sqrt{\frac{GM_\mathrm{DM}(< r_{1/2})}{r_{1/2}}}\ , \tag{4.7}$$

propagating uncertainties in the distance, size, luminosity, stellar M/L, and velocity dispersion. We color these points in Figure 4.4 by their stellar mass, with different symbols for field dwarfs versus satellites. We compare these measurements with halo circular velocity profiles for several halo masses, adopting MCR concentrations and $\gamma = 0.3$ cores, while color-coding these profiles by the SHMR-predicted stellar mass. The halo-concentration scatter is illustrated by the red band for the $10^{11}\ M_\odot$ halo.

This Figure shows that some dwarfs track cored-halo profiles appropriate to their stellar masses. Others have higher velocities and perhaps cuspy halos (e.g., Spekkens et al. 2005; Oñorbe et al. 2015; Genina et al. 2018). A few have low velocities; since most of these are satellites, they may be examples of ongoing tidal stripping that has depleted their central DM content (Collins et al. 2013; Fattahi et al. 2018; Buck et al. 2019). DF2, however, stands out from all these galaxies by having the lowest DM-velocity estimate, despite the much larger measurement radius. Andromeda XIX is closest in σ–$r_{1/2}$ space

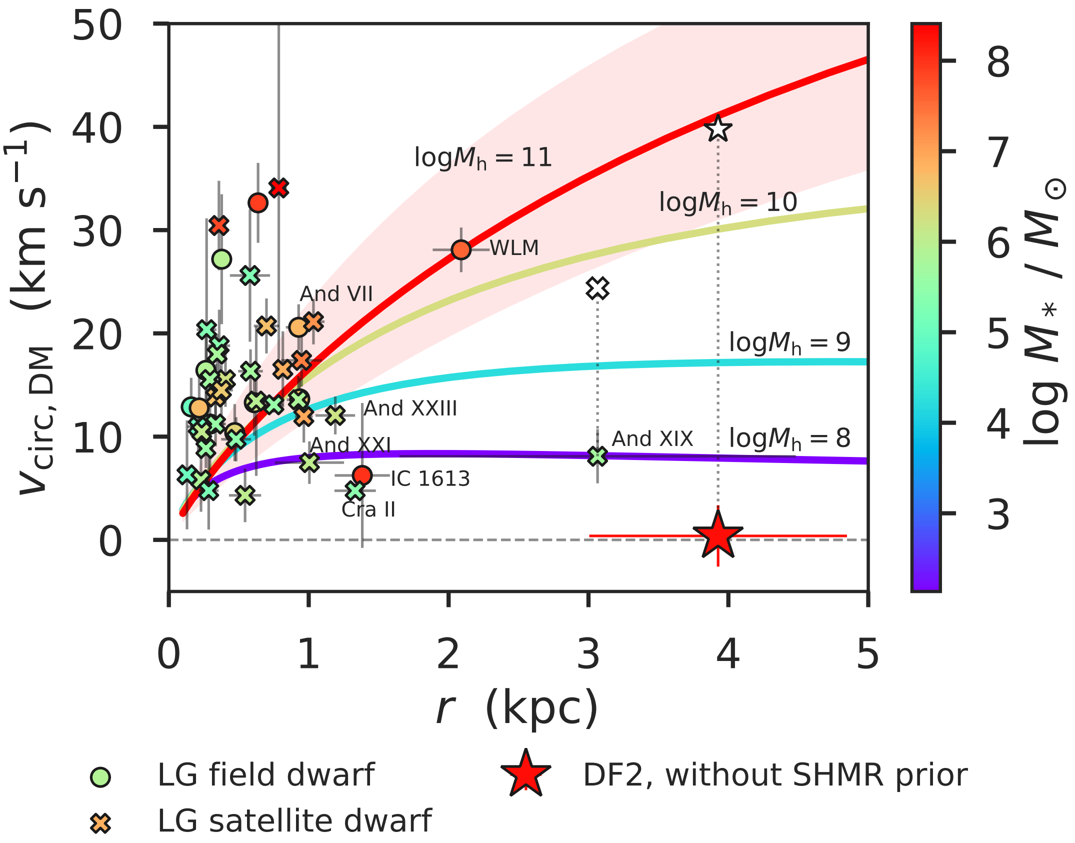

Figure 4.4: DF2 compared with Local Group dwarf galaxies. The circles and x's show the circular velocity of the DM component for field and satellite dwarfs respectively. The points are color-coded by stellar mass. The curves show cored ($\gamma = 0.3$) NFW profiles for different halo masses (in $M_\odot$), color-coded by the mean expected stellar mass. The posterior predictive value for the data-driven DF2 inference is shown as the star, below $\log M_{200c}/M_\odot = 8$. The open markers with dotted lines for And XIX and DF2 show the expected DM halos they would occupy given their stellar mass. We see that DF2 is an outlier even beyond the extended LG dwarfs in both its size and in mismatch between expected and observed DM halo mass.

but has $\sim 300\times$ lower stellar mass and thus does not appear as DM-depleted as DF2. IC 1613 has a high stellar mass but the smaller measurement radius allows for a larger range of halo masses.

We therefore strengthen the conclusion of vD+18a that DF2 is an extreme outlier in the usual dwarf–DM scaling relations. There are then two main possible explanations. One is that the galaxy formed with little or no DM, and the other is that it has been severely stripped of DM. We cannot definitively discriminate between the two scenarios, but in Section 4.5 we pointed out potentially major flaws in the tidal argument. Furthermore, there is an additional clue that has so far been generally overlooked: the very star-cluster system used to probe the dynamics of DF2 is itself so far unique in the known Universe. The clusters are on average far more luminous than in other galaxies including the Milky Way, and they are also unusually extended and elongated (vD+18a). The presence of either a normal or a stripped DM halo provides no explanation for this novel observation. On the other hand, if DF2 formed through a rare pathway without DM (e.g., scenarios discussed in vD+18a), then it is more plausible that its star-cluster system would show unusual properties as well.

The peculiar case of DF2 demonstrates the rich yield of information that can be obtained through detailed observations of dwarfs beyond the Local Group, which will help challenge and refine our understanding of galaxy formation and of the nature of DM.

Chapter 5

Constraints on fuzzy dark matter from the ultra-diffuse galaxy Dragonfly 44

5.1 Introduction

The concordant cosmological model of dark energy plus cold dark matter (ΛCDM) has had remarkable successes in describing the large scale structure of the universe (e.g., Tegmark et al. 2006; Planck Collaboration 2018). However, there have been a number of small scale challenges to this picture concerning the inner density structure of dark matter (DM) halos and the relative numbers of subhalos (e.g., Weinberg et al. 2015; Bullock & Boylan-Kolchin 2017, and references therein). Many authors have proposed solutions to these problems that involve a more detailed treatment of the baryonic physics of galaxy formation (e.g., Pontzen & Governato 2012; Martizzi et al. 2013; Schaller et al. 2015a). Furthermore, given the continued absence of directly detected

DM particles (Marrodán Undagoitia & Rauch 2016; Akerib et al. 2017; Aprile et al. 2018), attempts to explain these astrophysical discrepancies with modifications of the physics of DM have become increasingly appealing. Frequently considered modifications include allowing for self-interactions (SIDM; e.g., Carlson et al. 1992; Rocha et al. 2013; Wittman et al. 2018) and increasing the DM temperature at the time of thermal decoupling (Warm DM; e.g., Davis et al. 1981; Lovell et al. 2017; Bozek et al. 2019). For overviews of the intersection of astrophysics and particle physics searches for DM, we refer readers to the reviews of Bertone et al. (2005), Profumo (2017), and Buckley & Peter (2018).

One promising class of models posits that the DM particle is an extremely low-mass ($\ll 1$ eV)[1] spin-0 boson (i.e., a scalar field) manifesting quantum mechanical wave-like behavior on astrophysical scales ($\sim$kpc; Colpi et al. 1986; Lee & Koh 1996; Hu et al. 2000; Matos et al. 2009; Hui et al. 2017). Axions, a proposed solution to the strong Charge-Parity (CP) problem in particle physics (Peccei & Quinn 1977; Dine et al. 1981), are a well-motivated class of models that provide one such candidate DM particle. There are a variety of names for these DM models: ultra-light axion DM, scalar field DM, Bose-Einstein condensate DM, wave DM, or fuzzy DM. Here we adopt the term Fuzzy Dark Matter (FDM) for ultra-light ($m \sim 10^{-22}$ eV) non-thermal (i.e., restricted to the ground state) models lacking self-interaction. We refer to the mass of the DM scalar field in this model in its dimensionless form as $m_{22} = m/10^{-22}$ eV.

We note that for any model in which an ultra-light scalar field is the dominant contributor to DM, its production mechanism must necessarily be non-thermal (Marsh

---

[1] For particle masses, we use the convention that $c = 1$, giving mass and energy the same physical dimensions.

2016), in contrast with the thermal production of weakly interacting massive particles in the standard CDM cosmology (Bringmann & Hofmann 2007). Thermal production of such a low mass of DM would lead to hot (i.e. ultra-relativistic) DM, in conflict with observations of the matter power spectrum and the cosmic microwave background (CMB; e.g., Viel et al. 2005). For a broad overview of FDM cosmologies, we refer interested readers to Marsh (2016) and Hui et al. (2017).

The salient phenomena associated with FDM cosmologies are a cutoff in the halo mass function below $\sim 10^9\ M_\odot$, and distinct density cores in the inner ~ 1 kpc of DM halos, with a lighter scalar field mass resulting in a higher halo mass cutoff and a more massive inner core (Hu et al. 2000). This cutoff in the halo mass distribution implies less correlation of structure on smaller scales and the delayed formation of galaxies relative to CDM. The measured CMB and galaxy power spectra imply that, if FDM makes up the majority of DM in the universe, m_{22} must be $\gtrsim 10^{-3}$ (Hlozek et al. 2015). Constraints from the Lyα forest power spectrum imply that $m_{22} \gtrsim 1$, with some models excluding scalar field masses up to $m_{22} \sim 30$ (Armengaud et al. 2017; Nori et al. 2019). Complementary constraints on FDM models from both high redshift galaxy luminosity functions and the Milky Way satellite luminosity function are also consistent with $m_{22} \gtrsim 1$ (Bozek et al. 2015; Schive et al. 2016; Nadler et al. 2019).

The stellar dynamics of nearby galaxies offer further opportunities to test FDM models. The inner density structures of DM halos that form in an FDM cosmology follow a stationary wave, or soliton, solution to the Schrödinger–Poisson equation (Schive et al. 2014a; Marsh & Pop 2015). In the outer region the halo density profile transitions to a normal CDM halo profile (e.g., a Navarro-Frenk-White (NFW) profile, Navarro et al. 1997). The sizes of these cores are predicted to scale inversely with halo mass, while the symmetry of the soliton solution requires the core density to scale inversely with the core size (Schive et al. 2014a). Higher mass halos are therefore predicted to have smaller but denser cores.

Many previous studies of FDM density profiles in galaxies have focused on either dwarf spheroidal (dSph) or ultra-faint dwarf (UFD) galaxies (e.g., Lora & Magaña 2014; Marsh & Pop 2015; Chen et al. 2017; González-Morales et al. 2017), as their high dynamical mass-to-light ratios minimize the impact of systematic assumptions about the stellar mass distribution. Studies have generally found $m_{22} \sim 1$ (within a factor of a few), in slight tension with the Lyα constraints. Calabrese & Spergel (2016) found that the stellar kinematics of two UFDs were consistent with $m_{22} \sim 4$, though they noted the lack of kinematic measurements outside of the inferred core radius. More recently, Marsh & Niemeyer (2019) applied the stochastic density fluctuation model of El-Zant et al. (2016) to study how FDM would cause dynamical heating of the star cluster in the UFD Eridanus II. They argued that the survival of the EriII star cluster implies $m_{22} \gtrsim 1000$, whereas the existence of EriII itself implies $m_{22} \gtrsim 10$.

Looking toward more massive galaxies to probe FDM scaling relations presents increasing difficulties in disentangling the baryonic and dark mass components. In the halo mass range of 10^{10} - 10^{11} $M_{\odot}$, low surface brightness (LSB) galaxies have proven to be the most amenable to analysis. Bernal et al. (2018) modeled the rotation curves of 18 LSBs, and their results favored a lower value of $m_{22} \sim 0.05$ (though see Bar et al. 2019 for a discussion of the impact of the baryons on the FDM density structure). Bar et al. (2018) also modeled the rotation curves of LSBs under the assumption of the previously mentioned soliton–halo scaling relations, finding that, the data were in tension with $1 \lesssim m_{22} \lesssim 10$.

With the discovery of a vast population of even lower surface brightness "ultra-diffuse" galaxies (UDGs; van Dokkum et al. 2015; Mihos et al. 2015; Koda et al. 2015), we now have more opportunities to test FDM in a broader range of galaxy masses and environments. The Coma Cluster UDG Dragonfly 44 was shown to have a large stellar velocity dispersion, corresponding to a DM halo with a mass on the order of that of the Milky Way (van Dokkum et al. 2016). In a companion paper, van Dokkum et al. (2019) (hereafter Paper I), we present new spatially-resolved spectroscopy of Dragonfly 44, confirming that the potential of the galaxy is indeed dominated by DM. In this work, we address the question of whether or not the dynamics of Dragonfly 44 are consistent with FDM.

Throughout this work we assume the Planck Collaboration 2018 values of relevant cosmological parameters, including $H_0 = 67.66$ km s^{-1} Mpc^{-1} and $\Omega_m = 0.3111$.

In Section 5.2 we summarize the photometric and spectroscopic data for Dragonfly 44. We describe the Jeans modeling formalism and mass modeling assumptions in Section 5.3. In Section 5.4 we present our derived constraints on FDM models, and we place our results in context with other FDM studies in Section 5.5.

5.2 Data

Readers interested in a detailed description of the spectroscopic observations, data reduction, and kinematic extraction are referred to Paper I; here we provide a brief summary of the observational data for Dragonfly 44. We adopt a standard distance to Coma of 100 Mpc for the galaxy, which has an associated distance modulus $m - M = 35$ and an angular distance conversion factor of 0.485 kpc arcsec^{-1}.

Using the V_{606} *HST* WFC3/UVIS imaging data presented by van Dokkum et al. (2017b), we modeled the stellar light of Dragonfly 44 with a Sérsic surface brightness profile, deriving a total luminosity of $L_V = 2.33 \times 10^8\ L_{\odot,V}$, a major-axis effective radius of $R_e = 4.7$ kpc, a Sérsic index of $n = 0.94$, and an axis ratio of $b/a = 0.68$. For our modeling purposes, we adopt the circularized effective radius of $R_{e,\mathrm{circ}} = R_e\sqrt{b/a} = 3.87$ kpc.

We obtained integral field unit (IFU) spectroscopy of Dragonfly 44 with the Keck Cosmic Web Imager (KCWI) in the first half of 2018, with 17 hours of exposure time on target and an additional 8 hours on sky. We used the medium slicer with the BM grating, yielding a field-of-view of $16'' \times 20''$ and a spectral resolution of $R \sim 4000$.

For reducing the data to rectified, wavelength calibrated cubes, we used the public Keck-maintained pipeline, KDERP[2]. We aligned the individual science exposures by fitting a 2D model of the flux from the *HST* imaging data and interpolating to a common spatial grid with a spatial resolution of $\sim 1.2''$. We subtracted the sky spectrum using a principle component analysis technique – see Paper I for further details. The

---

[2] `https://github.com/Keck-DataReductionPipelines/KcwiDRP`

final signal-to-noise ratio in the optimally-combined spectrum was 48 per pixel or 96 Å^{-1}.

We extracted spectra in nine elliptical apertures following the isophotes of the galaxy. We modeled the stellar kinematic line-of-sight velocity distribution (LOSVD) as a fourth-order Gauss–Hermite function, and we fitted the LOSVD in each of these apertures by convolving it with both a high-resolution template spectrum of a synthetic stellar population and the instrumental line profile (including a wavelength-dependent resolution). From varying the ages and metallicities of the chosen stellar population template, we found the most likely values for an age of 10 Gyr and a metallicity of [Fe/H] $= -1.25$. For each spectrum we found the best fitting central velocity and higher-order (second, third, and fourth) moments of the LOSVD using a Markov Chain Monte Carlo (MCMC) simulation.

The radius of a given aperture is defined as the flux-weighted average pixel radius. There is little evidence for rotational motion in Dragonfly 44, with $v/\sigma \lesssim 0.25$ along the minor axis and $v/\sigma \lesssim 0.1$ along the major axis. We computed the effective rms velocity within each aperture as $v_{\mathrm{rms}}^2 = (v - v_{\mathrm{sys}})^2 + \sigma^2$.

5.3 Dynamical Modeling

We use the spherical Jeans modeling formalism presented in Wasserman et al. (2018a), using an updated, publicly available modeling code[3]. Under the assumptions of dynamical equilibrium and spherical symmetry, the model predicts the LOS velocity

---

[3] http://github.com/adwasser/Slomo.jl

dispersion as a function of projected galactocentric radius. See Hayashi & Obata (2019) for a discussion of the systematic uncertainty associated with applying spherical models to non-spherical systems. The main components of the model are the mass profile, $M(r)$, the tracer volume density profile, $\nu(r)$, and the orbital anisotropy profile of the tracers, $\beta_{\rm ani}(r)$. The orbital anisotropy for a spherically symmetric system is defined as

$$\beta_{\rm ani} = 1 - \sigma_t^2/\sigma_r^2 \tag{5.1}$$

where σ_t and σ_r are the tangential and radial components of the velocity dispersion.

We can compute the mean squared LOS velocity as

$$\sigma^2_{\rm los}(R) = \frac{2G}{I(R)} \int_R^\infty K_\beta\left(r, R\right) \nu(r) M(r) \frac{dr}{r} \tag{5.2}$$

where $I(R)$ is the tracer surface density profile and $K_\beta(r, R)$ is the anisotropy projection kernel. For our adopted constant anisotropy profile, the functional form of this projection kernel is given by Mamon & Łokas (2005), equation A16.

We set the stellar tracer density distribution to follow the Sérsic distribution of the star light. We assume that the stellar mass distribution follows the same Sérsic luminosity distribution used for the tracers, with the local stellar mass density given by the spatially-invariant stellar mass-to-light ratio, Υ_*, multiplied by the stellar luminosity density.

5.3.1 Halo Models

For the DM halo, we construct a flexible double power law model with a soliton core. A generalized form of the Navarro–Frenk–White (NFW) model (Navarro et al.

1997) is given by

$$\rho_{\alpha\beta\gamma}(r) = \rho_s \left(\frac{r}{r_s}\right)^{-\gamma} \left(1 + \left(\frac{r}{r_s}\right)^{\alpha}\right)^{(\gamma-\beta)/\alpha} \tag{5.3}$$

where ρ_s is the scale density, r_s is the scale radius, γ is the negative inner log slope, β is the negative outer log slope, and α controls the sharpness of the transition between the two slopes (Hernquist 1990; Di Cintio et al. 2014). For $(\alpha, \beta, \gamma) = (1, 3, 1)$, this is the typical NFW profile, which we assume to be an appropriate approximation for CDM halos in the absence of baryonic effects or FDM cores.

The inner soliton core region from FDM has the density profile

$$\rho_{\text{soliton}}(r) = \rho_{\text{sol}} \left(1 + \left(\frac{r}{r_{\text{sol}}}\right)^2\right)^{-8} \tag{5.4}$$

where ρ_{sol} and r_{sol} are the soliton scale density and scale radius, respectively (Schive et al. 2014a; Marsh & Pop 2015; Robles et al. 2019). Note that we use a slightly different definition of the soliton radius than Schive et al. (2014a) and Robles et al. (2019); their core radius, r_c, refers to the radius where the density has fallen to half of the central density, and it is equivalent to 0.3017 r_{sol}. In addition to eliminating a numeric constant from the equations, our choice of definition for the soliton radius makes the ratio of the transition radius to the soliton radius near unity (see Section 5.5.3).

From the symmetry of the soliton solution, the soliton scale density and radius are related to the scalar field mass as

$$\frac{\rho_{\text{sol}}}{M_\odot \text{kpc}^{-3}} = 8.755 \times 10^6 \; h^{-2} \; m_{22}^{-2} \left(\frac{r_{\text{sol}}}{\text{kpc}}\right)^{-4} \tag{5.5}$$

where h is the Hubble parameter in units of 100 Mpc km s^{-1}, and m_{22} is the scalar field mass in units of 10^{-22} eV (Marsh & Pop 2015).

We match the inner soliton profile with the outer $\alpha\beta\gamma$ profile at the transition radius, r_t, by finding the root of the function corresponding to the difference between the two profiles. This guarantees that the density profile,

$$\rho(r) = \begin{cases} \rho_{\text{soliton}}(r) & r < r_t \\ \\ \rho_{\alpha\beta\gamma}(r) & r \geq r_t \ , \end{cases} \tag{5.6}$$

is a continuous function, and the transition radius is thus fixed for a given set of outer halo and soliton parameters. We reject any model that fails to converge due to the inner profile being less dense than the outer profile at all radii. The transition radius is found in simulations to be a factor of a few times the core radius of the soliton, and the transition between the soliton and normal CDM profiles is sharp (Schive et al. 2014a; Mocz et al. 2017). While FDM halo density profiles are continuous, their density derivatives are not.

The enclosed mass in the $\alpha\beta\gamma$ model is

$$M_{\alpha\beta\gamma}(r) = \frac{4\pi\rho_s r_s^3}{\omega}\left(\frac{r}{r_s}\right)^{\omega} {}_2F_1\left[\frac{\omega}{\alpha}, \frac{\beta-\gamma}{\alpha}, 1+\frac{\omega}{\alpha}; -x^{\alpha}\right] \tag{5.7}$$

where $\omega = 3 - \gamma$ and ${}_2F_1$ is the hypergeometric function. For the limiting case of the NFW profile, this simplifies to

$$M_{\text{NFW}}(r) = 4\pi\rho_s r_s^3\left[\ln\left(1+\frac{r}{r_s}\right) - \frac{r}{r_s + r}\right] \ . \tag{5.8}$$

The enclosed mass of the soliton has an analytic form[4] and is given by

$$\begin{aligned}
M_{\rm soliton}(r) &= \int_0^r 4\pi\tilde{r}^2\rho_{\rm soliton}(\tilde{r})d\tilde{r} \qquad (5.9)\\
&= 4\pi\rho_{\rm sol}{r_{\rm sol}}^3\int_0^{r/r_{\rm sol}} x^2\left(1+x^2\right)^{-8}\ dx\\
&= 4\pi\rho_{\rm sol}{r_{\rm sol}}^3\int_0^{\theta} \tan^2(\theta)\sec^{-16}(\theta)\sec^2(\theta)\ d\theta\\
&= 4\pi\rho_{\rm sol}{r_{\rm sol}}^3\int_0^{\theta} \sin^2(\theta)\cos^{12}(\theta)\ d\theta
\end{aligned}$$

where in the second-to-last line we have used the trigonometric substitution $r/r_{\rm sol} = \tan(\theta)$. The integral in the last line can then be iteratively integrated by parts, yielding the following solution.

$$M_{\rm soliton}(r) = M_{\rm sol}\frac{1}{K}\left[k_0\theta + \sum_{i=1}^{7} k_i\sin(2i\theta)\right] \qquad (5.10)$$

where $M_{\rm sol} = 4\pi\rho_{\rm sol}{r_{\rm sol}}^3$, $K = 1720320$ and the other constant factors are given in the table below.

k_0	k_1	k_2	k_3	k_4	k_5	k_6	k_7
27720	17325	-1155	-4235	-2625	-903	-175	-15

Table 5.1: Coefficients for the analytic solution to the soliton enclosed mass profile (Equation 5.10).

From Equation 5.5, we can also express $M_{\rm sol}$ as

$$M_{\rm sol} = 1.1\times10^8\ M_\odot\ h^{-2}\ m_{22}^{-2}\left(\frac{r_{\rm sol}}{\rm kpc}\right)^{-1}. \qquad (5.11)$$

---

[4] The existence of such an analytic form was noted by Marsh & Pop (2015), but the derivation of this profile was left as an exercise to the reader.

Our generic halo mass profile is then given by

$$M(r) = \begin{cases} M_{\text{soliton}}(r) & r < r_t \\ \\ \Delta M_{\alpha\beta\gamma}(r) + M_{\text{soliton}}(r_t) & r \geq r_t \end{cases} \tag{5.12}$$

where $\Delta M_{\alpha\beta\gamma}(r) = M_{\alpha\beta\gamma}(r) - M_{\alpha\beta\gamma}(r_t)$.

We parameterize the halo with the virial mass and concentration, using the "200c" convention such that the virial radius is given by the relation

$$M(r_{200\text{c}}) = 200\rho_{\text{crit}}\frac{4\pi}{3}r_{200\text{c}}^3 \tag{5.13}$$

and $c_{200\text{c}} = r_{200\text{c}}/r_{-2}$. Note that here we use the convention that the halo concentration is given by the radius where the halo log slope is equal to -2. This is related to the halo scale radius as

$$r_{-2} = \left(\frac{2-\gamma}{\beta-2}\right)^{1/\alpha} r_s \ . \tag{5.14}$$

Generally speaking, we must be careful in our definition of the halo virial mass and concentration. Since the soliton core contributes to the mass of a halo, the outer halo density and radius scale parameters for a FDM halo of a given virial mass and concentration are necessarily different than those for a normal CDM halo.

However from the predicted scaling relation between soliton core mass and halo mass, we would expect a $10^{10}\ M_\odot$ halo to have $\lesssim 1\%$ of its mass locked up in the soliton core, with this fraction decreasing with increasing halo mass (Robles et al. 2019). Thus given the expected halo mass range of Dragonfly 44 of $\sim 10^{11} - 10^{12}\ M_\odot$, we assume that the differences in the outer halo scale parameters in the FDM and CDM models at fixed halo mass and concentration are negligible. We later verify the validity of this assumption by comparing the inferred virial mass with one computed from the posterior mass profile, finding a negligible difference.

This generic double-power law plus soliton halo model has eight free parameters ($\beta_{\rm ani}$, $M_{\rm 200c}$, $c_{\rm 200c}$, α, β, γ, m_{22}, $r_{\rm sol}$) and it would be poorly constrained by the available kinematic data. Thus, we consider the following constraints.

We impose a prior on $c_{\rm 200c}$ by using the halo mass–concentration relation (HMCR) from Diemer & Kravtsov (2015). Practically this is accomplished by sampling both $M_{\rm 200c}$ and $c_{\rm 200c}$, then using a log-normal prior on $c_{\rm 200c}$ whose mean is the HMCR prediction conditioned on the sampled $M_{\rm 200c}$, and whose scatter is 0.16 dex.

We consider two possibilities for the $\alpha\beta\gamma$ slope parameters. First, in the limit of no baryonic effects, we assume the outer halo follows an NFW profile with $(\alpha, \beta, \gamma) = (1, 3, 1)$. Alternatively assuming that baryonic feedback – such as cycles of bursty star formation – plays an important role, we use the halo scaling relations from the hydrodynamics simulations of Di Cintio et al. (2014), which map variation in $x = \log(M_*/M_{\rm vir})$ to α, β, and γ (see their Equation 3, also copied below as Equation 5.15).

$$\begin{aligned}
\alpha &= 2.94 - \log_{10}\left[(10^{x+2.33})^{-1.08} + (10^{x+2.33})^{2.29}\right] \\
\beta &= 4.23 + 1.34x + 0.26x^2 \\
\gamma &= -0.06 + \log_{10}\left[(10^{x+2.56})^{-0.68} + (10^{x+2.56})\right]
\end{aligned} \tag{5.15}$$

For Dragonfly 44, this results in a shallower CDM halo, with $\gamma \sim 0.3$.

To summarize, in addition to the CDM halo models described in Paper I, we have added two halo models by including the soliton core component from the FDM model, with both NFW and $\alpha\beta\gamma$ outer halo profiles.

Despite the constraints of the above assumptions, the task of inferring the properties of an FDM halo in Dragonfly 44 are substantial. Figure 5.1 illustrates the difficulty by comparing velocity dispersion profiles from expected FDM halo models with their CDM counterparts.

5.3.2 Bayesian Inference

We use a Gaussian likelihood to model the stellar velocity dispersion data, $\sigma_i \pm \delta\sigma_i$ in apertures with projected galactocentric radii, R_i. For a given halo model and model parameters, the predicted velocity dispersion, $\sigma_{\rm J}$, is modeled by Equation. 5.2. The log likelihood is thus

$$\ln \mathcal{L} = \sum_i -\frac{1}{2}\left(\ln(2\pi\delta\sigma_i^2) + \left(\frac{\sigma_i - \sigma_{\rm J}(R_i)}{\delta\sigma_i}\right)^2\right) . \tag{5.16}$$

We use uniform priors over the log of the halo mass, scalar field mass, and soliton scale radius. For the orbital anisotropy, we use a uniform prior over the symmetrized anisotropy parameter, $\tilde{\beta}_{\rm ani} = -\log_{10}(1-\beta_{\rm ani})$. This ensures that radial and tangential orbits are given equal weight. We use the HMCR as a prior for the concentration, as described in the previous section. For the stellar mass-to-light ratio, we use a log-normal distribution with mean $\log_{10}\Upsilon_{*,V} = \log_{10}(1.5)$ and a scatter of 0.1 dex. Here the mean value chosen is typical of an old, low metallicity stellar population, while the chosen

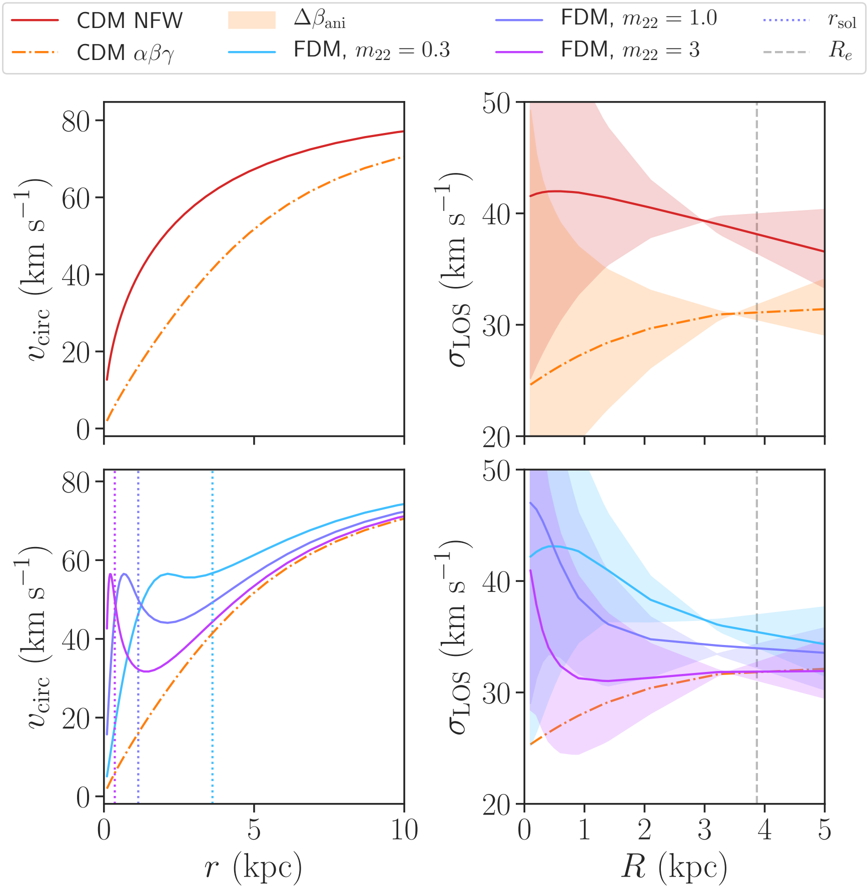

Figure 5.1: Illustration of mass models and their associated velocity dispersion profiles for different halo models described in Section 5.3.1. The top panels show CDM models with $\log_{10} M_{\rm 200c}/M_\odot = 11$, $c_{\rm 200c} = 10.5$, and $r_s = 9.3$ kpc. The red solid line shows a cuspy NFW halo and the orange dot-dashed line shows a cored $\alpha\beta\gamma$ halo. The bottom panels show FDM halos with an outer $\alpha\beta\gamma$ halo profile (plotted again for comparison) for a range of possible values of m_{22}. The left-hand panels show the circular velocity profile associated to the halo, while the right-hand panels show the line-of-sight velocity dispersion profile. The range of orbital anisotropy values (from $\beta_{\rm ani} = -1$ to 0.5) is shown by the shaded region, with the line indicating the isotropic ($\beta_{\rm ani} = 0$) profile. Tangentially-biased profiles ($\beta_{\rm ani} < 0$) generally display velocity dispersion profiles that increase with radius, while radially-biased profiles generally fall with radius. In the bottom left panel, the dotted lines show the expected soliton scale radius associated to each FDM halo (see Section 5.5.2). As the FDM scalar field mass gets larger, the profile approaches its CDM analogue, with the deviations occurring on increasingly smaller scales. FDM is more "detectable" for lower m_{22} values where there is more mass in the

scatter matches that found by Taylor et al. (2011) from the GAMA survey. We show a summary of these model parameters and our priors in Table 5.2.

For each halo model, we sample from our posterior probability distribution,

$$\mathrm{Post}(\theta|(\sigma, \delta\sigma, R), \mathrm{Model}) \propto \frac{\mathcal{L}(\sigma|R, \mathrm{Model}, \theta)}{\mathrm{Prior}(\theta)} \tag{5.17}$$

by using the affine-invariant ensemble MCMC algorithm of Goodman & Weare (2010). We run chains of 128 walkers for 4000 iterations, rejecting the first 2000 iterations where the MCMC might not have converged. We visually inspect the trace plots to verify that this is an adequate number of burn-in iterations.

Parameter	Unit	Prior	CDM + NFW	FDM + NFW	CDM + $\alpha\beta\gamma$	FDM + $\alpha\beta\gamma$
$\log_{10} M_{200c}$	$M_\odot$	$\mathcal{U}(7, 15)$	$10.62^{+0.42}_{-0.30}$	$10.64^{+0.41}_{-0.32}$	$11.20^{+0.63}_{-0.63}$	$11.16^{+0.58}_{-0.58}$
$\log_{10} c_{200c}$	–	HMCR	$1.00^{+0.19}_{-0.20}$	$0.98^{+0.18}_{-0.19}$	$0.98^{+0.13}_{-0.16}$	$0.99^{+0.12}_{-0.14}$
$\log_{10} \Upsilon_*$	$M_\odot/L_{\odot,V}$	$\mathcal{N}(0.176, 0.1)$	$0.18^{+0.10}_{-0.10}$	$0.18^{+0.10}_{-0.10}$	$0.19^{+0.10}_{-0.10}$	$0.18^{+0.10}_{-0.10}$
$\tilde{\beta}_{\rm ani}$	–	$\mathcal{U}(-1.5, 1.5)$	$-0.24^{+0.10}_{-0.12}$	$-0.44^{+0.22}_{-0.29}$	$-0.05^{+0.08}_{-0.11}$	$-0.16^{+0.15}_{-0.39}$
$\log_{10} m_{22}$	10^{-22} eV	$\mathcal{U}(-3, 3)$	–	$0.34^{+0.76}_{-0.25}$	–	$0.51^{+0.62}_{-0.44}$
$\log_{10} r_{\rm sol}$	kpc	$\mathcal{U}(-2, 1)$	–	$-0.22^{+0.25}_{-0.34}$	–	$-0.16^{+0.25}_{-0.26}$

Table 5.2: Model parameters for the two CDM halo models from Paper I and the two FDM halo models presented in this work. The parameters are, from top to bottom, the halo virial mass, the halo concentration, the stellar mass-to-light ratio, the symmetrized anisotropy parameter ($\tilde{\beta}_{\rm ani} = -\log_{10}(1 - \beta_{\rm ani})$), the scalar field mass, and the soliton core radius. Columns show the chosen parameterization, relevant units, the prior distribution, and posterior summaries for the four halo models. For the priors, $\mathcal{U}(\ell, u)$ denotes a uniform prior with lower bound ℓ and upper bound u, $\mathcal{N}(\mu, \sigma)$ denotes a Gaussian prior with mean μ and standard deviation σ, and HMCR refers to the halo mass–concentration relation prior (see Section 5.3.1). Posterior distributions are summarized as the median of the distribution and the distance to the 16th and 84th percentiles.

5.4 Results

Table 5.2 summarizes the posterior distributions for the different halo mass models. The full posterior distributions are shown as marginalized 1D and 2D histograms in Appendix 5.7.1.

We find that all models we consider are able to reproduce the observed velocity dispersion profile, as shown in Figure 5.2. We assess the relative quality of these models using leave-one-out cross validation (LOO-CV; Vehtari et al. 2015; Piironen & Vehtari 2017), finding no significant differences in the goodness-of-fit of FDM models relative to the CDM models. Translating the differences between models in their calculated LOO-CV information criteria into probabilities, we find that no model is more than ~ 0.3 times as likely as any other model to best describe the data. In other words, the increase in goodness-of-fit from the FDM models is not enough to compensate for the increased model freedom (i.e., the additional model parameters).

As demonstrated in Figure 5.3, the dynamical mass profile is best constrained at the maximum radius of the kinematic tracers (~ 5 kpc), with $M_{\rm dyn}(< 5~{\rm kpc}) = 3.4^{+0.5}_{-0.4}(\pm 0.1) \times 10^9~M_\odot$, where the systematic uncertainty (in parentheses) comes from the standard deviation between the four models.

Figure 5.3 also demonstrates the systematic effect that the choice of halo model has on the inferred circular velocity profile, with both CDM and FDM $\alpha\beta\gamma$ profiles preferring more massive halos than their associated NFW models by ~ 0.5 dex. This is to be expected, as the cored $\alpha\beta\gamma$ models put less mass in the inner region (where

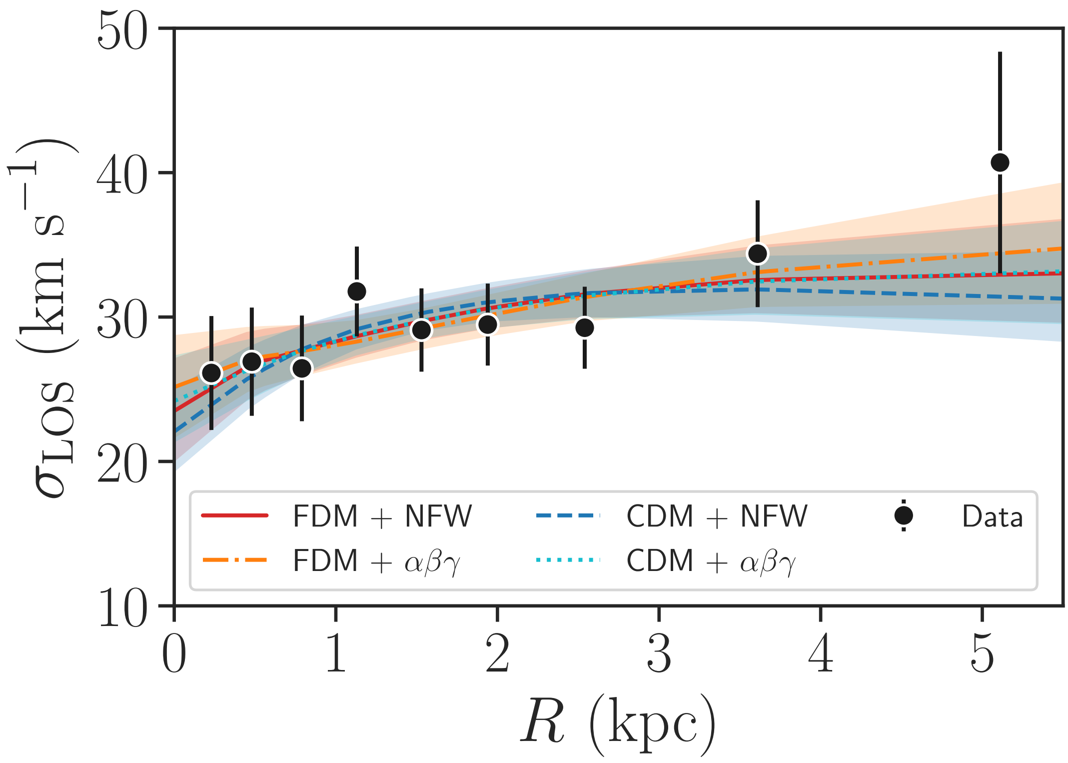

Figure 5.2: Posterior predictive checks on the velocity dispersion profiles for the FDM halo models compared with the kinematic observations, with the CDM halo models from Paper I shown for comparison. The red solid and orange dot-dashed lines show the FDM halo models for the NFW and $\alpha\beta\gamma$ outer profiles. The dark blue dashed and cyan dotted lines show the CDM halo models for the NFW and $\alpha\beta\gamma$ profiles. The shaded regions cover the 16th through 84th percentiles of the distribution. We see that all four models do an adequate job of recovering the general trend of the kinematic data.

we have kinematic constraints) compared to NFW models of the same halo mass. The differences in inferred halo mass between halo models are consistent within the statistical uncertainties from the spread in the posterior distributions, and the deviations indicates the difficulty in robustly extrapolating halo masses out to spatial scales where we lack data.

The analysis of higher order LOS velocity moments (e.g., kurtosis) may help in distinguishing cuspy density profiles (NFW) from shallower cored profiles ($\alpha\beta\gamma$), as discussed by Paper I. The high value of $h_4 = 0.13 \pm 0.05$ measured for the Dragonfly 44 stellar kinematic data slightly favors the $\alpha\beta\gamma$ model (predicted $h_4 = 0.01 \pm 0.01$) over the NFW model (predicted $h_4 = 0.03 \pm 0.02$). However since h_4 is more susceptible to systematic biases than the velocity dispersion, we remain largely agnostic about which halo model (and hence which associated value for the halo mass) is correct.

As expected, the choice of CDM or FDM models has the most impact on the inner mass profile, with FDM models allowing a $\sim 10^9\ M_\odot$ core within 1 kpc. The inner mass distribution is degenerate with both the chosen model and the orbital anisotropy (see Figure 5.4), with the FDM models preferring more DM inside of 1 kpc and slightly more tangentially-biased orbits. The primary modeling systematic affecting the anisotropy distribution however is the outer DM profile (NFW or $\alpha\beta\gamma$), with the NFW model preferring tangential orbits $\beta_{\mathrm{ani}} \sim -0.8$ and the $\alpha\beta\gamma$ model preferring isotropic orbits. We note that models with tangentially-biased orbits will hide the signal of the v_{circ} soliton bump when projecting to the LOS velocity dispersion.

Figure 5.5 shows the ratio of the enclosed (i.e., cumulative) DM mass to stellar

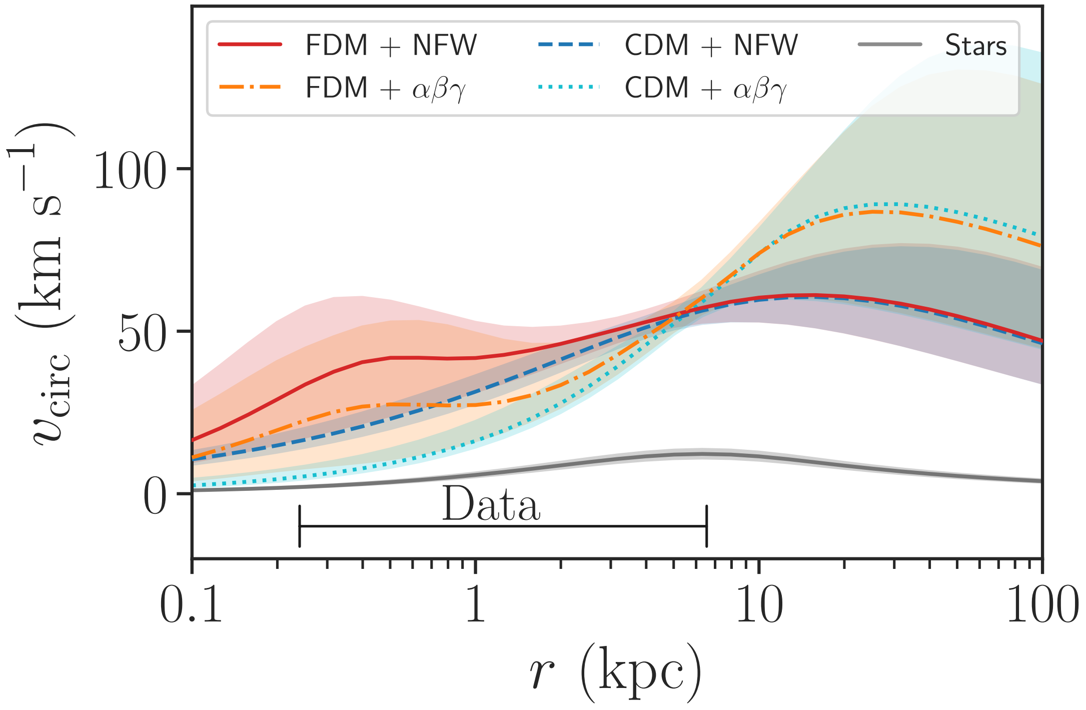

Figure 5.3: Circular velocity corresponding to the dynamical mass (DM + stars) for the FDM halo models, compared with their CDM halo counterparts. Note that these are profiles in de-projected (3D) radius, in contrast to the projected (2D) radial profiles shown in Figure 5.2. The bottom gray solid line shows the circular velocity profile corresponding to just the stellar mass for the NFW model. The black bar at the bottom indicates the spatial extent of the kinematic data. The dynamical mass within 5 kpc ($\sim R_e$) is well constrained by the data, but the mass within 1 kpc is degenerate with the chosen model.

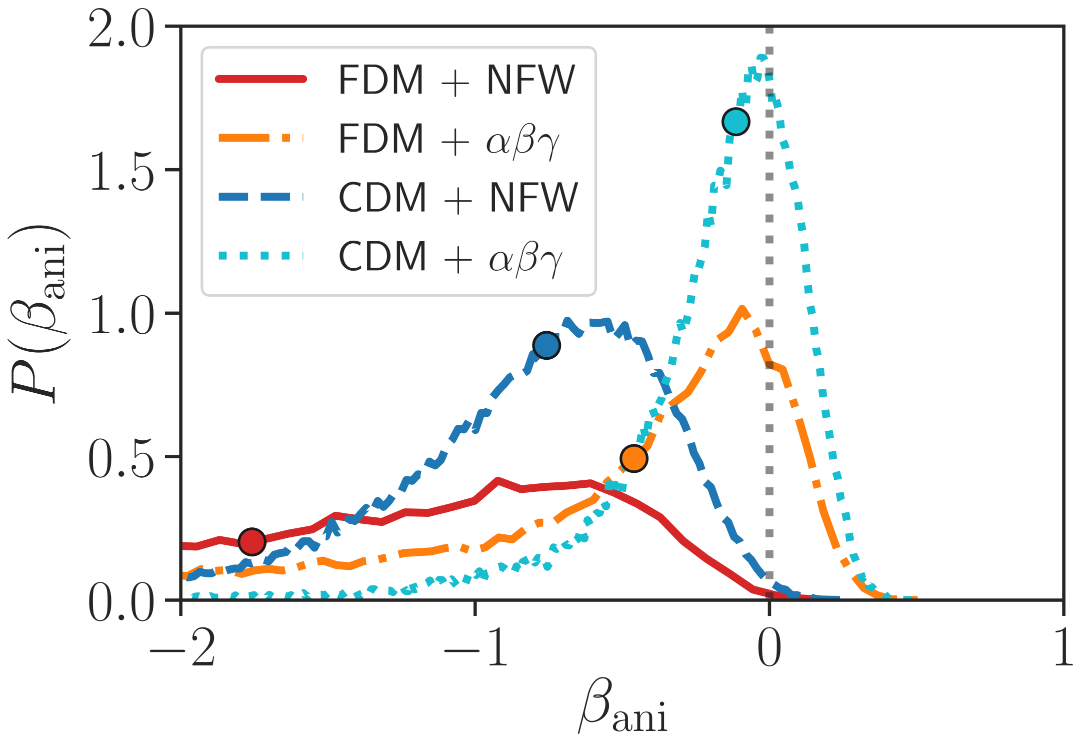

Figure 5.4: Posterior distributions of the orbital anisotropy parameter for the FDM halo models, compared with their CDM halo counterparts. The median of each distribution is marked by circles. The NFW models (both for CDM and FDM) prefer tangentially biased orbits ($\beta_{\rm ani} < 0$), with the tail of the distributions extending to the prior bound at $\tilde{\beta}_{\rm ani} = -1.5$ ($\beta_{\rm ani} = -30.6$). The $\alpha\beta\gamma$ models are consistent with isotropic orbits ($\beta_{\rm ani} = 0$, shown by the gray dotted line), but all of the posterior distributions are skewed in the direction of tangential anisotropy.

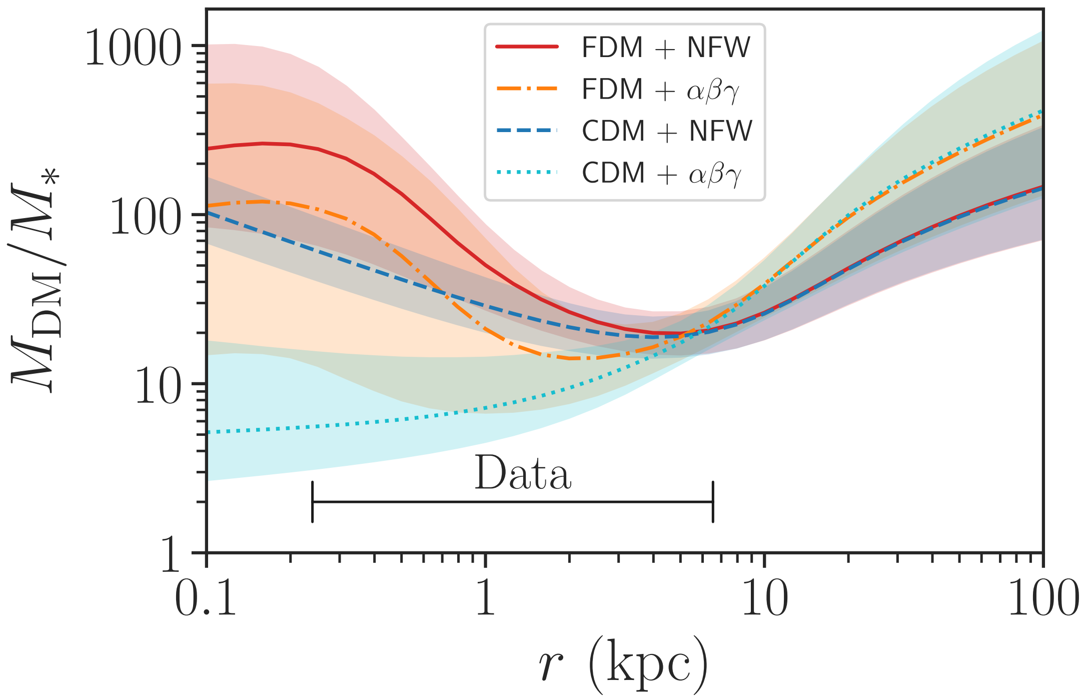

Figure 5.5: Ratio of DM to stellar mass as a function of radius for the FDM halo models, compared with their CDM halo counterparts. The black bar at the bottom indicates the spatial extent of the kinematic data. All four models show Dragonfly 44 to be DM-dominated ($M_{\mathrm{DM}}/M_* > 1$) down to ~ 0.1 kpc.

mass as a function of radius, and it confirms that Dragonfly 44 is DM-dominated ($M_{\mathrm{DM}}/M_* > 1$) independently of the considered cosmology (FDM/CDM) or degree of baryonic impacts (NFW/$\alpha\beta\gamma$), down to the smallest spatial scales probed by the data. As such, our inference on the mass-to-light ratio, Υ_*, is consistent with our chosen prior. With our chosen prior of $\log \Upsilon_* \sim 0.176 \pm 0.1$, $M_{\mathrm{DM}}/M_* \sim 20$ at $r = 5$ kpc, independently of the chosen mass model.

Looking at just the two FDM models, we see that they are consistent in their posterior soliton parameter distributions. Figure 5.6 shows the covariance between the scalar field mass, the total mass within the soliton core, and the ratio of the transition radius to the soliton scale radius. The modes of the distributions for both NFW and $\alpha\beta\gamma$ models have a $\sim 10^9\ M_\odot$ soliton core with a size of ~ 0.6 kpc. We find a less likely second peak in the posterior distribution for the NFW model, towards a more massive scalar field ($m_{22} \sim 10$). This region has a soliton core with mass of $\sim 10^7\ M_\odot$ that rapidly transitions to the outer NFW halo profile. Thus, this second peak corresponds to models for which the DM scalar field is too massive to create a dynamically significant core on spatial scales probed by our data. For the $\alpha\beta\gamma$ model, this region of parameter space has a similar posterior density, but this manifests as a long tail towards higher scalar field masses rather than as a discrete second mode.

While the observable velocity dispersion of the FDM models will approach that of the CDM models in the limit as $m_{22} \to \infty$ (see the bottom right panel of Figure 5.1), we caution that this does *not* mean that the bounded m_{22} posterior distribution favors FDM over CDM. Rather, as discussed in the beginning of this section, we need to statistically account for the additional model freedom that the introduction of the soliton parameters provide.

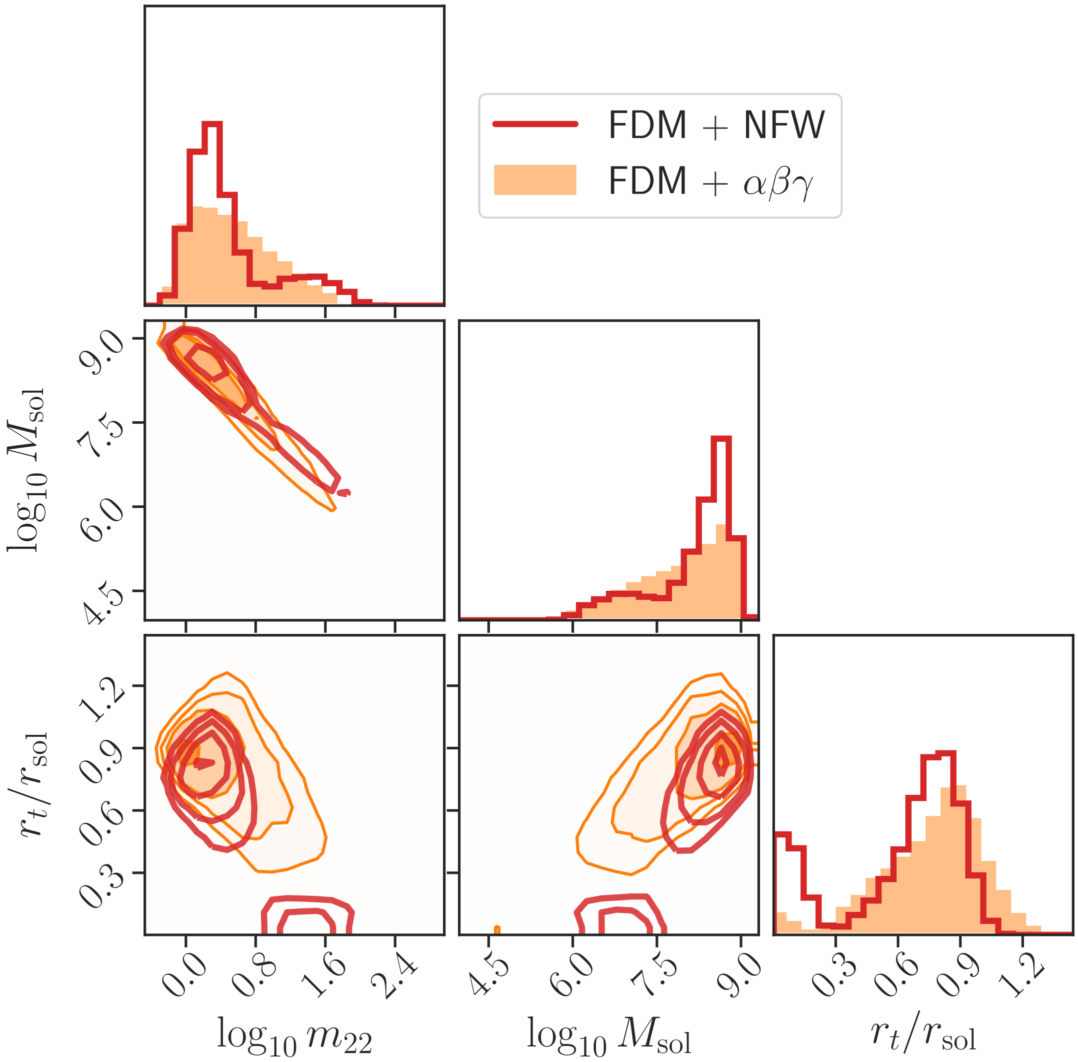

Figure 5.6: Posterior distributions for the scalar field mass in 10^{-22} eV, the mass within the soliton core (in $M_\odot$), and the ratio of the transition radius to the soliton core radius for the NFW (red, unfilled histograms) and $\alpha\beta\gamma$ (orange filled histograms) halo models. The FDM constraints are broadly similar between the two halo models, with both models favoring a core of mass $\sim 10^9\ M_\odot$. Both models show a mode in m_{22} of ~ 2, with a broad posterior tail towards higher m_{22} values. For the NFW model, we see a second mode at high m_{22}, corresponding to a negligible core mass and hence a near-zero transition radius.

5.5 Discussion

We now focus on the question of whether or not the stellar dynamics of Dragonfly 44 are consistent with the FDM hypothesis and other constraints on FDM. We find qualitatively similar FDM constraints for both the NFW and $\alpha\beta\gamma$ models (see Figure 5.6), and so for the sake of simplicity we focus on the FDM + $\alpha\beta\gamma$ model.

5.5.1 Scalar field mass

We find the DM scalar field mass to be $m_{22} = 3.3^{+10.3}_{-2.1}$.

Figure 5.7 shows this range in the context of other observational constraints on the scalar field mass. The values we find for m_{22} are similar to those for the Local Group dSph galaxies from the study of Chen et al. (2017), who found $m_{22} \sim 1.8$. González-Morales et al. (2017) found a similar value ($m_{22} \sim 2.4$) from Jeans modeling of the same data, but they cautioned that the orbital anisotropy degeneracy could cause the scalar field mass inference to be biased high. Instead of using this Jeans analysis, they advocated instead for using mass estimators with multiple stellar subpopulations (e.g., Walker & Peñarrubia 2011), for which they derived an upper bound of $m_{22} < 0.4$.

Recent work by multiple authors (e.g., Iršič et al. 2017; Armengaud et al. 2017; Kobayashi et al. 2017; Nori et al. 2019) have used the Lyα forest power spectrum to test FDM. Less massive FDM particles would result in stronger deviations from ΛCDM at small spatial scales; thus these studies infer lower bounds on the scalar field mass, with m_{22} values ranging from 7 to 30.

There are a large number of modeling assumptions that go into this lower bound, ranging from the temperature evolution of the intergalactic medium during reionization (e.g., Garzilli et al. 2017) to different priors on cosmological parameters. In addition, Desjacques et al. (2018) found that even a relatively small self-interaction term in FDM can lead to instabilities that result in notable differences (with respect to CDM) in the cosmic web, complicating the interpretation of Lyα forest clustering. Due to degeneracies between reionization history and the growth of structure, it remains uncertain to what degree the FDM constraints from low-z galaxy dynamics and the high-z Lyα power spectrum are in tension with one another. Ultimately, FDM models that reproduce both galaxy dynamics and the observed Lyα forest power spectrum may need to go beyond the simple model considered here (e.g., Leong et al. 2019).

5.5.2 Core size

The core sizes of soliton halos are predicted to scale with halo mass and scalar field mass as $r_{\rm sol} \propto m_{22}^{-1} M_h^{-1/3}$. We can see this by considering the following relations,

$$\begin{aligned} r_{\rm core} &\propto (mv)^{-1} \\ v &\propto \left(\frac{M_h}{r_h}\right)^{1/2} \\ r_h &\propto M_h^{1/3} \end{aligned} \tag{5.18}$$

where the first one is from the de Broglie wavelength of the scalar field, the second relation comes from the virial theorem, and the third one comes from the definition of the halo virial radius. Indeed, inserting relevant constants, we can recover within order

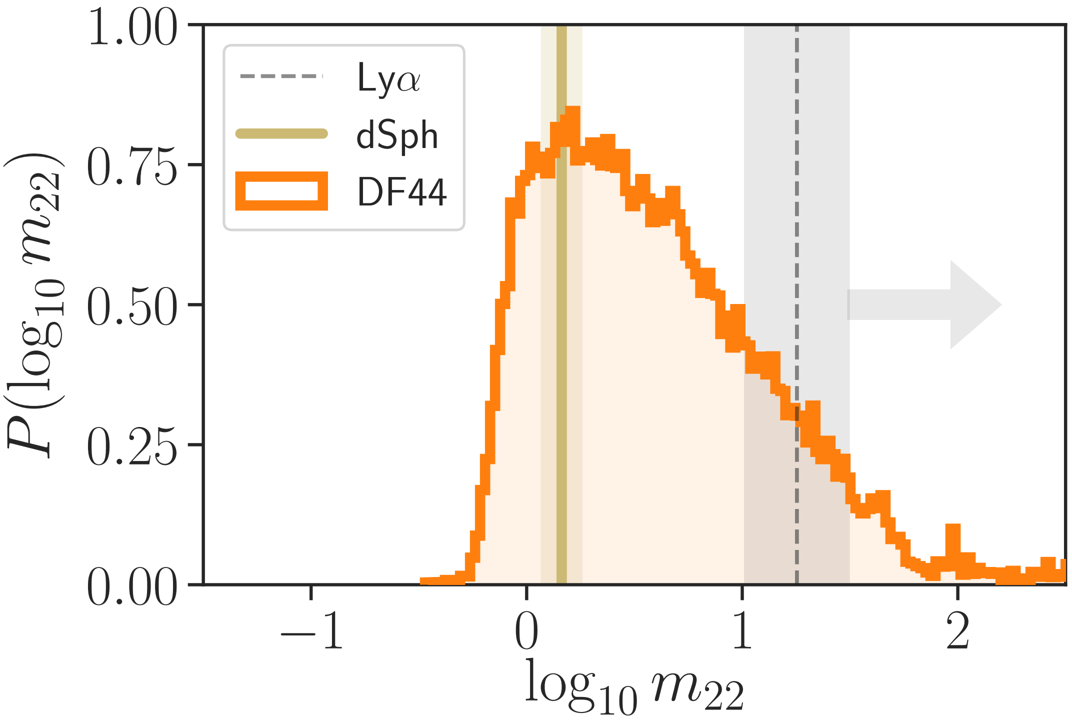

Figure 5.7: Posterior distributions of m_{22} from Dragonfly 44 (orange histogram) compared with constraints from the literature. A lower bound of $m_{22} \gtrsim 20$ from modeling of the Lyα forest (see sources in text) is shown by the gray dashed line, with the gray shaded region showing the range of lower bounds found in the literature. The constraint from dSph galaxies (Chen et al. 2017) is shown by the yellow solid line. We see that both inferences on m_{22} from Dragonfly 44 are consistent with the dSph constraints, but they are in tension with the Lyα constraint. Only $\sim 10\%$ of samples lie to the right of the Lyα lower bound.

unity the scaling relation found from FDM simulations (Schive et al. 2014b):

$$\frac{r_{\rm sol}}{\rm kpc} = 5.304 \left(\frac{M_h}{10^9 M_\odot} \right)^{-1/3} m_{22}^{-1} \ . \tag{5.19}$$

We could in principle use Equation 5.19 as an informative prior on $r_{\rm sol}$, which would result in stronger constraints on m_{22}. However, since we let $r_{\rm sol}$ be a free parameter in our modeling of FDM halos, Equation 5.19 acts as an additional consistency test for the model. Figure 5.8 shows the posterior distribution of the core size (multiplied by the scalar field mass to remove its associated scaling) and the halo mass. The mode of the posterior is well-matched to this relation. In addition, we see that our derived core size for Dragonfly 44 is less than that derived by Chen et al. (2017) for their sample of lower halo mass dSph galaxies, consistent with the direction of the soliton core size–halo mass scaling relation.

5.5.3 Transition radius

Another consistency check for our FDM models is the location of the transition from the inner soliton profile to the outer CDM-like profile (r_t from Equation 5.6). For the outer $\alpha\beta\gamma$ profile, we infer $r_t = 0.5^{+0.4}_{-0.2}$ kpc and $r_t/r_{\rm sol} = 0.8^{+0.2}_{-0.3}$. As shown in Fig. 5.6, these values are similar for the NFW model.

Using simulations of merging FDM halos, Mocz et al. (2017) interpreted this transition radius as the location where the energy density due to quantum pressure is equal to the classical kinetic energy density. They found this transition radius to occur at $r_t \sim 3.5\ r_c$ ($\sim 1\ r_{\rm sol}$).

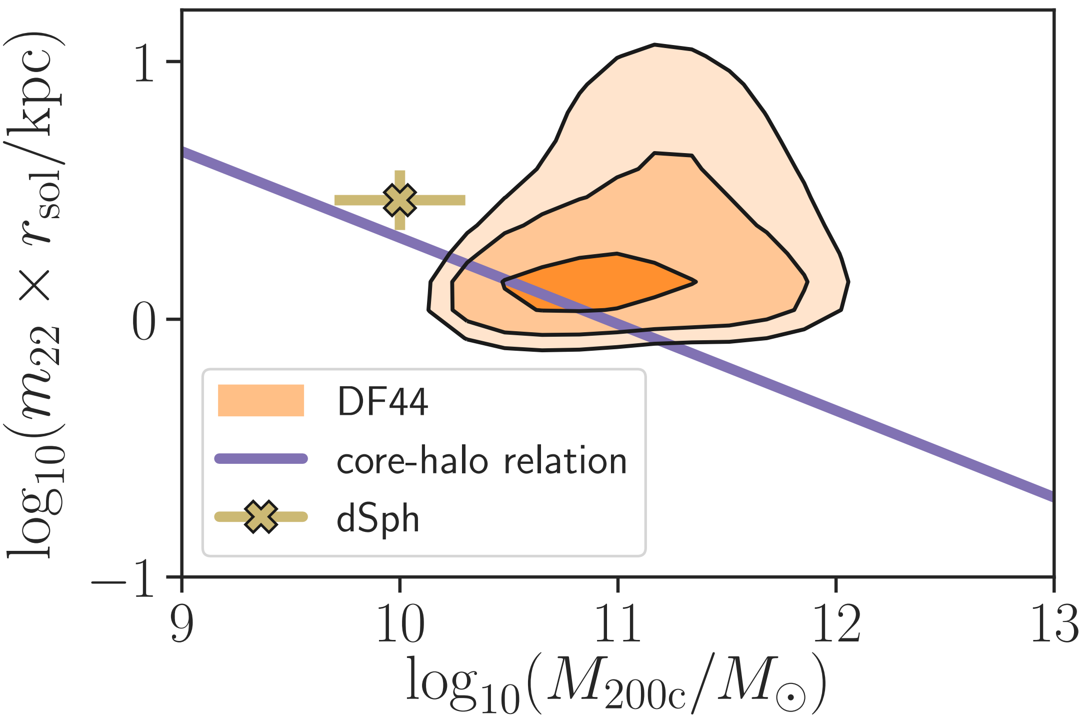

Figure 5.8: Posterior distribution of $M_{\rm 200c}$ and $m_{22} \times r_{\rm sol}$ for Dragonfly 44 compared to the expected scaling relation. The violet line shows the functional relationship between halo mass and core size predicted by Schive et al. (2014a). The yellow × shows the inferred core size from dSph galaxies (Chen et al. 2017). There is a broad range of allowed core sizes, but the mode of the distribution is consistent with the expected scaling relation.

Recent work by Robles et al. (2019) identified a plausible range for this ratio of the transition radius to the soliton core radius. The maximum of this value is set by the requirement that the radius of the peak of the circular velocity profile is less than the virial radius. The corresponding minimum of this transition ratio is set by either the requirement of a local maximum in the circular velocity profile (for halos $\lesssim 10^{11}\ M_\odot$) or by the need for the peak of the velocity profile in the FDM halo to be less than that of the corresponding CDM halo (for more massive halos). For a halo of mass $\sim 10^{11}\ M_\odot$, these requirements translate to $0.6 \lesssim r_t/r_{\rm sol} \lesssim 1.2$.

These bounds, as well as the posterior distribution for this transition ratio, $r_t/r_{\rm sol}$, are shown in Figure 5.9. We recall that our definition of the soliton core radius differs from that used by Robles et al. (2019), requiring a conversion factor of 3.315. In addition, we show the same ratio as found in the simulations of Mocz et al. (2017). Most of the posterior mass ($\sim 70\%$) as well as the mode of the distribution is inside of these bounds, indicating that the inferred soliton transition radius is in agreement with the constraints for a reasonable FDM halo.

5.5.4 Future work

One potentially rewarding area for future work would be testing FDM against galaxies with even higher halo masses than that of Dragonfly 44. Figure 5.10 shows that the difference in velocity dispersion between a CDM halo model and a FDM model (both assuming an outer $\alpha\beta\gamma$ profile) is on the order of the observational uncertainties for a halo mass similar to that of Dragonfly 44. A $10^{12}\ M_\odot$ FDM halo would be much more

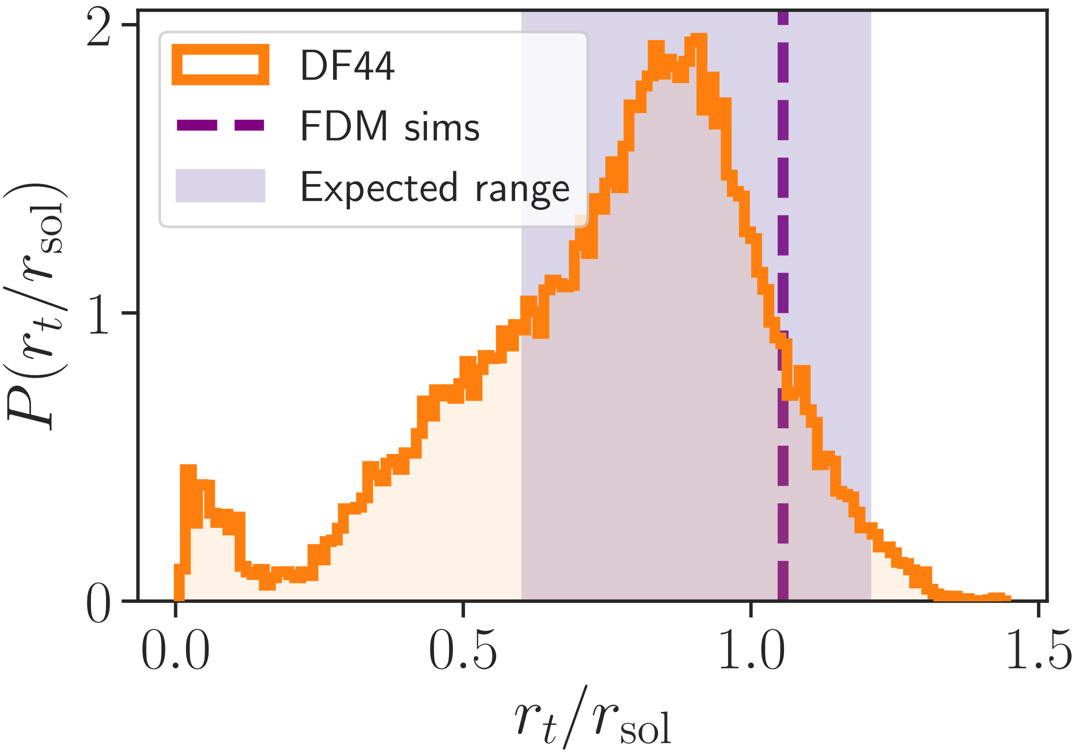

Figure 5.9: Posterior distribution of the ratio of the transition radius to the soliton scale radius for Dragonfly 44 (orange histogram), compared with the relevant bounds (violet region) for reasonable FDM halos at the inferred halo mass (see Robles et al. 2019, Sec. 2.2). The dotted violet line shows the approximate value from the FDM simulations of Mocz et al. (2017). Over two-thirds of the posterior mass for Dragonfly 44 is within these bounds, indicating good agreement with FDM predictions.

readily detected with the current observational error budget. The field UDG DGSAT I, with its high velocity dispersion of $\sigma = 56 \ \text{km s}^{-1}$(Martín-Navarro et al. 2019), may be one such promising candidate.

As discussed in Paper I, modeling higher order LOSVD moments may help break the mass–anisotropy degeneracy. Another possibility would be to use the extensive globular star cluster system of some UDGs (van Dokkum et al. 2017b) as tracers of the potential. Such multi-population Jeans modeling can also mitigate the uncertainties from orbital anisotropy (e.g., Oldham & Auger 2016; Zhu et al. 2016; Wasserman et al. 2018a).

Most simulation studies of FDM in the literature have not modeled the impact of baryons on the density structure of DM halos (with Bar et al. 2019 being a notable exception). Our crude method for marginalizing over this uncertainty was to try models with the best fit DM profiles from the hydrodynamical simulations of Di Cintio et al. (2014), which naturally assumed a CDM cosmology. Stellar feedback may be critical in forming UDGs (Di Cintio et al. 2017a; Chan et al. 2018; Jiang et al. 2019) and would likely affect the properties of soliton cores in FDM. Galaxy formation studies with WDM and SIDM (e.g., Di Cintio et al. 2017b; Fitts et al. 2019; Despali et al. 2019) have helped identify better ways of discriminating between available models, and we believe dedicated studies of galaxy formation in a FDM cosmology will be necessary to disentangle the effects of baryonic feedback and new DM physics on the observable DM mass distribution.

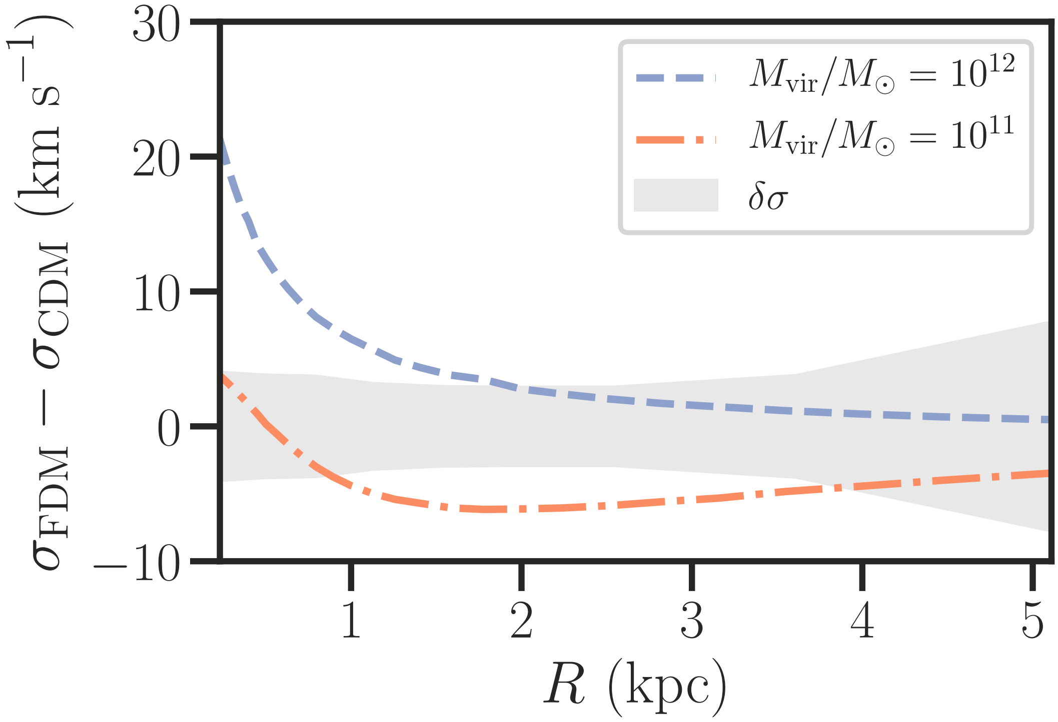

Figure 5.10: The difference in velocity dispersion between CDM and FDM models, as a function of radius. The orange dot-dashed line corresponds to a 10^{11} $M_\odot$ halo, similar to that inferred for Dragonfly 44. The blue dashed line corresponds to a 10^{12} $M_\odot$ halo, and it demonstrates a much more detectable bump in the velocity dispersion inside of 1 kpc. The gray band indicates the observational uncertainties in velocity dispersion for the Dragonfly 44 data. Note that this uncertainty region does not take into account the systematic uncertainty in the halo mass profile from the unknown virial mass and concentration.

5.6 Conclusions

We applied equilibrium dynamical models to new spatially-resolved spectroscopy of the integrated starlight of the ultra-diffuse galaxy Dragonfly 44. We considered FDM halo models in which DM consists of an ultra-light scalar field.

While we were unable to statistically distinguish between our proposed halo mass models, we were able to test the consistency of the FDM halo models. If we assume a FDM cosmology, the inferred scalar field mass and soliton core size are consistent with a range of FDM predictions, including the core size–halo mass scaling relation and the radius of transition between the soliton core and the outer halo.

The inferred scalar field mass from the Dragonfly 44 data is largely in agreement with other constraints from galaxy dynamics, however it is in tension with results from modeling the Lyα forest power spectrum. Possible solutions to these disagreements include accounting for any self-interactions in the scalar field or allowing for a mixture of FDM and CDM. Future work is needed to fully quantify this tension and to determine if FDM is a viable alternative to CDM.

5.7 Appendix

5.7.1 Posterior distributions

We show the 1D and 2D marginalized posterior distributions for each of the four halo models. The parameterization and associated units are shown in Table 5.2.

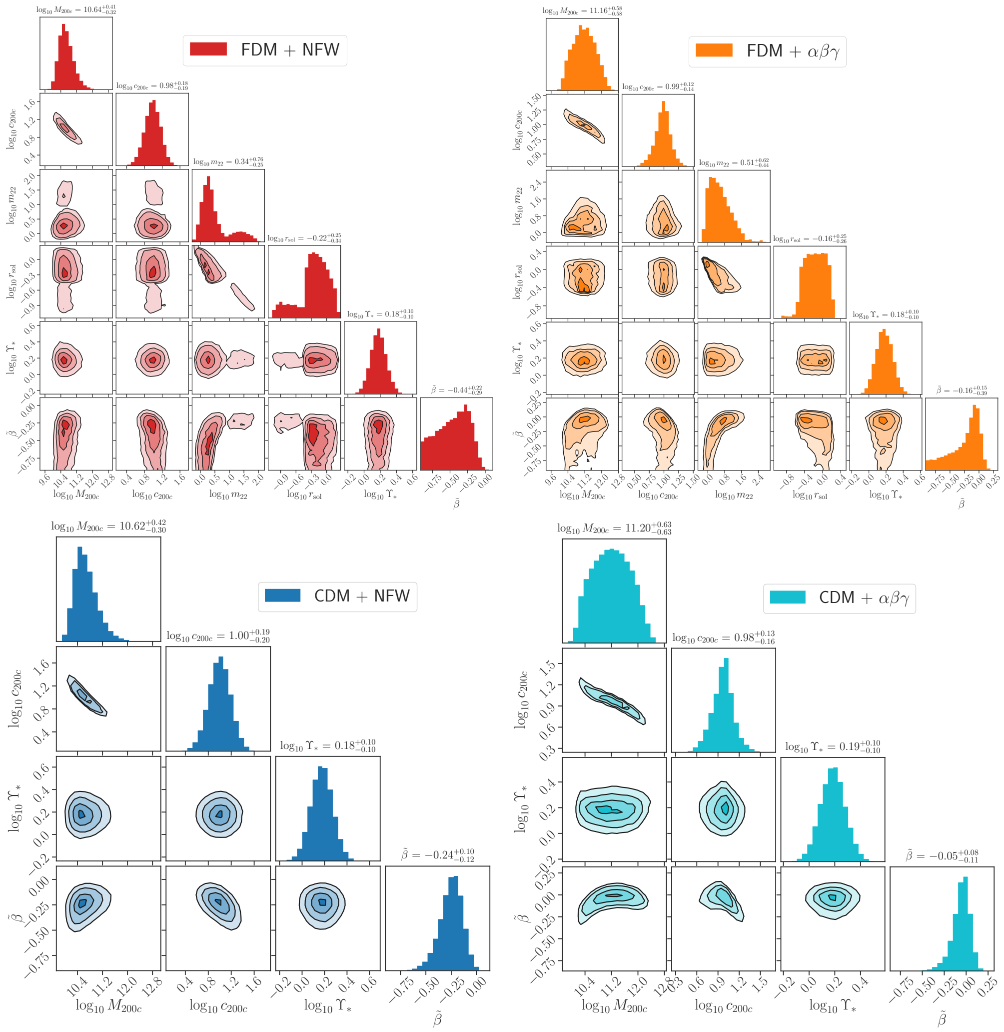

Figure 5.11: Marginalized posterior distributions for the four halo models. The top panels show the FDM models from this work. The bottom panels show the CDM models from Paper I. Left panels are for NFW halo profiles, and right panels show the results for the $\alpha\beta\gamma$ halo profiles. Within both top (FDM) panels the parameters are (from left to right, or top to bottom) the log of the halo mass, the log of the halo concentration, the log scalar field mass, the log soliton scale radius, the log of the stellar mass to light ratio, the symmetric parameterization of the anisotropy parameter. Contours show iso-density surfaces from 0.5 to 2.0 "sigma" levels (for a 2D Gaussian).

Chapter 6

Summary and future work

In this thesis I have presented a flexible model for predicting the kinematics of spherical galaxies and inferring the properties of these galaxies from kinematics of their tracer populations. I presented several applications of this model, including a multipopulation analysis of the massive elliptical galaxy NGC 1407, an uncertainty quantification for the ultra-diffuse galaxy NGC 1052-DF2, and a investigation of fuzzy dark matter models for the ultra-diffuse galaxy Dragonfly 44. There are numerous areas where extensions to this model would be promising.

6.1 Partial pooling for multiple galaxies

Chapter 3 demonstrated that it is feasible to measure the inner density structure of DM halos around nearby massive elliptical galaxies. Different physical mechanisms may be responsible for changing the log density slope, γ, ranging from adiabatic contraction and galaxy mergers, to CDM extensions such as self-interacting DM (Rocha et al. 2013).

To better understand the origin of differences in γ, we need to make measurements across a range of galaxy and halo masses. Moving one step up the hierarchical ladder to simultaneously model the dynamics of multiple galaxies at once would help constrain inferences for galaxies with noisier data and to robustly infer the relationship between γ and $M_{\rm halo}$. This method is, by no means, limited to the question of the γ–M_h relation. Indeed any proposed galaxy scaling relation can and should be used.

Partial pooling (e.g., Gelman 2006) refers to the phenomena of information sharing in a hierarchical (or more generally, multilevel) model between different levels. For instance, when inferring the mass, concentration, and inner density slope of DM halos, we can propose that all halos share some relation between these parameters, e.g.

$$
\begin{aligned}
\langle M_h \rangle &= \alpha_0^* + \alpha_h^* \log M_* \\
\langle \log c \rangle &= \alpha_0^c + \alpha_h^c \log M_h \\
\langle \log \gamma \rangle &= \alpha_0^\gamma + \alpha_h^\gamma \log M_h + \alpha_c^\gamma \log c
\end{aligned}
\tag{6.1}
$$

The first relation in the above equations is a stellar-to-halo mass relation, and we can use informative priors on the intercept and slope parameters (e.g., Rodríguez-Puebla et al. 2017). Similarly, the second relation in the above equations is simply a halo mass–concentration relation (e.g., Dutton & Macciò 2014; Diemer & Kravtsov 2015) which lead to informative priors on α_0^c and α_M^c. For the γ model, the relationship between the halo parameters is less well understood. Expectations from simulations are that $\alpha_h^\gamma < 0$ (Schaller et al. 2015a), but there exist potentially conflicting predictions

(Tollet et al. 2016).

Joint modeling of some small number of galaxies (e.g., ~ 10) is on the edge of computational convenience. However, it has been shown that importance sampling can provide a sufficient approximation to the posterior distribution for hierarchical models (Sonnenfeld et al. 2015).

6.2 Joint stellar population and DF modeling

As discussed briefly in Chapter 5.4, higher order moments of the LOSVD may help mitigate mass–anisotropy degeneracies when a multi-population analysis is unfeasible. For the spherical models that assume odd-ordered velocity moments are zero, this requires measurements of the LOS kurtosis. As mentioned by van Dokkum et al. (2019), such measurements are difficult and noisy. To properly address this challenge for integrated light spectroscopic observations of field stars would require a joint modeling of the stellar populations and the distribution function of the stellar tracers. The resulting inferences for the LOSVD should then be internally consistent with the stellar mass distribution.

6.3 Schwarzschild orbit modeling

It is clear that the simple assumptions of constant β or even the flexible β model of Read & Steger (2017) break down for real galaxies undergoing hierarchical assembly (Cunningham et al. 2019). If we wish to understand the connection of galaxy assembly history to the orbital structure of galaxies, then we need to go beyond Jeans modeling to e.g., Schwarzschild orbit library methods (Romanowsky & Kochanek 2001; Zhu et al. 2018).

The Bayesian hierarchical modeling presented in this thesis requires a large number of repeated likelihood evaluations, which is much more demanding for orbit library methods. However, if we wish to understand how uncertainty in mass models propagates to our inferences of orbital anisotropy, we need a mechanism for doing Bayesian computation for models with over an order of magnitude more parameters (mostly taken up by the weights of orbits in the library).

One way forward would be to construct a partial likelihood where the mass model parameters are sampled via an MCMC algorithm and the orbit weights are determined through the usual optimization (e.g., quadratic programming) methods. The difficulty in this would be determining the proper degree of regularization for the orbit weight optimization to ensure that a small change in the proposed potential results in only a small change in the resulting anisotropy profiles. With such a computational method, we can apply many of the same techniques discussed in this work (e.g., multiple tracer population) to the questions about the detailed orbital anisotropy profiles of galaxies.

Bibliography

Aaronson, M. 1983, ApJL, 266, L11, doi: 10.1086/183969

Adams, J. J., Simon, J. D., Fabricius, M. H., et al. 2014, The Astrophysical Journal, 789, 63, doi: 10.1088/0004-637X/789/1/63

Agnello, A., Evans, N. W., Romanowsky, A. J., & Brodie, J. P. 2014, Monthly Notices of the Royal Astronomical Society, 442, 3299, doi: 10.1093/mnras/stu960

Akerib, D. S., Alsum, S., Araújo, H. M., et al. 2017, PhRvL, 118, 021303, doi: 10.1103/PhysRevLett.118.021303

Alabi, A. B., Forbes, D. A., Romanowsky, A. J., et al. 2017, Monthly Notices of the Royal Astronomical Society, 468, 3949, doi: 10.1093/mnras/stx678

Amorisco, N. C., Monachesi, A., Agnello, A., & White, S. D. M. 2018, MNRAS, 475, 4235, doi: 10.1093/mnras/sty116

Aprile, E., Aalbers, J., Agostini, F., et al. 2018, PhRvL, 121, 111302, doi: 10.1103/PhysRevLett.121.111302

Armengaud, E., Palanque-Delabrouille, N., Yèche, C., Marsh, D. J. E., & Baur, J. 2017, MNRAS, 471, 4606, doi: 10.1093/mnras/stx1870

Arnold, J. A., Romanowsky, A. J., Brodie, J. P., et al. 2014, The Astrophysical Journal, 791, 80, doi: 10.1088/0004-637X/791/2/80

Bar, N., Blas, D., Blum, K., & Sibiryakov, S. 2018, PhRvD, 98, 083027, doi: 10.1103/PhysRevD.98.083027

Bar, N., Blum, K., Eby, J., & Sato, R. 2019, PhRvD, 99, 103020, doi: 10.1103/PhysRevD.99.103020

Beasley, M. A., Baugh, C. M., Forbes, D. A., Sharples, R. M., & Frenk, C. S. 2002, Monthly Notices of the Royal Astronomical Society, 333, 383, doi: 10.1046/j.1365-8711.2002.05402.x

Beasley, M. A., Romanowsky, A. J., Pota, V., et al. 2016, ApJL, 819, L20, doi: 10.3847/2041-8205/819/2/L20

Bellstedt, S., Forbes, D. A., Foster, C., et al. 2017, MNRAS, 467, 4540, doi: 10.1093/mnras/stx418

Bernal, T., Fernández-Hernández, L. M., Matos, T., & Rodríguez-Meza, M. A. 2018, MNRAS, 475, 1447, doi: 10.1093/mnras/stx3208

Bertone, G., Hooper, D., & Silk, J. 2005, PhR, 405, 279, doi: 10.1016/j.physrep.2004.08.031

Bezanson, J., Edelman, A., Karpinski, S., & Shah, V. B. 2017, SIAM Review, 59, 65, doi: 10.1137/141000671

Binney, J., & Tremaine, S. 2008, Galactic Dynamics: Second Edition

Blumenthal, G. R., Faber, S. M., Flores, R., & Primack, J. R. 1986, ApJ, 301, 27, doi: 10.1086/163867

Boylan-Kolchin, M., Bullock, J. S., & Kaplinghat, M. 2011, MNRAS, 415, L40, doi: 10.

1111/j.1745-3933.2011.01074.x

Bozek, B., Marsh, D. J. E., Silk, J., & Wyse, R. F. G. 2015, MNRAS, 450, 209, doi: 10.1093/mnras/stv624

Bozek, B., Fitts, A., Boylan-Kolchin, M., et al. 2019, MNRAS, 483, 4086, doi: 10.1093/mnras/sty3300

Bringmann, T., & Hofmann, S. 2007, JCAP, 2007, 016, doi: 10.1088/1475-7516/2007/04/016

Brodie, J. P., & Strader, J. 2006, ARA&A, 44, 193, doi: 10.1146/annurev.astro.44.051905.092441

Brodie, J. P., Romanowsky, A. J., Strader, J., et al. 2014, The Astrophysical Journal, 796, 52, doi: 10.1088/0004-637X/796/1/52

Brough, S., Forbes, D. A., Kilborn, V. A., Couch, W., & Colless, M. 2006, Monthly Notices of the Royal Astronomical Society, 369, 1351, doi: 10.1111/j.1365-2966.2006.10387.x

Brown, W. R., Geller, M. J., Kenyon, S. J., & Kurtz, M. J. 2007, ApJ, 666, 231, doi: 10.1086/519547

Buck, T., Macciò, A. V., Dutton, A. A., Obreja, A., & Frings, J. 2019, MNRAS, 483, 1314, doi: 10.1093/mnras/sty2913

Buckley, M. R., & Peter, A. H. G. 2018, PhR, 761, 1, doi: 10.1016/j.physrep.2018.07.003

Buitrago, F., Trujillo, I., Curtis-Lake, E., et al. 2017, Monthly Notices of the Royal Astronomical Society, 466, 4888, doi: 10.1093/mnras/stw3382

Bullock, J. S., & Boylan-Kolchin, M. 2017, ARA&A, 55, 343, doi: 10.1146/annurev-astro-091916-055313

Calabrese, E., & Spergel, D. N. 2016, MNRAS, 460, 4397, doi: 10.1093/mnras/stw1256

Cantiello, M., Blakeslee, J. P., Raimondo, G., et al. 2005, ApJ, 634, 239, doi: 10.1086/491694

Cappellari, M., & Emsellem, E. 2004, PASP, 116, 138, doi: 10.1086/381875

Carleton, T., Errani, R., Cooper, M., et al. 2019, MNRAS, 485, 382, doi: 10.1093/mnras/stz383

Carlson, E. D., Machacek, M. E., & Hall, L. J. 1992, ApJ, 398, 43, doi: 10.1086/171833

Chabrier, G. 2003, ApJL, 586, L133, doi: 10.1086/374879

Chan, T. K., Kereš, D., Oñorbe, J., et al. 2015, MNRAS, 454, 2981, doi: 10.1093/mnras/stv2165

Chan, T. K., Kereš, D., Wetzel, A., et al. 2018, Monthly Notices of the Royal Astronomical Society, 478, 906, doi: 10.1093/mnras/sty1153

Chapman, S. C., Ibata, R., Lewis, G. F., et al. 2005, ApJL, 632, L87, doi: 10.1086/497686

Chemin, L., de Blok, W. J. G., & Mamon, G. A. 2011, AJ, 142, 109, doi: 10.1088/0004-6256/142/4/109

Chen, S.-R., Schive, H.-Y., & Chiueh, T. 2017, MNRAS, 468, 1338, doi: 10.1093/mnras/stx449

Choi, J., Dotter, A., Conroy, C., et al. 2016, ApJ, 823, 102, doi: 10.3847/0004-637X/823/2/102

Churazov, E., Tremaine, S., Forman, W., et al. 2010, MNRAS, 404, 1165, doi: 10.1111/j.1365-2966.2010.16377.x

Ciotti, L., & Bertin, G. 1999, A&A, 352, 447

Cohen, Y., van Dokkum, P., Danieli, S., et al. 2018, ApJ, 868, 96, doi: 10.3847/1538-4357/aae7c8

Collaboration, A., Price-Whelan, A. M., Sipőcz, B. M., et al. 2018a, AJ, 156, 123, doi: 10.3847/1538-3881/aabc4f

Collaboration, P., Aghanim, N., Akrami, Y., et al. 2018b, arXiv e-prints, arXiv:1807.06209

Collins, M. L. M., Chapman, S. C., Rich, R. M., et al. 2013, ApJ, 768, 172, doi: 10.1088/0004-637X/768/2/172

Colpi, M., Shapiro, S. L., & Wasserman, I. 1986, PhRvL, 57, 2485, doi: 10.1103/PhysRevLett.57.2485

Conroy, C., & van Dokkum, P. G. 2012, ApJ, 760, 71, doi: 10.1088/0004-637X/760/1/71

Conroy, C., Villaume, A., van Dokkum, P. G., & Lind, K. 2018, ApJ, 854, 139, doi: 10.3847/1538-4357/aaab49

Cooper, M. C., Newman, J. A., Davis, M., Finkbeiner, D. P., & Gerke, B. F. 2012, ascl, ascl:1203.003

Cunningham, E. C., Deason, A. J., Sanderson, R. E., et al. 2019, The Astrophysical Journal, 879, 120, doi: 10.3847/1538-4357/ab24cd

Das, P., Gerhard, O., Churazov, E., & Zhuravleva, I. 2010, MNRAS, 409, 1362, doi: 10.

1111/j.1365-2966.2010.17417.x

Davis, M., Lecar, M., Pryor, C., & Witten, E. 1981, ApJ, 250, 423, doi: 10.1086/159390

de Swart, J., Bertone, G., & van Dongen, J. 2017, Nature Astronomy, 1, 0059, doi: 10.1038/s41550-017-0059

de Vaucouleurs, G., de Vaucouleurs, A., Corwin, H. G., et al. 1991, Third Reference Catalogue of Bright Galaxies

Deason, A. J., Belokurov, V., Evans, N. W., & McCarthy, I. G. 2012, ApJ, 748, 2, doi: 10.1088/0004-637X/748/1/2

Dekel, A., Devor, J., & Hetzroni, G. 2003, MNRAS, 341, 326, doi: 10.1046/j.1365-8711.2003.06432.x

Dekel, A., Stoehr, F., Mamon, G. A., et al. 2005, Natur, 437, 707, doi: 10.1038/nature03970

Desjacques, V., Kehagias, A., & Riotto, A. 2018, PhRvD, 97, 023529, doi: 10.1103/PhysRevD.97.023529

Despali, G., Sparre, M., Vegetti, S., et al. 2019, MNRAS, 484, 4563, doi: 10.1093/mnras/stz273

Di Cintio, A., Brook, C. B., Dutton, A. A., et al. 2017a, MNRAS, 466, L1, doi: 10.1093/mnrasl/slw210

—. 2014, MNRAS, 441, 2986, doi: 10.1093/mnras/stu729

Di Cintio, A., Tremmel, M., Governato, F., et al. 2017b, MNRAS, 469, 2845, doi: 10.1093/mnras/stx1043

Diemer, B. 2018, ApJS, 239, 35, doi: 10.3847/1538-4365/aaee8c

Diemer, B., & Kravtsov, A. V. 2015, ApJ, 799, 108, doi: 10.1088/0004-637X/799/1/108

Dine, M., Fischler, W., & Srednicki, M. 1981, PhLB, 104, 199, doi: 10.1016/0370-2693(81)90590-6

Dutton, A. A., & Macciò, A. V. 2014, MNRAS, 441, 3359, doi: 10.1093/mnras/stu742

Dutton, A. A., Macciò, A. V., Stinson, G. S., et al. 2015, MNRAS, 453, 2447, doi: 10.1093/mnras/stv1755

Einasto, J. 1965, Trudy Astrofizicheskogo Instituta Alma-Ata, 5, 87

El-Zant, A. A., Freundlich, J., & Combes, F. 2016, Monthly Notices of the Royal Astronomical Society, 461, 1745, doi: 10.1093/mnras/stw1398

El-Zant, A. A., Hoffman, Y., Primack, J., Combes, F., & Shlosman, I. 2004, ApJL, 607, L75, doi: 10.1086/421938

Faber, S. M., & Gallagher, J. S. 1979, Annual Review of Astronomy and Astrophysics, 17, 135, doi: 10.1146/annurev.aa.17.090179.001031

Faber, S. M., Phillips, A. C., Kibrick, R. I., et al. 2003, SPIE, 4841, 1657, doi: 10.1117/12.460346

Fattahi, A., Navarro, J. F., Frenk, C. S., et al. 2018, MNRAS, 476, 3816, doi: 10.1093/mnras/sty408

Fitts, A., Boylan-Kolchin, M., Bozek, B., et al. 2019, Monthly Notices of the Royal Astronomical Society, 490, 962, doi: 10.1093/mnras/stz2613

Flores, R. A., & Primack, J. R. 1994, The Astrophysical Journal, 427, L1, doi: 10.1086/187350

Forbes, D. A. 2017, MNRAS, 472, L104, doi: 10.1093/mnrasl/slx148

Forbes, D. A., Ponman, T., & O'Sullivan, E. 2012, MNRAS, 425, 66, doi: 10.1111/j.1365-2966.2012.21368.x

Forbes, D. A., Sánchez-Blázquez, P., Phan, A. T. T., et al. 2006, MNRAS, 366, 1230, doi: 10.1111/j.1365-2966.2006.09763.x

Forbes, D. A., Sinpetru, L., Savorgnan, G., et al. 2017, MNRAS, 464, 4611, doi: 10.1093/mnras/stw2604

Foreman-Mackey, D., Hogg, D. W., Lang, D., & Goodman, J. 2013, PASP, 125, 306, doi: 10.1086/670067

Fosbury, R. a. E., Mebold, U., Goss, W. M., & Dopita, M. A. 1978, MNRAS, 183, 549, doi: 10.1093/mnras/183.4.549

Foster, C., Pastorello, N., Roediger, J., et al. 2016, MNRAS, 457, 147, doi: 10.1093/mnras/stv2947

Galassi, M., Theiler, J., Gough, B., et al. 2009, GNU Scientific Library Reference Manual, 3rd edn. (Network Theory Limited)

Garrison-Kimmel, S., Bullock, J. S., Boylan-Kolchin, M., & Bardwell, E. 2017, MNRAS, 464, 3108, doi: 10.1093/mnras/stw2564

Garzilli, A., Boyarsky, A., & Ruchayskiy, O. 2017, Physics Letters B, 773, 258, doi: 10.1016/j.physletb.2017.08.022

Gelman, A. 2006, Technometrics, 48, 432, doi: 10.1198/004017005000000661

Gelman, A., Hwang, J., & Vehtari, A. 2013, arXiv:1307.5928 [stat]. https://arxiv.org/abs/1307.5928

Gelman, A., & Rubin, D. B. 1992, Statistical Science, 7, 457, doi: 10.1214/ss/

1177011136

Genina, A., Benítez-Llambay, A., Frenk, C. S., et al. 2018, MNRAS, 474, 1398, doi: 10.1093/mnras/stx2855

Gnedin, O. Y., Kravtsov, A. V., Klypin, A. A., & Nagai, D. 2004, ApJ, 616, 16, doi: 10.1086/424914

González-Morales, A. X., Marsh, D. J. E., Peñarrubia, J., & Ureña-López, L. A. 2017, MNRAS, 472, 1346, doi: 10.1093/mnras/stx1941

Goodman, J., & Binney, J. 1984, MNRAS, 207, 511, doi: 10.1093/mnras/207.3.511

Goodman, J., & Weare, J. 2010, CAMCS, 5, 65, doi: 10.2140/camcos.2010.5.65

Graham, A. W., & Driver, S. P. 2005, Publications of the Astronomical Society of Australia, 22, 118, doi: 10.1071/AS05001

Greco, J. P., Greene, J. E., Price-Whelan, A. M., et al. 2018, PASJ, 70, S19, doi: 10.1093/pasj/psx051

Harris, W. E., Ciccone, S. M., Eadie, G. M., et al. 2017, ApJ, 835, 101, doi: 10.3847/1538-4357/835/1/101

Hastings, W. K. 1970, Biometrika, 57, 97, doi: 10.1093/biomet/57.1.97

Hayashi, K., & Obata, I. 2019, Monthly Notices of the Royal Astronomical Society, 2554, doi: 10.1093/mnras/stz2950

Hernquist, L. 1990, ApJ, 356, 359, doi: 10.1086/168845

Hlozek, R., Grin, D., Marsh, D. J. E., & Ferreira, P. G. 2015, PhRvD, 91, 103512, doi: 10.1103/PhysRevD.91.103512

Hobson, M. P., Bridle, S. L., & Lahav, O. 2002, MNRAS, 335, 377, doi: 10.1046/j.

1365-8711.2002.05614.x

Hu, W., Barkana, R., & Gruzinov, A. 2000, PhRvL, 85, 1158, doi: 10.1103/PhysRevLett.85.1158

Hui, L., Ostriker, J. P., Tremaine, S., & Witten, E. 2017, PhRvD, 95, 043541, doi: 10.1103/PhysRevD.95.043541

Humphrey, P. J., Buote, D. A., Gastaldello, F., et al. 2006, ApJ, 646, 899, doi: 10.1086/505019

Hunter, J. D. 2007, CSE, 9, 90, doi: 10.1109/MCSE.2007.55

Iršič, V., Viel, M., Haehnelt, M. G., Bolton, J. S., & Becker, G. D. 2017, Physical Review Letters, 119, 031302, doi: 10.1103/PhysRevLett.119.031302

Jarrett, T. H., Chester, T., Cutri, R., et al. 2000, AJ, 119, 2498, doi: 10.1086/301330

Jeffreys, H. 1945, Proceedings of the Royal Society A, 186, 9

Jiang, F., Dekel, A., Freundlich, J., et al. 2019, Monthly Notices of the Royal Astronomical Society, 487, 5272, doi: 10.1093/mnras/stz1499

Kafle, P. R., Sharma, S., Lewis, G. F., & Bland-Hawthorn, J. 2012, ApJ, 761, 98, doi: 10.1088/0004-637X/761/2/98

Kafle, P. R., Sharma, S., Robotham, A. S. G., Elahi, P. J., & Driver, S. P. 2018, MNRAS, 475, 4434, doi: 10.1093/mnras/sty118

Karachentsev, I. D., Karachentseva, V. E., Suchkov, A. A., & Grebel, E. K. 2000, A&AS, 145, 415, doi: 10.1051/aas:2000249

Kleyna, J. T., Wilkinson, M. I., Evans, N. W., & Gilmore, G. 2005, ApJL, 630, L141, doi: 10.1086/491654

Klypin, A., Kravtsov, A. V., Valenzuela, O., & Prada, F. 1999, ApJ, 522, 82, doi: 10.1086/307643

Kobayashi, T., Murgia, R., De Simone, A., Iršič, V., & Viel, M. 2017, Physical Review D, 96, 123514, doi: 10.1103/PhysRevD.96.123514

Koda, J., Yagi, M., Yamanoi, H., & Komiyama, Y. 2015, The Astrophysical Journal, 807, L2, doi: 10.1088/2041-8205/807/1/L2

Koposov, S. E., Casey, A. R., Belokurov, V., et al. 2015, ApJ, 811, 62, doi: 10.1088/0004-637X/811/1/62

Laporte, C. F. P., Agnello, A., & Navarro, J. F. 2019, MNRAS, 484, 245, doi: 10.1093/mnras/sty2891

Laporte, C. F. P., & White, S. D. M. 2015, MNRAS, 451, 1177, doi: 10.1093/mnras/stv112

Lee, J.-W., & Koh, I.-G. 1996, Physical Review D, 53, 2236, doi: 10.1103/PhysRevD.53.2236

Leong, K.-H., Schive, H.-Y., Zhang, U.-H., & Chiueh, T. 2019, Monthly Notices of the Royal Astronomical Society, 484, 4273, doi: 10.1093/mnras/stz271

Li, H., Ge, J., Mao, S., et al. 2017, ApJ, 838, 77, doi: 10.3847/1538-4357/aa662a

Lim, S., Peng, E. W., Côté, P., et al. 2018, ApJ, 862, 82, doi: 10.3847/1538-4357/aacb81

Lima Neto, G. B., Gerbal, D., & Márquez, I. 1999, MNRAS, 309, 481, doi: 10.1046/j.1365-8711.1999.02849.x

Łokas, E. L. 2002, Monthly Notices of the Royal Astronomical Society, 333, 697, doi: 10.

1046/j.1365-8711.2002.05457.x

Lora, V., & Magaña, J. 2014, Journal of Cosmology and Astroparticle Physics, 2014, 011, doi: 10.1088/1475-7516/2014/09/011

Lovell, M. R., Gonzalez-Perez, V., Bose, S., et al. 2017, Monthly Notices of the Royal Astronomical Society, 468, 2836, doi: 10.1093/mnras/stx621

Ma, Y.-Z., & Berndsen, A. 2014, A&C, 5, 45, doi: 10.1016/j.ascom.2014.04.005

Mamon, G. A., & Łokas, E. L. 2005, MNRAS, 363, 705, doi: 10.1111/j.1365-2966.2005.09400.x

Marrodán Undagoitia, T., & Rauch, L. 2016, JPhG, 43, 013001, doi: 10.1088/0954-3899/43/1/013001

Marsh, D. J. E. 2016, PhR, 643, 1, doi: 10.1016/j.physrep.2016.06.005

Marsh, D. J. E., & Niemeyer, J. C. 2019, Physical Review Letters, 123, 051103, doi: 10.1103/PhysRevLett.123.051103

Marsh, D. J. E., & Pop, A.-R. 2015, Monthly Notices of the Royal Astronomical Society, 451, 2479, doi: 10.1093/mnras/stv1050

Martin, N. F., Collins, M. L. M., Longeard, N., & Tollerud, E. 2018, ApJL, 859, L5, doi: 10.3847/2041-8213/aac216

Martin, N. F., Ibata, R. A., Lewis, G. F., et al. 2016, ApJ, 833, 167, doi: 10.3847/1538-4357/833/2/167

Martín-Navarro, I., La Barbera, F., Vazdekis, A., Falcón-Barroso, J., & Ferreras, I. 2015, MNRAS, 447, 1033, doi: 10.1093/mnras/stu2480

Martín-Navarro, I., Romanowsky, A. J., Brodie, J. P., et al. 2019, Monthly Notices of the Royal Astronomical Society, 484, 3425, doi: 10.1093/mnras/stz252

Martínez-Delgado, D., Läsker, R., Sharina, M., et al. 2016, AJ, 151, 96, doi: 10.3847/0004-6256/151/4/96

Martizzi, D., Teyssier, R., & Moore, B. 2013, MNRAS, 432, 1947, doi: 10.1093/mnras/stt297

Mashchenko, S., Wadsley, J., & Couchman, H. M. P. 2008, Sci, 319, 174, doi: 10.1126/science.1148666

Matos, T., Vázquez-González, A., & Magaña, J. 2009, Monthly Notices of the Royal Astronomical Society, 393, 1359, doi: 10.1111/j.1365-2966.2008.13957.x

McConnell, N. J., Chen, S.-F. S., Ma, C.-P., et al. 2013, ApJL, 768, L21, doi: 10.1088/2041-8205/768/1/L21

McConnell, N. J., Lu, J. R., & Mann, A. W. 2016, ApJ, 821, 39, doi: 10.3847/0004-637X/821/1/39

McKinney, W. 2010, in Proceedings of the 9th Python in Science Conference, 51–56

Merritt, A., van Dokkum, P., Danieli, S., et al. 2016, ApJ, 833, 168, doi: 10.3847/1538-4357/833/2/168

Merritt, D. 1985, MNRAS, 214, 25P, doi: 10.1093/mnras/214.1.25P

Metropolis, N., & Ulam, S. 1949, Journal of the American Statistical Association, 44, 335, doi: 10.1080/01621459.1949.10483310

Mihos, J. C., Durrell, P. R., Ferrarese, L., et al. 2015, The Astrophysical Journal, 809, L21, doi: 10.1088/2041-8205/809/2/L21

Mitzkus, M., Cappellari, M., & Walcher, C. J. 2017, MNRAS, 464, 4789, doi: 10.1093/

mnras/stw2677

Mocz, P., Vogelsberger, M., Robles, V. H., et al. 2017, Monthly Notices of the Royal Astronomical Society, 471, 4559, doi: 10.1093/mnras/stx1887

Moore, B., Ghigna, S., Governato, F., et al. 1999, ApJL, 524, L19, doi: 10.1086/312287

Moster, B. P., Naab, T., & White, S. D. M. 2013, MNRAS, 428, 3121, doi: 10.1093/mnras/sts261

Mowla, L., van Dokkum, P., Merritt, A., et al. 2017, ApJ, 851, 27, doi: 10.3847/1538-4357/aa961b

Munshi, F., Brooks, A. M., Applebaum, E., et al. 2017, arXiv, arXiv:1705.06286

Nadler, E. O., Gluscevic, V., Boddy, K. K., & Wechsler, R. H. 2019, ApJL, 878, L32, doi: 10.3847/2041-8213/ab1eb2

Napolitano, N. R., Pota, V., Romanowsky, A. J., et al. 2014, MNRAS, 439, 659, doi: 10.1093/mnras/stt2484

Napolitano, N. R., Romanowsky, A. J., & Tortora, C. 2010, MNRAS, 405, 2351, doi: 10.1111/j.1365-2966.2010.16710.x

Napolitano, N. R., Romanowsky, A. J., Coccato, L., et al. 2009, MNRAS, 393, 329, doi: 10.1111/j.1365-2966.2008.14053.x

Navarro, J. F., Eke, V. R., & Frenk, C. S. 1996, Monthly Notices of the Royal Astronomical Society, 283, L72, doi: 10.1093/mnras/283.3.L72

Navarro, J. F., Frenk, C. S., & White, S. D. M. 1997, ApJ, 490, 493, doi: 10.1086/304888

Newman, A. B., Treu, T., Ellis, R. S., & Sand, D. J. 2013a, ApJ, 765, 25, doi: 10.1088/0004-637X/765/1/25

Newman, A. B., Treu, T., Ellis, R. S., et al. 2013b, ApJ, 765, 24, doi: 10.1088/0004-637X/765/1/24

Newman, J. A., Cooper, M. C., Davis, M., et al. 2013c, ApJS, 208, 5, doi: 10.1088/0067-0049/208/1/5

Nori, M., Murgia, R., Iršič, V., Baldi, M., & Viel, M. 2019, MNRAS, 482, 3227, doi: 10.1093/mnras/sty2888

Novak, G. S., Cox, T. J., Primack, J. R., Jonsson, P., & Dekel, A. 2006, ApJL, 646, L9, doi: 10.1086/506605

Ogiya, G. 2018, MNRAS, 480, L106, doi: 10.1093/mnrasl/sly138

Oh, S.-H., de Blok, W. J. G., Brinks, E., Walter, F., & Kennicutt, R. C. 2011, AJ, 141, 193, doi: 10.1088/0004-6256/141/6/193

Oldham, L., & Auger, M. 2018a, MNRAS, 474, 4169, doi: 10.1093/mnras/stx2969

Oldham, L. J., & Auger, M. W. 2016, MNRAS, 457, 421, doi: 10.1093/mnras/stv2982

—. 2018b, MNRAS, 476, 133, doi: 10.1093/mnras/sty065

Oñorbe, J., Boylan-Kolchin, M., Bullock, J. S., et al. 2015, MNRAS, 454, 2092, doi: 10.1093/mnras/stv2072

Oñorbe, J., Domínguez-Tenreiro, R., Sáiz, A., & Serna, A. 2007, MNRAS, 376, 39, doi: 10.1111/j.1365-2966.2006.11411.x

Oort, J. H. 1932, Bulletin of the Astronomical Institutes of the Netherlands, 6, 249

Oser, L., Ostriker, J. P., Naab, T., Johansson, P. H., & Burkert, A. 2010, ApJ, 725, 2312, doi: 10.1088/0004-637X/725/2/2312

Osipkov, L. P. 1979, Pisma v Astronomicheskii Zhurnal, 5, 77

Ostrov, P., Geisler, D., & Forte, J. C. 1993, The Astronomical Journal, 105, 1762, doi: 10.1086/116553

Paggi, A., Kim, D.-W., Anderson, C., et al. 2017, ApJ, 844, 5, doi: 10.3847/1538-4357/aa7897

Pandya, V., Romanowsky, A. J., Laine, S., et al. 2018, ApJ, 858, 29, doi: 10.3847/1538-4357/aab498

Pastorello, N., Forbes, D. A., Foster, C., et al. 2014, MNRAS, 442, 1003, doi: 10.1093/mnras/stu937

Peccei, R. D., & Quinn, H. R. 1977, PhRvL, 38, 1440, doi: 10.1103/PhysRevLett.38.1440

Pedregosa, F., Varoquaux, G., Gramfort, A., et al. 2011, Journal of Machine Learning Research, 12, 2825

Peirani, S., Dubois, Y., Volonteri, M., et al. 2017, MNRAS, 472, 2153, doi: 10.1093/mnras/stx2099

Peng, E. W., & Lim, S. 2016, ApJL, 822, L31, doi: 10.3847/2041-8205/822/2/L31

Peng, E. W., Jordán, A., Côté, P., et al. 2006, ApJ, 639, 95, doi: 10.1086/498210

Perez, F., & Granger, B. E. 2007, CSE, 9, 21, doi: 10.1109/MCSE.2007.53

Piironen, J., & Vehtari, A. 2017, Statistics and Computing, 27, 711, doi: 10.1007/s11222-016-9649-y

Pineda, J. C. B., Hayward, C. C., Springel, V., & Mendes de Oliveira, C. 2017, MNRAS, 466, 63, doi: 10.1093/mnras/stw3004

Planck Collaboration, P., Ade, P. a. R., Aghanim, N., et al. 2016, A&A, 594, A13, doi: 10.1051/0004-6361/201525830

Poci, A., Cappellari, M., & McDermid, R. M. 2017, MNRAS, 467, 1397, doi: 10.1093/mnras/stx101

Pontzen, A., & Governato, F. 2012, MNRAS, 421, 3464, doi: 10.1111/j.1365-2966.2012.20571.x

Pota, V., Forbes, D. A., Romanowsky, A. J., et al. 2013, MNRAS, 428, 389, doi: 10.1093/mnras/sts029

Pota, V., Brodie, J. P., Bridges, T., et al. 2015, MNRAS, 450, 1962, doi: 10.1093/mnras/stv677

Prieto, J. L., & Gnedin, O. Y. 2008, ApJ, 689, 919, doi: 10.1086/591777

Proctor, R. N., Forbes, D. A., Romanowsky, A. J., et al. 2009, MNRAS, 398, 91, doi: 10.1111/j.1365-2966.2009.15137.x

Profumo, S. 2017, An Introduction to Particle Dark Matter, doi: 10.1142/Q0001

Quintana, H., Fouque, P., & Way, M. J. 1994, A&A, 283, 722

Rackauckas, C., & Nie, Q. 2017, Journal of Open Research Software, 5, 15, doi: 10.5334/jors.151

Read, J. I., Iorio, G., Agertz, O., & Fraternali, F. 2016, MNRAS, 462, 3628, doi: 10.1093/mnras/stw1876

Read, J. I., & Steger, P. 2017, MNRAS, 471, 4541, doi: 10.1093/mnras/stx1798

Read, J. I., Wilkinson, M. I., Evans, N. W., Gilmore, G., & Kleyna, J. T. 2006, MNRAS, 366, 429, doi: 10.1111/j.1365-2966.2005.09861.x

Retana-Montenegro, E., van Hese, E., Gentile, G., Baes, M., & Frutos-Alfaro, F. 2012, Astronomy and Astrophysics, 540, A70, doi: 10.1051/0004-6361/201118543

Robles, V. H., Bullock, J. S., & Boylan-Kolchin, M. 2019, MNRAS, 483, 289, doi: 10.1093/mnras/sty3190

Robles, V. H., Lora, V., Matos, T., & Sánchez-Salcedo, F. J. 2015, ApJ, 810, 99, doi: 10.1088/0004-637X/810/2/99

Rocha, M., Peter, A. H. G., Bullock, J. S., et al. 2013, MNRAS, 430, 81, doi: 10.1093/mnras/sts514

Rodriguez-Gomez, V., Pillepich, A., Sales, L. V., et al. 2016, MNRAS, 458, 2371, doi: 10.1093/mnras/stw456

Rodríguez-Puebla, A., Primack, J. R., Avila-Reese, V., & Faber, S. M. 2017, MNRAS, 470, 651, doi: 10.1093/mnras/stx1172

Romanowsky, A. J., & Kochanek, C. S. 2001, ApJ, 553, 722, doi: 10.1086/320947

Romanowsky, A. J., Strader, J., Spitler, L. R., et al. 2009, AJ, 137, 4956, doi: 10.1088/0004-6256/137/6/4956

Röttgers, B., Naab, T., & Oser, L. 2014, MNRAS, 445, 1065, doi: 10.1093/mnras/stu1762

Rubin, V. C., Ford, Jr., W. K., & Thonnard, N. 1978, The Astrophysical Journal Letters, 225, L107, doi: 10.1086/182804

Rusli, S. P., Thomas, J., Saglia, R. P., et al. 2013, AJ, 146, 45, doi: 10.1088/0004-6256/146/3/45

Salpeter, E. E. 1955, ApJ, 121, 161, doi: 10.1086/145971

Schaller, M., Frenk, C. S., Bower, R. G., et al. 2015a, MNRAS, 452, 343, doi: 10.1093/

mnras/stv1341

—. 2015b, MNRAS, 451, 1247, doi: 10.1093/mnras/stv1067

Schive, H.-Y., Chiueh, T., & Broadhurst, T. 2014a, NatPh, 10, 496, doi: 10.1038/nphys2996

Schive, H.-Y., Chiueh, T., Broadhurst, T., & Huang, K.-W. 2016, ApJ, 818, 89, doi: 10.3847/0004-637X/818/1/89

Schive, H.-Y., Liao, M.-H., Woo, T.-P., et al. 2014b, PhRvL, 113, 261302, doi: 10.1103/PhysRevLett.113.261302

Schuberth, Y., Richtler, T., Hilker, M., et al. 2010, A&A, 513, A52, doi: 10.1051/0004-6361/200912482

Shen, J., & Gebhardt, K. 2010, ApJ, 711, 484, doi: 10.1088/0004-637X/711/1/484

Simon, J. D., Bolatto, A. D., Leroy, A., & Blitz, L. 2003, ApJ, 596, 957, doi: 10.1086/378200

Smercina, A., Bell, E. F., Price, P. A., et al. 2018, ApJ, 863, 152, doi: 10.3847/1538-4357/aad2d6

Sokal, A. 1997, in Functional Integration, ed. C. DeWitt-Morette, P. Cartier, & A. Folacci, Vol. 361 (Boston, MA: Springer US), 131–192, doi: 10.1007/978-1-4899-0319-8_6

Sonnenfeld, A., Treu, T., Marshall, P. J., et al. 2015, ApJ, 800, 94, doi: 10.1088/0004-637X/800/2/94

Spekkens, K., Giovanelli, R., & Haynes, M. P. 2005, AJ, 129, 2119, doi: 10.1086/429592

Spolaor, M., Forbes, D. A., Hau, G. K. T., Proctor, R. N., & Brough, S. 2008, MNRAS, 385, 667, doi: 10.1111/j.1365-2966.2008.12891.x

Straton, J. C. 2002, Results in Mathematics, 41, 394, doi: 10.1007/BF03322781

Su, Y., Gu, L., White, R. E., & Irwin, J. 2014, ApJ, 786, 152, doi: 10.1088/0004-637X/786/2/152

Su, Y., & Irwin, J. A. 2013, ApJ, 766, 61, doi: 10.1088/0004-637X/766/1/61

Taylor, E. N., Hopkins, A. M., Baldry, I. K., et al. 2011, MNRAS, 418, 1587, doi: 10.1111/j.1365-2966.2011.19536.x

Tegmark, M., Eisenstein, D. J., Strauss, M. A., et al. 2006, PhRvD, 74, 123507, doi: 10.1103/PhysRevD.74.123507

Thomas, J., Saglia, R. P., Bender, R., et al. 2007, MNRAS, 382, 657, doi: 10.1111/j.1365-2966.2007.12434.x

Tollet, E., Macciò, A. V., Dutton, A. A., et al. 2016, MNRAS, 456, 3542, doi: 10.1093/mnras/stv2856

Toloba, E., Lim, S., Peng, E., et al. 2018, ApJL, 856, L31, doi: 10.3847/2041-8213/aab603

Trimble, V. 1987, Annual Review of Astronomy and Astrophysics, 25, 425, doi: 10.1146/annurev.aa.25.090187.002233

Trujillo, I., Beasley, M. A., Borlaff, A., et al. 2019, MNRAS, 486, 1192, doi: 10.1093/mnras/stz771

Tully, R. B., Courtois, H. M., Dolphin, A. E., et al. 2013, AJ, 146, 86, doi: 10.1088/0004-6256/146/4/86

van den Bosch, F. C., Ogiya, G., Hahn, O., & Burkert, A. 2018, MNRAS, 474, 3043, doi: 10.1093/mnras/stx2956 van der Burg, R. F. J., Hoekstra, H., Muzzin, A., et al. 2017, A&A, 607, A79, doi: 10.1051/0004-6361/201731335

van der Walt, S., Colbert, S. C., & Varoquaux, G. 2011, CSE, 13, 22, doi: 10.1109/MCSE.2011.37

van der Wel, A., Franx, M., van Dokkum, P. G., et al. 2014, ApJ, 788, 28, doi: 10.1088/0004-637X/788/1/28

van Dokkum, P., Conroy, C., Villaume, A., Brodie, J., & Romanowsky, A. J. 2017a, ApJ, 841, 68, doi: 10.3847/1538-4357/aa7135

van Dokkum, P., Danieli, S., Cohen, Y., Romanowsky, A. J., & Conroy, C. 2018a, ApJL, 864, L18, doi: 10.3847/2041-8213/aada4d

van Dokkum, P., Abraham, R., Brodie, J., et al. 2016, ApJL, 828, L6, doi: 10.3847/2041-8205/828/1/L6

van Dokkum, P., Abraham, R., Romanowsky, A. J., et al. 2017b, ApJL, 844, L11, doi: 10.3847/2041-8213/aa7ca2

van Dokkum, P., Danieli, S., Cohen, Y., et al. 2018b, Natur, 555, 629, doi: 10.1038/nature25767

van Dokkum, P., Cohen, Y., Danieli, S., et al. 2018c, RNAAS, 2, 54, doi: 10.3847/2515-5172/aacc6f

—. 2018d, ApJL, 856, L30, doi: 10.3847/2041-8213/aab60b

van Dokkum, P., Wasserman, A., Danieli, S., et al. 2019, The Astrophysical Journal, 880, 91, doi: 10.3847/1538-4357/ab2914

van Dokkum, P. G., Abraham, R., Merritt, A., et al. 2015, ApJL, 798, L45, doi: 10.

1088/2041-8205/798/2/L45

Vehtari, A., Gelman, A., & Gabry, J. 2015, arXiv, arXiv:1507.04544

Viel, M., Lesgourgues, J., Haehnelt, M. G., Matarrese, S., & Riotto, A. 2005, PhRvD, 71, 063534, doi: 10.1103/PhysRevD.71.063534

Villaume, A., Conroy, C., Johnson, B., et al. 2017, ApJS, 230, 23, doi: 10.3847/1538-4365/aa72ed

Virtanen, P., Gommers, R., Oliphant, T. E., et al. 2019, arXiv:1907.10121 [physics]. https://arxiv.org/abs/1907.10121

Walker, M. G., & Peñarrubia, J. 2011, ApJ, 742, 20, doi: 10.1088/0004-637X/742/1/20

Wang, W., Han, J., Cole, S., et al. 2018, MNRAS, 476, 5669, doi: 10.1093/mnras/sty706

Wasserman, A., Romanowsky, A. J., Brodie, J., et al. 2018a, The Astrophysical Journal, 863, L15, doi: 10.3847/2041-8213/aad779

—. 2018b, The Astrophysical Journal, 863, 130, doi: 10.3847/1538-4357/aad236

Wasserman, A., van Dokkum, P., Romanowsky, A. J., et al. 2019, The Astrophysical Journal, 885, 155, doi: 10.3847/1538-4357/ab3eb9

Watkins, L. L., Evans, N. W., & An, J. H. 2010, MNRAS, 406, 264, doi: 10.1111/j.1365-2966.2010.16708.x

Weinberg, D. H., Bullock, J. S., Governato, F., Kuzio de Naray, R., & Peter, A. H. G. 2015, PNAS, 112, 12249, doi: 10.1073/pnas.1308716112

Wittman, D., Golovich, N., & Dawson, W. A. 2018, ApJ, 869, 104, doi: 10.3847/1538-4357/aaee77

Xu, D., Springel, V., Sluse, D., et al. 2017, MNRAS, 469, 1824, doi: 10.1093/mnras/

stx899

Yagi, M., Koda, J., Komiyama, Y., & Yamanoi, H. 2016, ApJS, 225, 11, doi: 10.3847/0067-0049/225/1/11

Zepf, S. E., & Ashman, K. M. 1993, Monthly Notices of the Royal Astronomical Society, 264, 611, doi: 10.1093/mnras/264.3.611

Zhang, H.-X., Peng, E. W., Côté, P., et al. 2015, ApJ, 802, 30, doi: 10.1088/0004-637X/802/1/30

Zhang, Z., Xu, H., Wang, Y., et al. 2007, ApJ, 656, 805, doi: 10.1086/510281

Zhu, L., Long, R. J., Mao, S., et al. 2014, ApJ, 792, 59, doi: 10.1088/0004-637X/792/1/59

Zhu, L., Romanowsky, A. J., van de Ven, G., et al. 2016, MNRAS, 462, 4001, doi: 10.1093/mnras/stw1931

Zhu, L., van den Bosch, R., van de Ven, G., et al. 2018, Monthly Notices of the Royal Astronomical Society, 473, 3000, doi: 10.1093/mnras/stx2409

Zinn, R. 1985, The Astrophysical Journal, 293, 424, doi: 10.1086/163249

Zwicky, F. 1937, The Astrophysical Journal, 86, 217, doi: 10.1086/143864